# Applications for Transition Metal Chemistry in Contrast Enhanced Magnetic Resonance Imaging

**Abhishek Gupta**[1,2], **Peter Caravan**[3,4], **William S. Price**[1,2], **Carlos Platas-Iglesias**[5], **Eric M. Gale**[3]

[1]Nanoscale Organisation and Dynamics Group, School of Science and Health, Western Sydney University, Penrith, NSW 2751, Australia

[2]Ingham Institute of Applied Medical Research, Liverpool, NSW 2170, Australia

[3]Athinoula A. Martinos Center for Biomedical Imaging, Department of Radiology, Massachusetts General Hospital/Harvard Medical School, Massachusetts 02129, United States

[4]Institute for Innovation in Imaging, Department of Radiology, Massachusetts General Hospital/ Harvard Medical School, Massachusetts 02129, United States

[5]Universidade da Coruña, Centro de Investigacións Científicas Avanzadas (CICA) and Departamento de Química, Facultade de Ciencias, 15071, A Coruña, Galicia, Spain.

## Abstract

Contrast enhanced magnetic resonance imaging (MRI) is an indispensable tool for diagnostic medicine. However, safety concerns related to gadolinium in commercial MRI contrast agents have emerged in recent years. For patients suffering from severe renal impairment, there is an important unmet medical need to perform contrast enhanced MRI without gadolinium. There are also concerns over the long-term effects of retained gadolinium within the general patient population. Demand for gadolinium-free MRI contrast agents is driving a new wave of inorganic chemistry innovation as researchers explore paramagnetic transition metal complexes as potential alternatives. Furthermore, advances in personalized care making use of molecular level information have motivated inorganic chemists to develop MRI contrast agents that can detect pathologic changes at the molecular level. Recent studies have highlighted how reaction-based modulation of transition metal paramagnetism offers a highly effective mechanism to achieve MRI contrast enhancement that is specific to biochemical processes. This Viewpoint article highlights how recent advances in transition metal chemistry are leading the way for a new generation of MRI contrast agents.

## Introduction.

Magnetic resonance imaging (MRI) plays a critical role in modern radiology, enabling high resolution visualization of soft tissue and vascular structures without exposing patients to ionizing radiation. Image contrast in MRI depends on the concentration and the relaxation times ($T_1$, $T_2$, $T_2^*$) of magnetically resonant protons, comprised predominantly of water and fat. Endogenous contrast is not always sufficient to visualize abnormalities but this can be overcome by administration of a paramagnetic MRI contrast agent, which shortens the relaxation times of nearby water protons and renders pathologic tissue highly conspicuous.[1] Contrast agents can add tremendous value to an MRI scan and are now heavily relied upon for detection of abnormalities in the brain and body,[2–3] diagnosis and staging of malignancies,[4–5] to inform therapeutic interventions,[6] and to monitor patient response to treatment.[7] Tens of millions of contrast enhanced MRI scans are performed each year worldwide.[1]

All products currently marketed for MRI contrast comprise aqueous parenteral formulations of low-molecular weight $Gd^{3+}$ chelates called gadolinium-based contrast agents (GBCAs).[8] Nine GBCAs are approved for use by the US Food and Drug Administration (FDA), and six GBCAs are authorized for marketing within the European Union, Figure 1.[9] The first GBCA received FDA approval for the detection of blood-brain barrier (BBB) disruptions in 1988, and with the exception of a few agents developed for liver imaging and angiography, the majority of the contrast agents introduced since then were designed as essentially interchangeable products.

$Gd^{3+}$ and $Eu^{2+}$ are the most potent ions for generating $T_1$-relaxation (positive MRI contrast), but it is challenging to stabilize $Eu^{2+}$ outside of a rigorously anaerobic environment.[10–11] $Gd^{3+}$ chelates were a logical first choice for clinical MRI contrast agents. It is possible to develop potent relaxation agents using other metal ions,[12] but substantially less research and development has been dedicated to contrast agents not containing Gd. GBCAs have a very low incidence of adverse drug reactions[8] and there was little motivation for chemists to develop alternatives to GBCAs. However, various concerns related to Gd retention and late toxicity have emerged over the last 14 years prompting regulatory actions and concerns amongst physicians and patients.[13–16] These safety concerns, which are described in more depth below, have stimulated new research into Gd-free contrast agents.

There is also a growing interest in developing MRI contrast agents for molecular imaging to detect and quantify metabolic or biochemical changes associated with disease. Molecular imaging can aid in early detection,[17–18] differential diagnosis,[18–20] therapeutic planning,[21] and monitoring of treatment response[22] based on non-invasively obtained biochemical information. Clinical molecular imaging is performed with nuclear medicine modalities like single photon emission computed tomography (SPECT) and positron emission tomography (PET), which require infrastructure to synthesize and purify compounds containing short lived isotopes, expose patients to ionizing radiation, and offer poor spatial resolution for disease mapping compared to MRI.[1, 23–24] No MRI contrasts agents are available for clinical molecular imaging but recent works have demonstrated the tremendous power of transition

metal redox and spin crossover as mechanisms for biochemically responsive MR signal modulation.

Here we review some exciting developments in transition metal-based MRI contrast agents in the separate contexts of gadolinium-free MRI and molecular MR imaging. We will provide background on the motivations to pursue this research, outline design criteria for an effective GBCA replacement or biochemically responsive agent, and highlight innovative inorganic chemistry related to these efforts. The scope of this article is limited to low-molecular weight transition metal complexes that generate MRI contrast via $T_1$-relaxation, magnetic saturation transfer, or chemical shift. The theory underlying MRI contrast mechanisms is discussed only insofar as required to contextualize the inorganic chemistry discussed in this article. Readers are referred to excellent existing review articles for information regarding clinical MRI,[25] in depth discussions of theory related to MR contrast mechanisms,[1, 26–28] lanthanide-based contrast agents,[29–30] or macromolecular and nanoparticle-based contrast agents.[31–33]

### Transition metal complexes as alternatives to GBCAs.

**Background.—**In 2006, GBCA exposure was directly linked to a devasting fibrosing condition termed nephrogenic systemic fibrosis (NSF) that can occur in patients suffering renal impairment.[14, 34] In 2007, the US Food and Drug Administration (FDA) responded by applying a boxed warning to all GBCAs and assigning a contraindication for the use of three GBCAs (Gd-DTPA, Gd-DTPA-BMA, and Gd-DTPA-BMEA, see Fig 1) for use in patients suffering from severe renal insufficiency or acute kidney injury.[35] The mechanistic link between Gd and NSF remains unknown and underexplored, but a 2009 FDA data-mining analysis indicated that the frequency of NSF incidence associated with different GBCAs is correlated inversely to the kinetic inertness of the chelate.[35] The vast majority of NSF cases are associated with acyclic GBCAs derived from a diethylenetriamine backbone, Fig 1A. Few unconfounded NSF cases have been documented for macrocyclic GBCAs derived from a cyclen backbone, which are substantially more inert to Gd dechelation, Fig 1C, although the majority of MRI exams to that point in time were performed with acyclic GBCAs.[36]

New cases of NSF are now extremely rare due to updated physician guidelines and careful screening of patients with impaired renal function. However, it is important to note that there are currently no clinically available alternatives to GBCAs. Iodinated X-ray contrast agents for computed tomography are the most similar available contrast media, but these agents are associated with nephrotoxicity in patients suffering renal insufficiency.[37–38] An estimated 16% of US adults suffer from moderate to advanced chronic kidney disease,[39–40] and this patient population is disproportionately afflicted by comorbidities like cancer and peripheral artery disease that are often diagnosed and managed with the aid of medical imaging.

Concerns over GBCA safety were reignited in 2013 following a report that identified endogenously hyperintense signal in the dentate nucleus and globus pallidus of patients receiving prior contrast enhanced scans.[41] Elemental analysis of neurologic tissue collected upon autopsy of patients receiving GBCAs confirmed that Gd retention was indeed the cause of the signal hyperintensity.[15] Gd accumulation in brain tissue is long-term and cumulative with repeat dosing.[42] Gd brain deposition has been observed following exposure to both

acyclic and macrocyclic GBCAs, but the acyclic agents are associated with a higher degree of Gd retention.[43] As a result of these findings, the European Medicines Agency (EMA) recommended suspending the marketing authorization of three GBCAs in 2017 and restricted the use of two others for liver imaging only, Figs 1A–B.[9] Other regulatory bodies such as FDA, Pharmaceuticals and Medical Devices Agency (PMDA, Japan) and Therapeutic Goods Administration (TGA, Australia) did not restrict any GBCAs, but issued revised precautions and warnings.[44–46] Recently, two acyclic GBCAs were voluntarily withdrawn from the US market by their manufacturers. It is important to note that there is no confirmed toxicity associated with Gd retention in neurologic tissues.

Recent reports of NSF-like symptoms and clouded mentation arising after GBCA exposure in patients with normal renal function have been broadly characterized as gadolinium deposition disease (GDD).[47–48] GDD is controversial and not widely accepted in the medical community. Symptoms are typically self-reported by patients.[48] However, NSF-like symptoms are clinically documented and it has been observed that Gd can be found in the urine of these patients long after their last scan. Moreover the Gd urine content can be increased when these patients are provoked with DTPA, including patients who had received the more inert macrocyclic GBCAs.[49]

**Requirements for an effective GBCA alternative.—**GBCAs are highly versatile and add tremendous diagnostic value to an MRI scan. Upon intravenous injection, GBCAs rapidly distribute through the blood pool and extracellular spaces, and are then rapidly eliminated by renal filtration. Angiographic images to diagnose vascular abnormalities can be acquired in the seconds after injection when the GBCA makes its first pass through the arteries.[50] Dynamic phase images acquired during the arterial and venous phases can also be useful for characterizing tumor vasculature.[51] Hyperpermeable lesions remain conspicuously hyperintense in the minutes after injection, after blood pool enhancement has diminished substantially. Dynamic imaging of GBCA uptake and washout from hyperpermeable lesions can be useful for assessing risk for malignancy in diseases like breast cancer.[52]

A GBCA alternative must provide comparable or improved diagnostic efficacy at a safe dose. A number of considerations must be taken into account when designing a GBCA alternative. Detection sensitivity should be optimized to afford the highest possible contrast enhancement at the lowest possible dose. Pharmacokinetics must also be considered. Current contrast enhanced MRI imaging protocols and workflows are designed for contrast agents that distribute rapidly through the blood pool and extracellular spaces and rapidly washout out from blood and normal tissue. A hyperpermeable lesion is detected minutes after GBCA injection, but may require hours or even longer for detection with a macromolecule or nanoparticle-based agent. In this regard, low-molecular weight, hydrophilic chelates represent the most obvious choice for GBCA alternatives. Metal ion related toxicity is a major safety concern for metal-based contrast agents. Different metal ions are tolerated up to different thresholds, exhibit varying degrees of bioavailability, and different modes of toxicity. There are unfortunately no defined criteria for thermodynamic stability or kinetic inertness that equate to safety. As a rule of thumb, new metal-ion based contrast agents should be designed to be as thermodynamically stable and kinetically inert as reasonably possible. The intact complex itself must also be non-toxic. The contrast agent should be

highly soluble in water. GBCAs are formulated at 0.5M or greater, and typically administered intravenously to adult patients at volumes of 10 – 20 mL. New contrast agents need not necessarily be formulated or dosed identically, but the agent should be soluble enough that a diagnostically effective dose can be administered at a reasonable volume. Solutions of the contrast agent must not be too viscous to facilitate intravenous administration.

### Transition metal complexes as $T_1$-relaxation agents.

**$T_1$-relaxation mechanism.**—The signal-generating efficacy of a $T_1$-relaxation agents is measured by relaxivity ($r_1$), Eq 1,

$$r_1 = \frac{\frac{1}{T_1} - \frac{1}{T_{1,dia}}}{[M]} = r_1^{IS} + r_1^{SS} + r_1^{OS} \qquad \text{Eq 1.}$$

which describes the paramagnetically induced $T_1$ shortening normalized to the concentration of the contrast agent. A contrast agent interacts with water in few different ways and each interaction contributes to $r_1$. Overall $r_1$ receives contributions from water molecules directly coordinated to the paramagnetic metal, if present, ($r_1^{IS}$, $IS$ = inner sphere), from second sphere water molecules that associate with the metal complex via hydrogen bonding interactions ($r_1^{SS}$), as well as from outer sphere water molecules that diffuse in and out of proximity with the metal complex ($r_1^{OS}$). For GBCAs, $r_1$ receives roughly equal contributions from $r_1^{IS}$ and $r_1^{OS}$,[53] contributions from $r_1^{SS}$ are typically small but can be increased substantially by the presence of negatively charged donor groups such as phosphonates or by introducing pendant anionic functional groups. [54–55] For a given metal ion, a chemist can rationally control $r_1^{IS}$ through fine tuning the chemical structure, whereas $r_1^{SS}$ and $r_1^{OS}$ are more challenging to control. The magnitude of $r_1^{IS}$ depends on the number ($q$), relaxation time ($T_{1m}$) and mean residency time ($\tau_m$) of water molecules bound to the metal ion, Eq 2, Fig 2.

$$r_1^{IS} = \frac{\frac{q}{[H_2O]}}{T_{1m} + \tau_m} \qquad \text{Eq 2.}$$

Accurate determination of $q$ and $\tau_m$ are important to characterizing and devising strategies to optimize new $T_1$-relaxation agents. Solutions spectroscopic techniques to determine $q$ are well established for Gd complexes, but are comparatively underdeveloped for paramagnetic transition metal complexes. Once $q$ is known $\tau_m$ can be ready determined by measuring the temperature dependence of paramagnetically induced $T_2$ relaxation of bulk water $^{17}O$ and fitting the data with the Swift-Connick equations describing two-site exchange.[56] Two experimental methods have been recently proposed to determine $q$ for $Mn^{2+}$ complexes. One study demonstrated how the temperature dependence of the $Mn^{2+}$ induced line-broadening of the bulk water $^{17}O$ NMR resonance encodes for $q$.[57] It was shown that at the temperature position where line-broadening is greatest, $q$ is directly proportional to the full-width at half-max (FWHM). In another study, a semi-empirical expression to estimate $q$ from $r_1$ recorded

at Larmor frequency 1 MHz was proposed after careful analysis of previously reported nuclear magnetic relaxometric dispersion (NMRD) data of 49 $Mn^{2+}$ complexes.[58]

At magnetic field strengths 0.2T (~10 MHz), which are typical for the vast majority clinical and pre-clinical MRI applications, $T_{1m}$ is governed by a dipolar mechanism which is described by the general Solomon-Bloembergen-Morgan (SBM) Theory, Eq 3

$$\frac{1}{T_{1m}} = \frac{2}{15}\left(\frac{\mu_0}{4\pi}\right)^2 \frac{\gamma_H^2 g_e^2 \mu_B^2 S(S+1)}{r_{MH}^6}\left[\frac{3\tau_C}{1+\omega_H^2\tau_C^2}\right] \qquad \text{Eq. 3}$$

where $\gamma_H$ and $\omega_H$ are the proton gyromagnetic ratio and Larmor frequency, $g_e$ is the Landé g-factor for a free electron, and $\mu_B$ is the Bohr Magneton. A chemist can optimize $T_{1m}$ by introducing a metal ion of difference spin quantum number ($S$), altering the distance between the paramagnetic ion and water $^1H$ ($r_{MH}$), or by altering the correlation time (time required for 1 radian rotation perpendicular to the applied field) for magnetic field fluctuations experienced by the water $^1Hs$ ($\tau_C$).

The parameter $\tau_C$ receives contributions from three dynamic processes, Eq 4,

$$\frac{1}{\tau_C} = \frac{1}{\tau_R} + \frac{1}{\tau_m} + \frac{1}{T_{1e}} \qquad \text{Eq. 4}$$

$\tau_m$, the rotational correlation time ($\tau_R$), and the longitudinal electron spin relation time ($T_{1e}$), which refers to the time constant for electronic spin states to return to their equilibrium populations after ligand field perturbations. $\tau_C$ is controlled by whichever dynamic process occurs on the fastest time scale. For low molecular weight metal complexes, $\tau_R$ occurs on the ps time scale. $\tau_m$ can range from ps to seconds, depending on the metal ion and ligand environment. $T_{1e}$ is on the ns time scale for systems with electronically isolated electronic ground states such as ions with S-state free ion ground term configurations like $Gd^{3+}$ or $Mn^{2+}$, or strongly Jahn-Teller distorted ions like in many $Cu^{2+}$ systems). For systems with excited state configurations that are easily accessed via spin-orbit coupling interactions, $T_{1e}$ occurs typically on the ps time scale. For most GBCAs and $Mn^{2+}$ complexes, $\tau_m$ and $T_{1e}$ occur on the ns time scale, so $\tau_C \cong \tau_R$.[59]

The $T_{1m}$ mechanism is most efficient when $1/\tau_C$ and $\omega_H$ are closely matched. At MRI Larmor frequencies ranging 20–80 MHz, $r_1$ of $Gd^{3+}$ and $Mn^{2+}$ complexes can be increased by incorporation into higher molecular weight, more slowly rotating structures, effectively slowing $\tau_C$ from the ps to ns regime. For example, $r_1$ of the albumin binding complex Mn-LCyPh$_2$ increases from 5.8 mM$^{-1}$s$^{-1}$ in water to 46 mM$^{-1}$s$^{-1}$ in 660 µM HSA solution at 0.47 T ($\nu_H$ = 20 MHz). At 1.4T ($\nu_H$ = 60 MHz), $r_1$ increases from 5.3 mM$^{-1}$s$^{-1}$ to 46 mM$^{-1}$s$^{-1}$. As the MRI Larmor frequency increases beyond 80 MHz, the $r_1$ of macromolecule associated $Gd^{3+}$ or $Mn^{2+}$ complexes drops precipitously. Note in Table 1 how the $r_1$ increase achieved by albumin binding of Mn-LCyPh$_2$ is substantially lower at $\nu_H$ 128 MHz than at $\nu_H$ 60 MHz. The combined influence of $\tau_R$ and $^1H$ Larmor frequency on $r_1^{IS}$ are depicted in Figure 3. Because the $S(S+1)/r_{MH}^6$ component of Equation 3 yields nearly identical values for $Mn^{2+}$ and $Gd^{3+}$, analogous results are obtained if the same simulation is applied

to a $Gd^{3+}$ complex There is evidence that $r_1$ for complexes of $Mn^{3+}$ and $Fe^{3+}$ can also be substantially increased by slowing $\tau_R$. $Mn^{3+}$ and $Fe^{3+}$ complexes are expected to exhibit shorter $T_{1e}$ values than complexes of $Gd^{3+}$ and $Mn^{2+}$, and as a result the influence of changing $\tau_R$ may exhibit a different field dependency. To date, the mechanisms underpinning $r_1$ for $Mn^{3+}$ and $Fe^{3+}$ complexes have been less extensively studied.

For low molecular weight $Gd^{3+}$ or $Mn^{2+}$ systems where $\tau_R$ occurs on the ps time scale $r_1$ is relatively insensitive to changes in $\tau_m$ unless the complex exhibits rare behavior in which $\tau_m$ accelerates into the ps regime where it is fast enough to influence $\tau_C$ or slows to the μs regime where water exchange may be slow with respect to $T_{1m}$. For complexes where $\tau_R$ is rotationally optimized, $r_1$ can be very sensitive to $\tau_m$. Figures 4A and 4B depict the influence of $\tau_m$ on $r_1^{IS}$ at 0.47T, 1.5T, and 4.7T for a $Mn^{2+}$ complex where $\tau_R = 80$ ns and for one where $\tau_R$ has been slowed so that $1/\tau_R = \omega_H$. As in Figure 3, the simulations yield almost identical $r_1^{IS}$ values for complexes of $Gd^{3+}$. The precise $\tau_m$ required for to achieve the greatest $r_1$ will vary as a function of both $\tau_R$ and $^1H$ Larmor frequency, and the reader is referred to more in depth reviews on this topic.[60–61] The impact of changing $\tau_m$ for relaxation agents of other paramagnetic ions is less well studied.

Increasing $\tau_R$ can increase the $r_1$ of GBCAs, but on the other hand increasing $\tau_R$ through protein binding or incorporating the GBCA into a macromolecule can also alter pharmacokinetics of the contrast agent in ways that render the agent less useful in the context of clinical imaging protocols, as described above. Low-molecular weight chelates have been favored for clinical development, despite their lower $r_1$.

**Mn-based relaxation agents.**—High spin $Mn^{2+}$ complexes can behave as potent relaxation agents. Like $Gd^{3+}$, high-spin $Mn^{2+}$ has a symmetrically half-filled valence subshell and is capable of forming ternary complexes with poly/amino-carboxylate chelators and labile water co-ligand(s). There is a precedence for the use of $Mn^{2+}$ in contrast enhanced MRI in humans. The chelate Mn-DPDP has US FDA and EMA approvals for detection of liver tumors,[62] although it is no longer marketed. Mn-DPDP is a labile complex that dissociates $Mn^{2+}$ upon injection into the bloodstream, and the dissociated $Mn^{2+}$ transiently accumulates in hepatocytes enabling identification of liver metastases as hypointense abnormalities.[63–65] Free dissociated $Mn^{2+}$ enters cells via pathways of $Ca^{2+}$ flux, and thus exhibits a high degree of uptake by excitable cells like cardiomyocytes and insulin releasing pancreatic β cells.[66–67] A formulation comprised of free $Mn^{2+}$ and $Ca^{2+}$ gluconate was developed for cardiac imaging and was evaluated in a Phase II clinical trial (NCT00881075).[68] The free $Mn^{2+}$ transiently accumulates within viable cardiomyocytes via voltage-gated $Ca^{2+}$ channel uptake.[69–70] Free $Mn^{2+}$ antagonizes voltage-gated $Ca^{2+}$ uptake, but the toxicity is offset by co-administration of $Ca^{2+}$. The $Mn^{2+}$:$Ca^{2+}$ ratio is tuned so that $Mn^{2+}$ uptake is diagnostically useful but not cardio-depressive. A liposomal oral formulation containing $MnCl_2$ has an FDA approval for bowel imaging but is no longer marketed. An oral formulation of $MnCl_2$ with D-alanine and vitamin $D_3$ to stimulate enterohepatic circulation is currently being evaluated in Phase III trials for detection of focal lesions in liver tissue (NCT04119843). A formulation comprising paramagnetic Mn(II) containing monodisperse nanoparticles with average hydrodynamic radius 5–6 nm[71–72] is currently

being evaluated in a Phase I clinical trial to assess safety, tolerability, and pharmacokinetics in breast cancer patients (NCT04080024).

There is a proven diagnostically utility and track record of safe clinical use for Mn-based contrast agents. However, previously used $Mn^{2+}$-based agents cannot substitute for GBCAs, which are administered as bolus injections, confine to extracellular spaces, and are rapidly eliminated. A suitable Mn-based alternative should have pharmacokinetics that are analogous to GBCAs, be thermodynamically stable and kinetically inert enough to be administered as a bolus injection without inducing any cardiovascular toxicity, and have $r_1$ comparable to or higher than GBCAs.

A number of $Mn^{2+}$ chelates have been evaluated in the context of GBCA alternatives. A comprehensive review of this expanding body of work extends beyond the scope of this Viewpoint article, but notable examples are shown in Fig 5 and their $r_1$ values are compared in Table 2. Thermodynamic stability constants and $Mn^{2+}$ dissociation kinetics under different sets of reaction conditions compared in Tables 3 and 4.

$Mn^{2+}$ complexes with rapidly exchanging water co-ligand(s) can achieve $r_1$ comparable to GBCAs. The smaller $S$ relative to Gd is compensated for by the reduced $r_{MH}$ (estimated 2.8Å and 3.1Å for $Mn^{2+}$ and $Gd^{3+}$, respectively). Based on the $S(S+1)/r_{MH}^6$ component of Eq 3, $Mn^{2+}$ generates $r_1^{IS}$ as effectively as $Gd^{3+}$ for an equivalent $\tau_R$ value. When comparing $r_1$ of $Mn^{2+}$ and $Gd^{3+}$ complexes in Table 1, the values largely reflect differences in molecular weight. Note the comparable relaxivities of $Mn^{2+}$ and $Gd^{3+}$ chelates of similar molecular weight when recorded under identical conditions (Mn-PyC3A-3-OBn and Gd-DOTA, for example). Like $Gd^{3+}$, the $r_1$ of most $Mn^{2+}$ complexes can be increased by slowing $\tau_R$ and $Mn^{2+}$ agents capable of protein binding exhibit elevated $r_1$ in blood plasma. In this regard, a number of $Mn^{2+}$ complexes conjugated to albumin-targeting moieties have been synthesized as high-$r_1$ contrast agents. Examples of $Mn^{2+}$ complexes with exceptionally high affinity for HSA include Mn-EDTA-BOM$_2$, Mn-LCyPh2, Mn-C12OPAADA, Mn-DPAC12A, Mn-DPAC6PHA, and Mn-mX(DPAMA)2, Figure 5; $r_1$ values valued in Table 1.

We are unaware of any studies to aimed at improving $r_1$ through $\tau_m$ optimization, but recent work has demonstrated how $\tau_m$ can be controlled by systematic modifications to ligands that support high $r_1$ and kinetically inert $Mn^{2+}$ complexes. For example, water exchange at $Mn^{2+}$-NO2A-type complexes like $Mn^{2+}$-MeNO2A and $Mn^{2+}$-MeBzNO2A (Figure 5) occurs by an associative mechanism and the process is slowed by modifications that introduce bulky substituents that hinder access of water molecules approaching the $Mn^{2+}$ water binding site.[73] The effect is illustrated by comparing the $\tau_m$ for $Mn^{2+}$-MeNO2A (1.6 ns at 25 °C) and $Mn^{2+}$-MeBzNO2A (38 ns at 25 °C). Water exchange of 7-coordinate ternary complexes comprising acyclic EDTA-like ligands is believed to occur by a dissociative mechanism which can be slowed by increasing ligand rigidity, which raises the activation energy required to achieve the 6-coordinate water dissociated transition state. For example, $\tau_m$ for $Mn^{2+}$-EDTA and $Mn^{2+}$-CyDTA are 2.4 ns and 7.1 ns, respectively.[74–75]

$Mn^{2+}$ complexes with a vacant coordination site for water co-ligand binding are inherently less thermodynamically stable than GBCAs. The reduced stability of $Mn^{2+}$ complexes is partially a function of the reduced charge-to-radius ratio compared to $Gd^{3+}$. Additionally, the smaller size of the $Mn^{2+}$ ion requires penta- or hexadentate ligands to accommodate $q=1$, whereas $q=1$ $Gd^{3+}$ can be accommodated by octadentate ligands. It is our view that the lower thermodynamic stability of $Mn^{2+}$ complexes does not mean the complexes are "insufficiently stable." Several q=1 $Mn^{2+}$ complexes have conditional pH 7.4 stability constants (log $K_{cond\ pH\ 7.4}$) greater than 10, i.e. a dissociation constant, $K_d < 10$ pM.

Of more serious concern is the perceived kinetic lability of $Mn^{2+}$ chelates compared to GBCAs. Even for thermodynamically stable complexes, substantial exposure to dissociated metal ions can occur if the complex is kinetically labile with respect to metal ion dissociation. However, recent work has shown that using rigid acyclic or macrocyclic ligands, it is indeed possible to develop high-relaxivity $Mn^{2+}$ complexes that appear to be comparably or more inert than some GBCAs based on functional assays of kinetic inertness. [76–79] Comparison of Mn and Gd dissociation rates under four different sets of reaction conditions (Dissociation Challenges 1–4) are listed in Table 4. For example, the q=1 chelate $Mn^{2+}$-PyC3A is comparably inert to Gd-DTPA under assay conditions used to compare dissociation kinetics of GBCAs (Dissociation Challenge 1). [80–81] Under these conditions, 2.5 mM contrast agent is incubated with 2.5 mM $Zn^{2+}$ in 50 mM pH 7.0 phosphate buffer at 37 °C, and kinetic inertness is compared by measuring the time required to achieve 20% release of the paramagnetic ion ($t_{20\%}$). In a side-by-side comparison, 1.8 h and 2.8 min were required for 20% dissociation of Mn-PyC3A and Gd-DTPA, respectively. [79] Under conditions of Dissociation Challenge 2 (1 mM contrast agent, 25 mM $Zn^{2+}$, pH 6.0 MES buffer), Mn-PyC3A was found to be 20-fold more inert than Gd-DTPA. The complex Mn-PC2A-EA, which appears to be the most kinetically inert $Mn^{2+}$ complex of q > 0 reported to date, [78] appears to be over one and two orders of magnitude more inert than Gd-DTPA when evaluated according to Dissociation Challenge 3 ([contrast agent] = $[Zn^{2+}]$ or $[Cu^{2+}]$ = 0.01 mM, pH 7.4) and Dissociation Challenge 4 ([contrast agent] = $[Zn^{2+}]$ or $[Cu^{2+}]$ = 1.0 mM, pH 7.4), respectively, which estimate the rates of trans-chelation in the presence of $Cu^{2+}$ or $Zn^{2+}$ based on quantitative thermodynamic and rate law data.

Side by side comparisons of $Mn^{2+}$ and $Gd^{3+}$ dissociation kinetics highlight the inertness of the Mn complexes, but the relative rates of Mn vs. Gd dissociation are not consistent across all reaction conditions. Different complexes may undergo dissociation via different reactions mechanisms. For many of the $Mn^{2+}$ complexes listed in Table 4, dissociation in the presence of competing metal ions like $Cu^{2+}$ and $Zn^{2+}$ is rate limited by spontaneous dissociation of the mono-protonated $Mn^{2+}$ complex, exhibiting effectively zero-order kinetics with respect to concentration of the challenging metal ion. For example, the rates of $Mn^{2+}$ dissociation from Mn-CyDTA, Mn-12-PyN4A, Mn-15-PyN5, Mn-PC2A and Mn-DO2A derivatives are either unaffected or modestly inhibited by increasing challenging ion concentration. [78, 82–84] On the other hand, dissociation of Gd-DTPA exhibits a first order dependence on challenger metal ion concentration. [85] Side by side comparisons of Mn-CyDTA vs. Gd-DTPA kinetic inertness under Dissociation Challenges 3 and 4 exemplifies the challenge in comparing kinetic inertness of complexes that dissociate by different reaction mechanisms. Mn-CyDTA appears to be over an order of magnitude less inert than Gd-DTPA under Dissociation

Challenge 3 but is estimated to be almost four-fold *more* inert under Dissociation Challenge 4, where the concentrations of the contrast agent and challenger metal ion are each elevated by 100-fold. Although GBCA inertness seems to correlate with Gd retention, it is unclear whether there is any in vitro assay to accurately predict the degree to which $Mn^{2+}$ is dissociated or retained in vivo. It is our view that thermodynamic stability and kinetic inertness should be prioritized when developing complexes of $Mn^{2+}$ or other metal ions as GBCA alternatives. However, given the paucity of in vivo data related to metal ion retention from Gd-free contrast agents, researchers should also be aware that in vitro assays for stability and inertness may not necessarily predict metal exposure in vivo. As more $Mn^{2+}$ complexes are evaluated as MRI contrast agents, functional assays capable of predicting kinetic inertness in vivo may emerge.

The complex $Mn^{2+}$-PyC3A was rationally designed as a GBCA alternative.[79] The PyC3A chelate imparts high thermodynamic stability and kinetic inertness, as described above, while simultaneously leaving a vacant coordination site for a rapidly exchanging water co-ligand.[79] The $r_1$ of Mn-PyC3A, Gd-DTPA, and Gd-DOTA in human blood plasma are 3.5, 4.1, and 3.6 $mM^{-1}s^{-1}$, respectively at 1.5T and 37 °C.[86–87] The blood clearance pharmacokinetics of Mn-PyC3A were quantified in a baboon model and shown to be analogous to Gd-DTPA.[88] Like Gd-DTPA, the hydrophilic character and anionic overall charge limit distribution to the extracellular spaces. Although hydrophilic overall, the hydrophobic *trans*-1,2-diaminocyclohexyl backbone and pyridyl segments of the chelate impart a degree of amphiphilicity (octanol:water partition coefficient,[79, 89] logP = 0.595) which is believed to promote partial hepatobiliary excretion. Partial hepatobiliary clearance has been demonstrated in mouse and baboon imaging studies.[79, 88] Quantification of fractional excretion in rats demonstrated roughly 85% renal and 15% hepatobiliary elimination of Mn-PyC3A.[89]

The comparable $r_1$ values and pharmacokinetics of Mn-PyC3A to GBCAs result in comparable MRI contrast enhancement in vivo. Mn-PyC3A demonstrated angiographic contrast that was not significantly different from an equal dose of Gd-DTPA in a baboon model.[88] Mn-PyC3A was also demonstrated to be highly effective for tumor visualization. Figure 6 shows a side by side comparison of axial $T_1$-weighted images of an orthotopic mouse model of breast cancer acquired prior to and 3 min after injection of 0.1 mmol/kg Gd-DOTA and 0.1 mmol/kg Mn-PyC3A. The tumor is located in the upper left thoracic mammary pad and denoted by the yellow arrow. Prior to contrast injection, the tumor is isointense relative to adjacent muscle tissue but is rendered similarly hyperintense after injection of either agent. Quantitation of post-injection – pre-injection tumor vs. muscle contrast-to-noise ratios demonstrated no significant difference using the Gd and Mn agents.[89]

The in vivo stability of Mn-PyC3A was demonstrated by tandem HPLC-ICP-MS analysis of blood plasma and urine collected from baboons following Mn-PyC3A injection. The chromatography traces provide sensitive detection of Mn-containing species and revealed little evidence of metabolism or Mn de-chelation.[88]

A side by side comparison of whole body Mn vs. Gd elimination in rats receiving equal doses of 2.0 mmol/kg Mn-PyC3A or Gd-DOTA demonstrated that significantly lower quantities of Mn than Gd were retained in the rats 1 day and 7 days after injection.[89] By 7 days, Mn levels were either significantly lower or not significantly different than Gd levels in each of the 20 tissues analyzed during the study. Tables 3 and 4 show that Gd-DOTA is orders of magnitude more stable than Mn-PyC3A, and is extremely kinetically inert compared to $Mn^{2+}$ chelates, but the in vivo biodistribution data highlights how $Mn^{2+}$ and $Gd^{3+}$ are processed by distinctly different biochemistry and underscores how in vitro assays of stability and inertness are inadequate measures of long term metal exposure.

Mn-based alternatives to liver specific GBCAs have also been explored. Mn-EDTA functionalized with lipophilic ethoxybenzyl (Mn-EOB-DTPA) and benzothiazole aniline moieties (Mn-BTA-EDTA) have been reported, and it was demonstrated that a 0.05 mmol/kg dose of either agent provided delayed phase liver enhancement that improves visualization of liver tumors in mice.[90–91] The transient liver uptake of Mn-PyC3A has also been capitalized on for liver specific imaging.[89] A more amphiphilic derivative of Mn-PyC3A-3-OBn (logP = 1.15) was recently reported for liver specific imaging and provides substantially greater liver-to-tumor CNR than Mn-PyC3A.[86]

$Mn^{3+}$ porphyrins have also been considered as GBCA alternatives, Figure 7, Table 2. The $r_1$ of $Mn^{3+}$-porphyrins are substantially larger than GBCAs and has been described as 'anomalously' high.[92] Magnetic relaxation in the presence of $Mn^{3+}$ is underexplored compared to $Gd^{3+}$ and $Mn^{2+}$, but the unexpectedly high relaxivity has been attributed in part to the presence of two rapidly exchanging water co-ligands, close $r_{MH}$ interations, and longer than expected $T_{1e}$ considering the asymmetrically occupied $d^4$ ground state electronic configuration. The long $T_{1e}$ has been attributed to a large Jahn-Teller distortion, resulting in a large energy separation and reduced admixture between the vacant $x^2$-$y^2$ orbitals and four half-filled $d$-orbitals, effectively minimizing spin-orbit coupling interactions. It has also been proposed that interactions between water-$^1H$ and electron spin exceed what is predicted by the $1/r_{MH}^6$ approximation due to an anisotropic electronic wavefunction that is elongated along the $d_z^2$ orbital axis pointing at the water co-ligands.[92]

Preliminary in vivo evaluation of $Mn^{3+}$ porphyrins as MRI contrast agents has yielded promising results. Strong tumor enhancement was achieved between 2 and 4 hours following a 0.09 mmol/kg dose of Mn-TPPS$_4$ in murine xenograft models of human carcinoma, lymphoma, and fibrosarcoma.[93] In another study, Mn-TPPS$_4$ provided strong contrast enhancement of human breast cancer and colorectal xenografts in mice.[94] Mn-TPPS$_4$, Mn-TPPS$_3$, Mn-*cis*-TPPS $_2$, and Mn-*trans*-TPPS $_2$ were all shown to be effective contrast agents for visualizing tumors in an orthotopic mouse model of breast cancer.[95] Mn-TPPS$_4$ and Mn-mesoporphoryin provide delayed liver enhancement than has used for detection of liver metastases in rats.[96–97] The anionic chelate Mn-TCP and neutral dimeric chelate Mn-P2 have been evaluated evaluated as GBCA alternatives[98–101] Dynamic MRI measurements demonstrated that Mn-TCP has comparable pharmacokinetics, and biodistribution to Gd-DTPA and provided stronger tumor enhancement that Gd-DTPA in a rat xenograft model of breast cancer.[100–101] Mn-P2 provided prolonged blood pool enhancement that could be potentially useful for MR angiography applications.[99]

The thermodynamic stability and kinetic inertness of $Mn^{3+}$-porphyrins are underexplored. The increased charge-to-radius ratio compared with $Mn^{2+}$ and ligand field stabilization energy associated with the $d^4$ configuration suggest that $Mn^{3+}$-porphyrins should be thermodynamically stable. However, the thermodynamic stability of $Mn^{3+}$ chelates is difficult to assess, as the free $Mn^{3+}$ ion rapidly disproportionates to $Mn^{4+}$ and $Mn^{2+}$, rendering pH-potentiometric titration experiments challenging. We are unaware of any reported experiments to interrogate the kinetic inertness of $Mn^{3+}$ porphyrins. One study demonstrated that incubation of 0.5 mg/mL Mn-TPPS$_4$ in blood plasma at 37 °C did not result in detectable amounts of free TPPS$_4$ ligand over 9 days.[102] Given the high relaxivity and in vivo imaging efficacy of $Mn^{3+}$-porphyrin complexes, studies to further evaluate the in vivo efficacy and safety are certainly merited.

$Mn^{3+}$ complexes of 1,2-phenylenediamine bisamide ligands shown in Fig 7 have also been synthesized as MRI contrast agents. Studies with these complexes have focused on molecular imaging applications,[103–104] but this class of compounds could also be considered for evaluation as GBCA alternatives.

**Fe-based relaxation agents.—**High-spin S=5/2 complexes of $Fe^{3+}$ represent another potential alternative to GBCAs. Endogenous levels of Fe are high, ranging 3–4 g total Fe in human adults, with highly regulated systems for transport and storage.[105] Nonetheless, free $Fe^{3+}$ exhibits acute toxicity at high doses and $Fe^{3+}$ solubility is exceedingly low at neutral pH. In this regard, high-relaxivity $Fe^{3+}$ complexes are subject to the same thermodynamic stability and kinetic inertness considerations as complexes of other metal ions.

The $r_1$ values for $Fe^{3+}$ chelates that have been evaluated as MRI contrast agents are tabulated in Table 2. Magnetic relaxation in the presence of $Fe^{3+}$ has not been explored as thoroughly as for $Mn^{2+}$ and $Gd^{3+}$ but nuclear magnetic relaxation dispersion (NMRD) measurements performed on Fe-EDTA and relaxometric evaluation of free vs. protein bound $Fe^{3+}$-EHPG indicate that $r_1$ is controlled predominantly by $\tau_R$.[106–107] $Fe^{3+}$ is a stronger Lewis acid compared to $Gd^{3+}$ or $Mn^{2+}$ and care must be taken to ensure that water co-ligand pKa is high enough to avoid formation of Fe-hydroxide or Fe-oxo ligands, which may substantially reduce inner sphere contributions to $r_1$. The water co-ligand p$K_a$ values of four structurally related acyclic chelates are compared in Table 5, and demonstrate how for $Fe^{3+}$ complexes the water co-ligand pKa is strongly influenced by changes ligand environment.[108–110] For example, swapping the *trans*-1,2-cyclohexylene backbone of Fe-CyDTA for a 1,2-phenylene backbone (Fe-PhDTA) can alter the acidity of the water co-ligand by >5 pKa units. Care must be also taken to ensure stabilization of high-spin $Fe^{3+}$, as the increased charge-to-radius ratio results in chelates with greater crystal field splitting energy compared to corresponding $Mn^{2+}$ chelates. For example, the TACN-derived ligands L1-L4, Fig 8, support complexes of high-spin $Fe^{3+}$, but swapping the 2-hydroybenzyl or acetate pendant donor arms for more strong field 2-methylimidazole (Fe-Tim) or 1-methyl-2-methylimidazole (Fe-Mim) donors results in complexes of low-spin $Fe^{3+}$.[111–112]

Because $Fe^{3+}$ has a substantially larger charge-to-radius ratio than $Mn^{2+}$ or $Gd^{3+}$, $Fe^{3+}$ tends to form complexes which are more thermodynamically stable.[113] For example, the log $K_{ML}$ values of the $Fe^{3+}$, $Mn^{2+}$ and $Gd^{3+}$ complexes of DTPA are 28.0, 14.1 and 22.5, respectively.

[114–115] The kinetic inertness of $Fe^{3+}$ contrast agents are largely underexplored compared to $Mn^{2+}$ and $Gd^{3+}$ contrast agents. There is also paucity of data pertaining to in vivo Fe retention following $Fe^{3+}$ contrast agent injection, although one study demonstrated 95% recovery of $^{54}Fe$ labelled $Fe^{3+}$-CyDTA in urine 1h after injection of a 0.1 mmol/kg dose in mice.[113] There is no excretory path for de-chelated iron and this data suggests that $Fe^{3+}$-CDTA is rapidly eliminated in vivo without undergoing substantial Fe dechelation.

In vivo imaging studies support $Fe^{3+}$ chelates as potentially suitable GBCA alternatives. $Fe^{3+}$-EHPG was shown to be an effective hepatobiliary agent and it was reported that doses as high as 2.0 mmol/kg administered to rats were well tolerated without observation of any safety signals.[116] Comparison of 0.2 mmol/kg dose of Fe-CyDTA to a 0.1 mmol/kg dose of Gd-DTPA demonstrated comparable tumor vs. adjacent muscle CNR in a murine xenograft model of human breast cancer.[117] A 0.05 mmol/kg dose of Fe-L1 showed strong enhancement of the blood pool and kidneys that rapidly diminished in the minutes following injection, consistent with rapid elimination via renal filtration, as well as liver enhancement that persisted for out to 4 hours post-injection but returned to near baseline levels within 24h, consistent with hepatocellular uptake.[111]

### Transition metal complexes as paraCEST agents.

Another way to generate MRI contrast is via the chemical exchange saturation transfer (CEST) mechanism. CEST contrast is achieved though radiofrequency saturation of protons capable of exchange with bulk water, resulting in MR signal loss, Figure 9.[118–120] Labile protons for CEST imaging are typically provided by functional groups such as amines, amides, alcohols, or phenols, and can be from endogenous sources like amino acids or exogenously added contrast agents. When the CEST agent is a metal complex, labile protons can be provided via exchangeable water co-ligand(s).[121] The magnitude of the CEST effect is most commonly characterized as Magnetization Transfer asymmetry (MTR$_{assym}$), eq. 7

$$MTR_{assym} = \frac{SI(-\Delta\omega) - SI(+\Delta\omega)}{SI_O} \qquad \text{Eq. 7}$$

where $SI(-\omega)$ and $SI(+\omega)$ are the water $^1H$ signal intensities acquired with RF saturation applied on resonance with the exchangable proton pool and at the off-resonance frequency symmetric with respect to the water signal, $SI_0$ is water $^1H$ signal intensity with no RF saturation applied.[119]

The CEST effect exhibits dependencies on the magnitude of chemical shift between the $^1H$ of water and the proton exchanging functional group ($\omega$), the corresponding rate of prototropic exchange ($k_{ex}$), and radiofrequency power used to achieve magnetic saturation ($B_1$) of the labile protons bound to the CEST agent. Each of these parameters can be expressed in Hz. In order for CEST to be achieved, $k_{ex}$ must not exceed $\omega$, CEST criterion 1. Within this limit the CEST effect increases with $k_{ex}$, provided $B_1 << \omega$ so as to avoid blunting the CEST effect by direct RF saturation of bulk water protons, CEST criterion 2. Increasing $k_{ex}$ results in exchange broadening of the bound proton resonance and requires greater $B_1$ to achieve full magnetic saturation which can result in a violation of CEST criterion 2 and can increases the specific absorption rate (SAR) of RF radiation, resulting in

tissue heating. Thus, a careful balance between $\Delta\omega$, $k_{ex}$, and $B_1$ must be struck when optimizing CEST contrast agents.[121]

CEST criterion 1: $k_{ex} \leq \Delta\omega$

CEST criterion 2: $B_1 << \Delta\omega$

Under conditions where CEST criteria 1 and 2 are met, CEST contrast agent efficacy is governed by equation 8,

$$\frac{SI(\Delta\omega)}{SI_O} = \frac{1}{1 + \frac{[mM]q^H}{[H_2O]}(k_{ex})(T_{1a})}$$

Eq. 8

where $q^H$ is the number of exchangeable protons bound to the contrast agent, $\tau_m^{\ H}$ is the mean residency time of the exchangeable proton, and $T_{1a}$ refers to the $T_1$ of water.

There have been studies which suggest that CEST agents could be used in place of GBCAs. The iodinated X-ray contrast agents iopamidol, iohexol, and iodixanol, Fig 10a, each contain multiple labile OH groups and have been used to visualize tumors and quantify perfusion in an orthotopic mouse model of breast cancer via CEST contrast enhancement.[122–123]

However, there are also substantial drawbacks to using CEST agents when compared to GBCAs. CEST agents are detected with substantially lower sensitivity than relaxation agents. In the murine breast cancer imaging experiment discussed in the above paragraph, tumor contrast enhancement observed following 10 mmol/kg (7.8 to 16 g contrast agent per kg animal, depending on the X-ray agent used) iodinated contrast agent (reported as percentage saturation transfer) was nearly an order of magnitude lower than that observed after injection of 0.1 mmol/kg Gd-HPDO3A (percentage signal enhancement). Essentially, the CEST agent was detected with 1000-fold lower sensitivity.[122] Another drawback is that the CEST effect is also very sensitive to the magnetic field inhomogeneities that are present when scanning live subjects. Moreover, the CEST effect in vivo is superimposed on a very broad CEST-like effect called magnetization transfer.[124] Together these factors introduce additional uncertainty when analyzing CEST data.

It has been proposed that CEST detection sensitivity can be improved substantially by expanding $\Delta\omega$ with the assistance of a paramagnetic ion.[121, 125] Paramagnetically shifted CEST agents (paraCEST agents), can in theory tolerate $k_{ex}$ and $B_1$ values up to two orders of magnitude greater than what can be achieved with diamagnetic CEST agents before CEST criteria 1 and 2 are violated, Table 6, and as a result can be detected with much greater sensitivity than conventional CEST agents. CEST agents that can tolerate larger $B_1$ without violating Criterion 2 are also more robust to $\Delta\omega$ uncertainties introduced by field inhomogeneities. However, it is in reality very challenging to fully capitalize on the theoretical advantages of paraCEST agents because the large $B_1$ required for full magnetic saturation of rapidly exchangeable protons will result in substantial RF energy deposition and tissue heating.

A number of trivalent lanthanide complexes have been evaluated as paraCEST agents, and a few representative examples are shown in Fig 10b The strong magnetic moment, high magnetic anisotropy and rapid $T_{1e}$ of paramagnetic lanthanides are ideal for expanding Δω while minimizing line broadening of the exchangeable $^1H$ resonance via $T_2$ relaxation. Complexes of $Tb^{3+}$ and $Dy^{3+}$ have been shown to generate chemical shifts as large as −600 ppm and −720 ppm, respectively,[121] Table 6.

On the other hand, given the consistent coordination chemistry across the lanthanide series, metal deposition from lanthanide-based CEST agents may reflect that which occurs when using GBCAs. For example, it was recently shown the biodistribution patterns of Gd and the pseudo-lanthanide Y were nearly identical 48 hours after administration of equal doses of the corresponding DTPA and DOTA chelates in rats.[126] Taken together, concerns of lanthanide retention and the substantially higher doses required of paraCEST agents represent substantial challenges to developing lanthanide paraCEST agents as GBCA alternatives.

Transition metal paraCEST agents are comparatively underexplored compared to lanthanide agents. High-spin $Fe^{2+}$, $Co^{2+}$, and $Ni^{2+}$ are all capable of generating large Δω that is not offset by strong paramagnetic relaxation effects. A few monomeric $Fe^{2+}$, $Co^{2+}$, and $Ni^{2+}$ complexes have been evaluated as CEST agents, Figure 10c.[127–137] The chemical shift in ppm and $k_{ex}$ of transition metal paraCEST agents are compared to representative diamagnetic CEST and lanthanide-based paraCEST agents in Table 6.

It was recently demonstrated that dinuclear complexes of ferromagnetically coupled $Cu^{2+}$ can be utilized as paraCEST agents.[138] Mononuclear complexes of $Cu^{2+}$ typically exhibit low magnetic anisotropy and long $T_{1e}$, rendering the CEST effect highly inefficient due to relaxation line broadening.[139] Ferromagnetic coupling of the otherwise well-isolated $Cu^{2+}$ spins of $Cu(L)(P_2O_7)$, Fig 10c, simultaneously induces strong enough magnetic anisotropy to achieve 29 ppm chemical shift for exchangeable amide-NHs and shortens $T_{1e}$ into the ps regime, allowing for sharp, saturable NMR resonances. The results of these studies suggest that paramagnetic ions typically utilized as relaxation agents may also be utilized as paraCEST agents when incorporated into multinuclear systems that promote magnetic superexchange coupling.

Given the low detection sensitivity of CEST agents compared to relaxation agents, it is our view that it is challenging to develop a CEST or paraCEST contrast agents that could be interchangebly used with GBCAs in any indication. However, there are a number of powerful molecular imaging applications for CEST and paraCEST agents. The majority of CEST molecular imaging to date has been performed using diamagnetic CEST agents. Chemical exchange spin-lock imaging has been used to map glucose consumption in human brain tumors.[140] Proton exchanging functional groups exhibit a pH dependence on $k_{ex}$, which can be utilized for pH mapping of pathologic tissue. CEST agents featuring two or more proton exchanging functional groups, each with a distinct Δω and pH dependence on $k_{ex}$, have been developed to evaluate pH via ratiometric analysis of saturation transfer recorded at different frequency offsets.[141] For example, the clinical X-ray contrast agent iopamidol has been used for ratiometric pH measurements in human bladder and metastatic

ovarian cancer.[142–143] ParaCEST agents have been utilized for pH mapping in rodent models of acidosis.[144–146] Enzymatically activated paraCEST agents, in which hydrolytic activity liberates proton exchanging -OH or $NH_2$ groups, have also been reported in the chemistry literature.[147–153] Modulation of paraCEST via changes in paramagnetism are discussed later in this article.

**Transition metal complexes as paraSHIFT agents.—**Exogenously administered molecules detected by direct $^1H$ or $^{19}F$ NMR observation may also be considered as GBCA alternatives. These molecules do not generate contrast between tissues and are therefore not contrast agents - they are instead referred to as chemical shift agents or probes. Tissue containing elevated concentrations of the shift agent (i.e. hyperpermeable lesions) would be detected as an $^1H$ or $^{19}F$ "hot spots."

Paramagnetic metal complexes detected by direct nuclear observation are referred to as paraSHIFT agents. Paramagnetically shifted $^1H$ resonances can be unambiguously detected without interference from endogenous $^1H$ of water (~4.8 ppm) and fat (~1.3 ppm). Paramagnetically induced $T_1$-relaxation of the $^1H$ and $^{19}F$ nuclei can enable multiple MR acquisitions can be acquired in the time frame of a conventional acquisition, effectively improving detection sensitivity relative to corresponding diamagnetic species by an order of magnitude.[154–155]

The paramagnetic requirements of an effective paraSHIFT agent mirrors those of an effective paraCEST agent - strong magnetic moment, high magnetic anisotropy, and low-relaxivity. In this regard, high-spin complexes of $Fe^{2+}$, $Co^{2+}$, and $Ni^{2+}$ have also been considered as transition-metal based $^1H$ and $^{19}F$ paraSHIFT agents, Figures 11 and 12, respectively.[112, 127, 130, 134, 156–161] The chemical shift in ppm, $T_1$ relaxation time, and full-width at half-height (directly proportional to $T_2^*$) of previously reported $^1H$ and $^{19}F$ paraSHIFT agents are summarized in Tables 7 and 8, respectively. In order to maximize detection sensitivity paraSHFIT agents are typically designed to included several chemically equivalent equivalent 1H or 19F nuclei.

It is also possible to optimize detection sensitivity of $^1H$ or $^{19}F$ nuclei through synthetic modifications. The magnitude of the pseudocontact shift of the observed nuclei is governed by both the distance from the paramagnetic ion ($r^{-3}$ dependence) and positioning relative to the metal ion's principle magnetic axis.[162–163] For transition metal complexes, contact shift contributions may also contribute to ω. Similarly, there is an $r^{-6}$ dependence on $T_2$ contributions to line broadening. Thus, there are synthetic handles available for chemists to increase ω and also tune $T_1$ and $T_2$ relaxation rates of the observed nuclei. For paraSHIFT $^{19}F$ tracers with no interfering background signal, one could envision using any paramagnetic transition metal ion provided the metal-$^{19}F$ distance is carefully optimized to balance the signal enhancing $T_1$-relaxation against offsetting $T_2$-relaxation.

The majority of in vivo imaging using chemical shift agents has utilized diamagnetic systems. Cell tracking via $^{19}F$ imaging of cells loaded with perfluorocarbon nanoemulsions (PFCNs) has been demonstrated.[164–169] Chemical shift and paraSHIFT agents are detected with low sensitivity compared to GBCAs and other relaxation agents, but PFCNs provide a

tremendous $^{19}$F payload and confinement within implanted cells enables long-acquisitions to boost $^{19}$F signal-to-noise. Pre-clinical rodent studies have been performed to quantitatively monitor pancreatic islet implantation,[168] and to monitor monocyte infiltration into multiple sclerosis lesions and head and neck carcinoas.[164–165] In a clinical trial, dendritic cells harvested from patients with colorectal cancer were engineered to present tumor specific antigens and for PFCN loading prior to intradermal auto-implantation.[166] $^{19}$F signal loss was tracked over a 24h period, corresponding to either migration or death of the $^{19}$F-labelled cells. It was recently shown that that lipophilic perfluoroalkyl functionalized complexes of high-spin $Fe^{3+}$ relaxation agents incorporated into PFCNs provide up to four-fold sensitivity gain for $^{19}$F detection.[170]

Given the low detection sensitivity of shift and paraSHIFT agents, it is more challenging to image using low molecular weight complexes that are rapidly eliminated. However, it has been demonstrated that a carefully optimized $Dy^{3+}$ paraSHIFT agents (DyL6, Figure 11A, Table 7) with 18 equivalent $^1$Hs shifted −18 ppm from water could be detected in tissues of mice following a 0.12 mmol/kg intravenous dose using MR acquisitions requiring less than 4 minutes.[171] On the other hand, the resultant in vivo images did not yield "contrast" that could be used to visualize tissue structures. It is our view that like CEST and paraCEST agents, chemical shift and paraSHIFT agents will prove most useful in molecular imaging applications to map changes in temperature change, pH, or molecular level biomarkers. The pseudocontact shift obeys a $T^{-2}$ temperature dependence and is also sensitive to changes in chemical microenvironment. For example, the 12 equivalent $^1$Hs of Tm-DOTMA (Figure 11) shift 0.57 ppm per °C, and a 0.6 mmol/kg dose of the complex was used generate maps of  T vs. reference tissue in rats (it is important to note here that the rats were fully nephrectomized to slow elimination of that $Tm^{3+}$ complex).[172] Other lanthanide paraSHIFT agents have been developed for magnetic thermometry, as well as for sensing changes in pH and $Zn^{2+}$ concentration, and one could envision using these paraSHIFT agents in an analogous fashion.

### Transition metal complexes as biochemically responsive MRI contrast agents.

**Background.—**Biochemically specific MRI contrast agents generate signal specifically in the presence of a biochemical target, enabling non-invasive detection, mapping, and in some cases quantification of pathologic changes occurring at the molecular level. One approach to biochemically specific MRI is to develop contrast agents that bind to a specific target, providing delayed signal enhancement after washout of the unbound agent. Gadolinium chelates targeted to protein targets such as fibrin,[173] type I collagen,[174] and elastin have been validated in vertebrate animal models of thrombosis,[175–177] fibrosis,[178–180] and cardiovascular tissue remodeling,[181–184] respectively. The fibrin-binding contrast agent EP2104R was tested in a Phase II clinical trial.[185]

Unfortunately, the broad utility of the target-binding approach to biochemically specific MRI is limited by the low detection sensitivity of contrast agents. Gd-based relaxation agents require concentrations  10 μM for in vivo detection and CEST and chemical shift agents are detected with substantially lower sensitivity than relaxation agents. The vast majority of imaging biomarkers are inaccessible to MR imaging via this approach. One

approach to improving the detection sensitivity of target-binding agents is to increase the Gd payload via multimerization.[29, 186] In fact, the fibrin and collagen binding probes discussed above are comprised of four and three Gd complexes conjugated to their respective target-binding moieties. However, for most imaging targets a mere doubling or tripling of $r_1$ per target-binding moiety is insufficient for MR conspicuity. High-molecular weight macromolecular structures containing very high signal generator payloads can be developed, but this will greatly alter the pharmacokinetics and time course of imaging time.

Another approach is to develop contrast agents that modulate the MR signal in the presence of a specific biochemical signature. The biochemically stimulated signal change occurs following a chemical reaction that alters the mechanisms governing $T_1$-relaxation, CEST, or pseudo-contact shift. Biochemically responsive lanthanide-based agents have been developed to respond to changes in pH,[187–188] metal ion or neurotransmitter concentrations, [189–194] redox potential,[195–196] enzymes expressed by reporter genes,[197–199] and enzyme markers of injury or disease.[148–149, 153, 200–202] Although enzyme concentrations are well below the threshold for direct detection with target-binding agents, catalytic action on biochemically responsive agents can result in meaningful signal change.

There are a number of important criteria to consider when designing a biochemically responsive agent for in vivo use. First, the "activated" or "on" form of the agent must be detectable at concentrations that can be achieved within the tissue studied by the imaging experiment. Second, the signal change achieved between the "off" and "on" states must be large enough so that the biochemically triggered signal change can be interpreted unambiguously. MR signal enhancement by relaxation and CEST agents are functions of both agent concentration and $r_1$ or magnetization transfer efficiency, respectively. The biochemically triggered signal change must well exceed differences in signal enhancement that could result from variations in tissue concentration. For chemical shift agents, the chemical shift difference between the "off" and "on" states must be large enough that signal from the "off" state does not contaminate imaging weighted to signal from the "on" state. Third, a biochemically triggered response must be fast relative to the pharmacokinetics of the agent so that detectable concentrations of the activated agent can accumulate in vivo. Additionally, the agent should be robust against degradation both prior to and after biochemical activation. The agent should also be non-toxic. Our discussion below will focus on chemistry to address detection sensitivity and magnitude of signal response.

Biochemically responsive relaxation agents offer a clear advantage to detection sensitivity over agents detected by CEST or direct nuclear observation. Over the last two decades, innovative chemistry has been applied to develop dozens of biochemically responsive Gd-based relaxation agents, and some Gd-based agents have been advanced to successfully image pH change,[203–204] $Zn^{2+}$ flux,[205–206] and enzyme activities[199, 207–210] in vertebrate animal models. However, the magnitude of $r_1$ response are typically very low for Gd-based agents. Gd chelates are strong relaxation agents even prior to biochemical activation and only a few of the agents developed to date can achieve a 2-fold increase in the presence of clinically relevant concentrations of biochemical stimuli. The Gd-based agents capable of generating the largest $r_1$ change undergo reactions that result in oligomerization or protein binding, with $r_1$ increasing resulting from longer $\tau_R$. However, the $r_1$ boost conferred to Gd

via $\tau_R$ increase is strongest at $B_0 < 1.5$ T, and the effect diminishes precipitously with increasing field strength. For example, the myeloperoxidase sensing agent Gd-MPO, Figure 13, which is forms higher molecular weight oligomers following myeloperoxidase mediated oxidation of the 5-hydroxytryptamine functional group, receives a 2.4-fold $r_1$ increase from 4.3 mM$^{-1}$s$^{-1}$ to 10.5 mM$^{-1}$s$^{-1}$ at 0.47T , but $r_1$ is virtually unchanged by oligomerization at 4.7T, Table 9. Similarly, the blood plasma $r_1$ of the Zn$^{2+}$ sensing agent Gd-L1Zn, Fig 12, which binds Zn$^{2+}$ and subsequently associates with serum albumin, increases 3.1-fold upon Zn$^{2+}$ binding from 5.8 mM$^{-1}$s$^{-1}$ to 18 mM$^{-1}$s$^{-1}$ at 0.50T, but the r$_1$ increase is only 10% at 9.4T. Most of the Zn$^{2+}$ and enzymatically activated agents used in vivo undergo stimuli responsive protein binding or polymerization – selective tissue enhancement is due largely to retention of the activated agent at delayed time points.

The challenge to implementing biochemically responsive agents that provide small $r_1$ change is exemplified by imaging experiments to map pH in rat models of renal acidosis and glioblastoma using the pH sensing agent Gd-DOTA-4AmP, Fig 13. Gd-DOTA-4AmP $r_1$ increases by ~5% per 0.1 pH unit decrease between pH 7.4 and 6.0. Equally large signal change could be generated by small differences in Gd-DOTA-4AmP concentration. In vivo experimentation required a dual probe approach in which a pH-unresponsive agent with similar pharmacokinetics was injected and washed out before injection of Gd-DOTA-4AmP. The dynamic imaging data from the pH-unresponsive agent was used to estimate concentration of the pH sensor agent, and the pH maps were generated from Gd-DOTA-4AmP enhanced signal change normalized to estimated concentration.[203–204] This dual probe approach provides an innovative solution to correct for variations in tissue concentration of Gd-DOTA-4AmP, but would be very difficult to implement in a clinical setting due to time constraints and safety concerns of doubling metal ion exposure.

Unlike Gd relaxation agents, it theoretically possible to achieve a true "off/ on" effect with CEST or chemical shift agents. In practice, the low detection sensitivity of CEST agents severely limits the dynamic range for biochemically mediated signal modulation.

There is a growing interest in developing transition metal complexes as biochemically responsive MRI contrast agents. The multiple oxidation states and electron spin configurations available to transition metals, each with unique paramagnetic properties and disparate structural preferences, offer exciting mechanisms by which to modulate MR signal response. Innovative examples highlighting the exciting opportunities for MRI contrast offered by transition metal chemistry are discussed below.

**Transition metal complexes as biochemically responsive relaxation agents.—**
Biochemically activated Gd-based relaxation agents undergo $r_1$ change in response to chemical reactions that alter either $q$, $\tau_m$, or $\tau_R$, Table 9. Using transition metals, it is theoretically possible to impact multiple relaxation mechanisms simultaneously via biochemical triggered change in oxidation state. For example, one could envision changing $S$, $q$, and even modulating the influence of $\tau_R$ simply by switching between Mn$^{3+}$ and Mn$^{2+}$ oxidation states. The Mn$^{3+}$ ion has a strong preference for octahedral geometry and complexes comprising hexadentate ligands will likely result in a $q$=0 system, whereas Mn$^{2+}$ is a substantially larger ion that can accommodate coordination number 7, thus enabling

hexadentate ligands to form complexes of $q$=1. Given the asymmetric ground state electronic distribution of the $Mn^{3+}$ ion it is also expected that $T_{1e}$ will contribute substantially to $\tau_C$, thus limiting the capability to improve $r_1$ by slowing $\tau_R$ change.[211] On the other hand, $T_1$-relaxation by $Mn^{2+}$ complexes are typically controlled by $\tau_R$, and one could envision further amplifying the $Mn^{3+}$ vs $Mn^{2+}$ $r_1$ incorporating the $Mn^{3+/2+}$ complex into higher molecular weight structures.

Initial proof of concept for MR signal modulation with a redox active Mn complex was demonstrated using $Mn^{3+/2+}$-TPPS$_4$, Fig 14. $Mn^{3+/2+}$-TPPS$_4$ was evaluated as a $p$O$_2$ sensor, with $Mn^{2+}$ vs $Mn^{3+}$ composition reflecting $p$O$_2$ between 0 and 40 torr O$_2$.[211] Between 0.47T and 3T at 25 °C the $Mn^{3+}$-TPPS$_4$ $r_1$ ranges from 12 to 10 $mM^{-1}s^{-1}$ and $Mn^{2+}$- TPPS$_4$ ranges 10 to 8 $mM^{-1}s^{-1}$ (remember the "anomalously" high relaxivity of $Mn^{3+}$ porphyrins).[92] Because $Mn^{3+/2+}$-TPPS$_4$ does not undergo any substantial structural change upon oxidations state change and because the r1 of Mn3+ porphyrins exceed that predicted by the $S(S+1)/r_{MH}^6$ component of Equation 3, switching from $Mn^{2+}$-TPPS$_4$ to $Mn^{3+}$-TPPS$_4$ effects only a modest $r_1$ change. However, a substantially larger 2.5-fold $r_1$ difference was achieved by formation of a macromolecular adduct with $\beta$-cyclodextran. Upon association with $\beta$-cyclodextran, the 0.47T relaxivity of $Mn^{3+}$- TPPS$_4$ and $Mn^{2+}$- TPPS$_4$ increase to 23 $mM^{-1}s^{-1}$ and 58 $mM^{-1}s^{-1}$, corresponding to 2.3-fold and 4.8-fold r1 increase, respectively. The improved $r_1$ response achieved by association of $Mn^{3+/2+}$-TPPS$_4$ with a macromolecular system highlights how $Mn^{3+}$ $T_{1e}$ is fast relative to $Mn^{2+}$ $T_{1e}$ at 0.47T, thus rendering the $Mn^{3+}$ relaxivity less responsive to changes in $\tau_R$.

A series of ligands HBET-**R** and CyHBET-**R**, Fig 14, were designed to support isolable complexes of both $Mn^{3+}$ and $Mn^{2+}$, which are stabilized by different ligand environments. Ligands like EDTA support stable complexes of $Mn^{2+}$, but cannot stabilize $Mn^{3+}$, which will disproportionate to $Mn^{2+}$ and $Mn^{4+}$. On the other hand, $Mn^{3+}$ is stabilized by ligands featuring more electron releasing donors, like TPPS$_4$ or the bis-phenolate ligands HBED and EHPG. Both ligands stabilize $Mn^{3+}$ exclusively under aerobic conditions.[211–212] Based on the $Mn^{3+}$ and $Mn^{2+}$ stabilizing preferences of HBED and EDTA, it was hypothesized that the structurally analogous HBET-**R** and CyBET-**R** ligands featuring 3 carboxylates and 1 phenolate pendant donor would stabilize both oxidation states.[213–214] It was also hypothesized that this class of ligands would also enable $q$ modulation upon switching between $Mn^{3+}$ and $Mn^{2+}$. A total of six HBET-**R** and CyBHET-**R** systems were studied (**R** = -H, -OMe, -NO$_2$), and all could be isolated in both the $Mn^{3+}$ and $Mn^{2+}$ oxidation states, with the exception of complexes where **R** = -OMe, which were only isolable in $Mn^{2+}$ form, as described below. The HBET-**R** and CyHBET-**R** ligands form 7-coordinate ternary $Mn^{2+}$ complexes with a rapidly exchanging water co-ligand. The corresponding $Mn^{3+}$ complexes are believed to be $q = 0$, analogous to $Mn^{3+}$-EHPG.[215] For this series of complexes, reduction from $Mn^{3+}$ to $Mn^{2+}$ results in $r_1$ increase ranging from 2.5-fold to 8.2-fold, at 1.4T and 37 °C. The effect is field independent, with a comparable turn-on effect achieved at 4.7T.

$Mn^{3+}$ complexes of the HBET-**R** and CyHBET-**R** series reduce to $Mn^{2+}$ instantaneously upon dissolution in blood plasma. The $Mn^{3+/2+}$ redox potentials are >500 mV more positive than the thiol/disulfide couples that govern biological redox, and thus favor $Mn^{2+}$

exclusively in biological milieu. Attempts to depress the redox potential via phenolate **R**-substituents destabilizes the phenolate-ligands with respect to redox. For example, the $Mn^{3+}$-HBET-$p$-OMe can be transiently generated and observed via one electron oxidation with potassium ferricyanide, but undergoes ligand-metal auto-redox resulting in oligomeric $Mn^{2+}$ species.[213] However, $Mn^{3+}$-phenolate auto-redox can also be a productive mechanism for biochemically responsive MRI contrast. For example, treatment of the complex $Mn^{2+}$-HPTP1 with $H_2O_2$, yields transiently a brown intermediate (likely the corresponding $Mn^{3+}$ complex) that rapidly converts to a C-C linked dinuclear complex with a concomitant $r_1$ change, Figure 15.[216]

A different approach to stabilizing both $Mn^{3+}$ and $Mn^{2+}$ has been pursued using the complex Mn-JED, in which the ligand undergoes redox triggered isomerization between $Mn^{2+}$ stabilizing "BPED-like" binding mode and $Mn^{3+}$ stabilizing "HBED-like" binding modes. [217] The JED ligand stabilizes both the $Mn^{3+}$ and $Mn^{2+}$ ligands in blood plasma, with little spontaneous interconversion between oxidation states observed over the course of 24 h. Relaxivity measurements in blood plasma demonstrate 9-fold greater $r_1$ for $Mn^{2+}$-JED vs. $Mn^{3+}$-JED. Although JED stabilizes both $Mn^{3+}$ and $Mn^{2+}$, $Mn^{2+}$-JED is rapidly and cleanly converted to $Mn^{3+}$-JED in the presence of peroxidase enzyme activity. The reaction is reversible, as $L$-cysteine mediates reduction of $Mn^{3+}$-JED to $Mn^{2+}$-JED.

$Fe^{3+/2+}$ redox has also been considered as a mechanism to generate biochemically responsive MRI contrast. As described above, high-spin complexes of $Fe^{3+}$ are very effective relaxation agents. On the other hand, complexes of $Fe^{2+}$ are much less effective relaxation agents. For high-spin $Fe^{2+}$, $r_1$ is limited by short $T_{1e}$, and low spin $Fe^{2+}$ is diamagnetic.[218] The chelate Fe-PyC3A was demonstrated to be a highly effective redox responsive MRI contrast agent.[110] PyC3A forms a ternary complex with high-spin $Fe^{3+}$ and a rapidly exchanging water co-ligand, resulting in a $r_1$ ranging between 1.8 to 2.2 mM$^{-1}$s$^{-1}$ between 1.4 T and 11.7 T at 37 °C. $r_1$ for the sister $Fe^{2+}$-PyC3A chelate ranges 0.15 to 0.18 mM$^{-1}$s$^{-1}$, a full order of magnitude lower. The $Fe^{3+}$-PyC3A vs. $Fe^{2+}$-PyC3A relaxivity difference is large enough to provide a virtual "turn off/ turn on" effect as demonstrated in Figure 16, which shows MR images of phantoms containing water, 0.5 mM $Fe^{2+}$-PyC3A, and $Fe^{3+}$-PyC3A. Contrast agent concentrations of 0.5 mM or greater are achieved in tissues in vivo following a standard dose of a low-molecular weight agent. The $Fe^{2+}$-Py3A containing solution is barely contrast enhanced compared to water, whereas the $Fe^{3+}$-PyC3A containing solution is strikingly hyperintense.

$Fe^{2+}$-PyC3A is rapidly oxidized by $H_2O_2$. In this regard, $Fe^{2+}$-PyC3A was evaluated as a sensor for ROS in vivo in a mouse model of pancreatic inflammation. Molecular imaging of ROS has been proposed as biomarker for acute inflammation. Neutrophils that infiltrate inflamed tissue secrete high levels of reactive oxygen species (ROS) via respiratory burst as well as myeloperoxidase, which catalyzes the conversion of respiration-derived ROS into highly deleterious sources of electrophilic oxygen, like ferryl heme and hypochlorous acid. For the study, pancreatic vs. adjacent muscle contrast to noise ratios (CNR) were quantified following injection of 0.2 mmol/kg $Fe^{2+}$-PyC3A into either a mouse model of pharmacologically induced pancreatic inflammation (caerulein/ lipopolysaccharide model), [219] or to control mice treated only with saline (normal pancreas). As a negative control, mice

with pancreatic inflammation were imaged with an equal volume dose of 0.02 mmol/kg dose of $Mn^{2+}$-PyC3A (solution "$T_1$ matched" to $Fe^{2+}$-PyC3A), which does not react with ROS. The results of the imaging study are shown in Fig 17. Prior to contrast injection, the signal arising from the pancreas and nearby tissues like liver are comparable. Little enhancement is observed after injection of $Fe^{2+}$-PyC3A to mice with normal pancreas, or after injection of the $T_1$-matched $Mn^{2+}$-PyC3A dose to mice with inflamed pancreas. On the other hand, the inflamed pancreatic tissue is strongly and selectively enhanced after injection of $Fe^{2+}$-PyC3A. Importantly, contrast enhancement of the pancreas correlated tightly with ex vivo quantitation of pancreatic myeloperoxidase activity levels.

**Transition metal complexes as biochemically responsive paraCEST agents.—**
Structural and paramagnetic differences between transition metal oxidation states can also be used to biochemically modulate CEST. For example, the ligand TPT supports low-spin diamagnetic complexes of $Co^{3+}$ but high-spin paramagnetic complexes of $Co^{2+}$ that shift the magnetically saturable pyrazole-NH protons 135 ppm from the bulk water resonance,[220] Fig 18. Oxidation state interchange enables a true "off/ on" CEST effect. The $Co^{3+/2+}$-TPT redox potential of −107 mV vs. NHE enables oxidation and reduction in the presence of $O_2$ and $L$-cystine, respectively.

Oxidation state interchange resulting in distinct paramagnetically shifted resonances for labile, magnetically saturable protons can be capitalized on for ratiometric quantitation of biochemical properties. For example, the dinuclear complex $Fe_2L$(etidronate), Fig 18, supports $Fe^{2+}Fe^{2+}$ and $Fe^{3+}Fe^{2+}$ oxidation state configurations that exhibit CEST enhancement at saturation frequencies of 83 ppm and 40 ppm, respectively, which enable quantitation of microenvironment redox potential via ratiometric analysis of distinct CEST signals.[221] As with the dinuclear $Cu^{2+}:Cu^{2+}$ complex $Cu_2(L)(P_2O_7)$ discussed above, $Fe^{3+}$ $T_{1e}$ is substantially reduced via magnetic coupling interactions with $Fe^{2+}$. In vitro proof of concept for this ratiometric imaging approach was demonstrated through spectroscopic measurements performed on solutions of defined $L$-cysteine and potassium superoxide composition, which mediate reduction to $Fe^{2+}Fe^{2+}$ and oxidation to $Fe^{3+}Fe^{2+}$, respectively. The ratio of % CEST enhancement arising from magnetic saturation at frequencies corresponding to oxidized and reduced agents correlated strongly with the solution open circuit potential determined by electrode readings.[221]

The CEST effect can also be modulated by spin crossover phenomena. The $Fe^{2+}$ complexes Fe-3-BPP and Fe-$Me_2$NPY5$Me_2$, Fig 18, exhibit spin crossover from low-spin to high-spin in the 20 °C to 60 °C temperature range, which results in a 0.23 ppm per °C and 1.0 ppm per °C shift for the $^1H$ resonances of labile, saturable imidazole-NHs or water co-ligand, respectively.[222] This temperature dependent spin crossover behavior could potentially be utilized in MR thermometry applications to aid in minimally invasive thermal therapy targeted at solid tumors.

**Transition metal complexes as biochemically responsive paraSHIFT agents.—**
Metal ion redox has also been utilized as an activation mechanism for paraSHIFT agents. For example, it was shown that $H_2O_2$ mediated oxidation of high-spin $Co^{2+}$-NODACF$_3$ to low-spin $Co^{3+}$-NODACF$_3$ by $H_2O_2$ triggers a 4 ppm chemical shift of the -$C^{19}F_3$ resonance,

Fig 19.[223] The chelates $Co^{2+}$-NODA-C(CF$_3$)$_3$ and $Co^{2+}$-MSCI-C(CF$_3$)$_3$ offer a 3-fold increase in $^{19}F$ payload and interestingly achieve a nearly 10 ppm $^{19}F$ chemical shift upon oxidation by $H_2O_2$ and $H_2O_2$/peroxidase, respectively.[224–225]

$Cu^{2+}/Cu^{1+}$ redox has been used to trigger $^{19}F$ signal turn on in response to biochemical reduction. In this regard, the hypoxia specific positron emission tomography (PET) tracer $^{64}Cu^{2+}$-ATSM, which is selectively reduced to $Cu^+$-ATSM within hypoxic cells,[226] has been adapted as an $^{19}F$ chemical shift agent for MRI, Fig 19. The $Cu^+$ complex undergoes facile dissociation compared to $Cu^{2+}$-ATSM, resulting in cellular retention of Cu in hypoxic tissues. In PET scans, hypoxic regions appear as positron emitter "hot spots" during late time points after washout of unreacted $Cu^{2+}$-ATSM.[227] The $^{19}F$ MR tracer $Cu^{2+}$-ATSM-F$_3$ is detected via $^{19}F$ signal turn on under conditions of hypoxia. The $^{19}F$ resonances of $Cu^{2+}$-ATSM are not MR visible due to strong relaxation properties of $Cu^{2+}$, which results in extreme $^{19}F$ line broadening, but reduction to $Cu^+$ results in $^{19}F$ signal turn on. NMR studies performed on MCF-7 cells incubated with $Cu^{2+}$-ATSM-CF$_3$ demonstrated a $^{19}F$ turn-on effect that was specific to hypoxic conditions.[228] The sensitivity and cell-permeability of $Cu^{2+}$-ATSM derived $^{19}F$ agents was improved by increasing $^{19}F$ payload and lipophilicity, Fig 19.[229] A $Cu^{2+}$ reduction approach was applied to the $^{19}F$ labelled complexes $Cu^{2+}$-LRF1 and $Cu^{2+}$-LRF2, Fig 19, which are reduced from the $Cu^{2+}$ to $Cu^+$ oxidation state in the presence of *L*-cysteine resulting in $^{19}F$ signal turn on.[230]

Biochemically triggered changes in *d*-electron spin configuration can also effect profound changes in $^{19}F$ chemical shift. For example. Deprotonation of the 3,5-dimethyl-4-hydroxypyridine donor groups (pKa 6 at 37 °C) in $^{19}F$ labelled $Fe^{2+}$ complex Fe-PY3OH, Fig 19, trigger a switch from low-spin to high-spin $Fe^{2+}$, accompanied by a 13.5 ppm shift in the $^{19}F$ resonance per pH unit.

## Summary and Outlook.

Contrast enhanced MRI is an indispensable tool for contemporary diagnostic medicine as well as non-clinical and pre-clinical biomedical research. Contrast agent design has traditionally centered around lanthanide complexes, but recent concerns over GBCA toxicity have inspired chemists to consider paramagnetic transition metal complexes in the context of MRI contrast. Simultaneously, increasingly personalized advances in patient care will require imaging that delivers increasingly specific cellular and molecular level information. Reaction-based manipulation of transition metal paramagnetism, enables $T_1$-weighted signal modulation that exceeds what is possible using Gd-based relaxation agents, and offers a powerful mechanism by which to turn CEST and chemical shift effects "off" and "on". The field of MRI contrast agents offers a number of exciting opportunities for inorganic chemists interested in applying transition metal chemistry to biomedical imaging research.

## ACKNOWLEDGMENT

## AUTHOR BIOS

**Abhishek Gupta** completed his B.Sc (Hons I) in medical nanotechnology in 2012 and graduated with a PhD in 2016 from Western Sydney University (WSU) and the Commonwealth Scientific and Industrial Research Organisation, Australia. He is currently working as a postdoctoral research fellow at WSU and Ingham Institute (Liverpool Hospital), Australia, where he is developing responsive self-assembled nanoparticulate contrast agents for integrated MRI-linear accelerator systems. His current research interests also lie in the development of Gd-free MRI contrast agents and the advancement of the theory and applications of NMR, MRI and field-cycling relaxometry.

**Peter Caravan** is Professor of Radiology at Harvard Medical School and Co-Director of the Institute for Innovation in Imaging at Massachusetts General Hospital. A native of Bay Roberts, Newfoundland, he received a B.Sc.(Hons) from Acadia University and a Ph.D. in Chemistry from the University of British Columbia working with Chris Orvig. After post-doctoral work with André Merbach at the Université de Lausanne, he joined Epix Medical, a specialty biopharma focused on targeted MRI contrast agents, before joining the faculty of Harvard Medical School and A. A. Martinos Center for Biomedical Imaging at Massachusetts General Hospital in 2007. He has a longstanding interest in the chemistry, biophysics, and application of contrast agents.

**William S. Price** received his BSc(Hons), PhD and DSc degrees from the University of Sydney in 1986, 1990 and 2012, respectively. After postdoctoral study at the Institute of Atomic and Molecular Science in Taipei, Taiwan and the National Institute of Material and Chemical Research in Tsukuba, Japan he joined the Water Research Institute in Tsukuba, Japan in 1995 and became Chief Scientist in 1996. In 2000 he went for a year at the Royal Institute of Technology (KTH) with Prof. Peter Stilbs. In 2001 he returned to Japan as Professor of Chemistry at Tokyo Metropolitan University. At the end of 2003 he returned to Australia and is currently Professor of Medical Imaging Physics at Western Sydney University. His interests focus on the development and application of NMR techniques (pulsed gradient spin-echo (PGSE) NMR, NMR relaxation and MRI) to the study of molecular dynamics in chemical and biochemical systems. He has more than 190 peer reviewed publications.

**Carlos Platas Iglesias** graduated in Chemistry at the University of Santiago de Compostela and obtained a Ph.D. at the University of A Coruña in 1999. After working as a postdoctoral researcher at the University of Lausanne (Switzerland) and Delft University of Technology (The Netherlands) he returned to A Coruña, were he currently holds a position as Associate Professor of Inorganic Chemistry. His research interests are related to the application of coordination chemistry principles to design metal complexes with predetermined stability, kinetic, optical or magnetic properties, including contrast agents for Magnetic Resonance Imaging.

**Eric M. Gale** graduated with a bachelor's degree in chemistry from Rutgers University in 2006 and received his PhD in chemistry from the University of Georgia in 2012 under the mentorship Todd Harrop. He trained as a postdoc under the mentorship Peter Caravan from

2012–2015. Eric is currently an Assistant Professor in Radiology at Massachusetts General Hospital and Harvard Medical School, where he applies chemistry to solve problems related to radiology and biomedical imaging. A major focus of his current research involves design, physicochemical characterization and pre-clinical evaluation of transition metal complexes as biochemically responsive MRI contrast agents.

## REFERENCES

1. Wahsner J; Gale EM; Rodriguez-Rodriguez A; Caravan P, Chemistry of MRI Contrast Agents: Current Challenges and New Frontiers. Chem. Rev 2019, 119 (2), 957–1057. [PubMed: 30350585]

2. Moon M; Cornfield D; Weinreb J, Dynamic Contrast-Enhanced Breast MR Imaging. Magn. Reson. Imaging Clin. N. Am 2009, (17), 2.

3. Essig M; Dinkel J; Gutierrez JE, Use of Contrast Media in Neuroimaging. Magn. Reson. Imaging Clin. N. Am 2012, 20, 633–648. [PubMed: 23088943]

4. Yang S; Law M; Zagzag D; Wu HH; Cha S, Dynamic Contrast-Enhanced Perfusion MR Imaging Measurements of Endothelial Permeability: Differentiation between Atypical and Typical Meningiomas. Am. J. Neuroradiol 2003, 24, 1554–1559. [PubMed: 13679270]

5. Choi JY; Lee JM; Sirlin CB, CT and MR Imaging Diagnosis and Staging of Hepatocellular Carcinoma: Part I. Development, Growth, and Spread: Key Pathologic and Imaging Aspects. Radiology 2014, 272 (3), 634–653.

6. Essig M; Anzalone N; Combs SE; Dorfler A; Lee S-K; Picozzi P; Rovira A; Weller M; Law M, MR Imaging of Neoplastic Central Nervous System Lesions: Review and Recommendations for Current Practice. Am. J. Neuroradiol 2012, 33 (5), 803–817. [PubMed: 22016411]

7. Kim SY; Cho N; Shin SU; Lee HB; Han W; Kwon BR; Kim SY; Lee SH; Chang JM; Moon WK, Contrast-enhanced MRI after neoadjuvant chemotherapy of breast cancer: lesion-to background parenchymal signal enhancement ratio for discriminating pathological complete response from minimal residual tumou. Eur. Radiol 2018, 28 (7), 2986–1995. [PubMed: 29380033]

8. Gale EM; Caravan P; Rao AG; McDonald RJ; Winfeld M; Fleck RJ; Gee MS, Gadolinium-based contrast agents in pediatric magnetic resonance imaging. Pediatr Radiol 2017, 47 (5), 507–521. [PubMed: 28409250]

9. European Medicine Agency https://www.ema.europa.eu/en/documents/press-release/emas-final-opinion-confirms-restrictions-use-linear-gadolinium-agents-body-scans_en.pdf. (accessed 26 June 2019).

10. Burai L; Toth E; Seibig S; Scopelliti R; Merbach AE, High-pressure NMR kinetics, part 95 - Solution and solid-state characterization of Eu-II chelates: A possible route towards redox responsive MRI contrast agents. Chemistry-a European Journal 2000, 6 (20), 3761–3770.

11. Gamage NDH; Mei YJ; Garcia J; Allen MJ, Oxidatively Stable, Aqueous Europium(II) Complexes through Steric and Electronic Manipulation of Cryptand Coordination Chemistry. Angew. Chem.-Int. Edit 2010, 49 (47), 8923–8925.

12. Lauffer RB, Paramagnetic metal complexes as water proton relaxation agents for NMR imaging: theory and design. Chem. Rev 1987, 87 (5), 901–927.

13. Grobner T; Prischl FC, Gadolinium and nephrogenic systemic fibrosis. Kidney Int 2007, 72 (3), 260–264. [PubMed: 17507905]

14. Marckmann P; Skov L; Rossen K; Dupont A; Damholt MB; Heaf JG; Thomsen HS, Nephrogenic systemic fibrosis: suspected causative role of gadodiamide used for contrast-enhanced magnetic resonance imaging. J. Am. Soc. Nephrol 2006, 17 (9), 2359–2362. [PubMed: 16885403]

15. Kanda T; Fukusato T; Matsuda M; Toyoda K; Oba H; Kotoku J; Haruyama T; Kitajima K; Furui S, Gadolinium-based contrast agent accumulates in the brain even in subjects without severe renal dysfunction: evaluation of autopsy brain specimens with inductively coupled plasma mass spectroscopy. Radiology 2015, 276 (1), 228–232. [PubMed: 25942417]

16. Layne KA; Dargan PI; Archer JRH; Wood DM, Gadolinium deposition and the potential for toxicological sequelae – A literature review of issues surrounding gadolinium-based contrast agents. British J. Clin. Pharmacol 2018, 84 (11), 2522–2534.

17. Bao W; Jia H; Finnema S; Cai Z; Carson RE; Huang YH, PET Imaging for Early Detection of Alzheimer's Disease: From Pathologic to Physiologic Biomarkers. PET Clin 2017, 12 (3), 329–350. [PubMed: 28576171]

18. Hammes J; Bischof GN; Drzezga A, Molecular imaging in early diagnosis, differential diagnosis and follow-up of patients with neurodegenerative diseases. Clin. Transl. Imaging 2017, 5, 465–471.

19. Bauckneht M; Capitanio S; Raffa S; Roccatagliata L; Pardini M; Lapucci C; Marini C; Sambuceti G; Inglese M; Gallo P; Cecchin D; Nobili F; Morbelli S, Molecular imaging of multiple sclerosis: from the clinical demand to novel radiotracers. EJNMMI Radiopharm. Chem 2019, 4, 6. [PubMed: 31659498]

20. Lindner JR; Sinusas A, Molecular imaging in cardiovascular disease: Which methods, which diseases? J Nucl Cardiol 2013, 20 (6), 990–1001. [PubMed: 24092271]

21. Jeraj R; Bradshaw T; Simoncic U, Molecular Imaging to Plan Radiotherapy and Evaluate Its Efficacy. J. Nucl. Med 2015, 56, 1752–1765. [PubMed: 26383148]

22. Shah K; Jacobs A; Breakefield XO; Weissleder R, Molecular imaging of gene therapy for cancer. Gene Therapy 2004, 11, 1175–1187. [PubMed: 15141158]

23. Shukla AK; Kumar U, Positron emission tomography: An overview. J. Med. Phys 2006, 31 (1), 13–21. [PubMed: 21206635]

24. Moses WM, Fundamental Limits of Spatial Resolution in PET. Nucl. Instrum. Methods Phys. Res. A 2011, 648, S236–S240. [PubMed: 21804677]

25. Edelman RR; Hesselink JR; Zlatkin MB; Crues JV III, Clinical Magneic Resonance Imaging - Volume 3 Elsevier Health: St. Louis, 2006.

26. Caravan P, Strategies for increasing the sensitivity of gadolinium based MRI contrast agents. Chemical Society Reviews 2006, 35 (6), 512–523. [PubMed: 16729145]

27. Botta M; Carniato F; Esteban-Gomez D; Platas-Iglesias C; Tei L, Mn(II) compounds as an alternative to Gd-based MRI probes. Future Med. Chem 2019, 11 (12), 1461–1483. [PubMed: 31298575]

28. Aime S; Botta M; Esteban-Gomez D; Platas-Iglesias C, Characterisation of magnetic resonance imagine (MRI) contrast agents using NMR relaxometry. Mol. Phys 2019, 117 (7–8), 898–909.

29. Li H; Meade TJ, Molecular Magnetic Resonance Imaging with Gd(III)-Based Contrast Agents: Challenges and Key Advances. J. Am. Chem. Soc 2019, 141 (43), 17025–17041. [PubMed: 31593630]

30. Heffern MC; Matosziuk LM; Meade TJ, Lanthanide Probes for Bioresponsive Imaging. Chemical Reviews 2014, 114, 4496–4539. [PubMed: 24328202]

31. Pellico J; Ellis CM; David JJ, Nanoparticle-Based Paramagnetic Contrast Agents for Magnetic Resonance Imaging. Contrast Media & Molecular Imaging 2019, 2019 (1845637), 1–13.

32. Estelrich J; Sanchez-Martin MJ; Busquts MA, Nanoparticles in magnetic resonance imaging: from simple to dual contrast agents. Int. J. Nanomed 10 (1727–1741), 1727.

33. J., D.-L.; Łazarczyk A; Hałubiec P; Szafra ski O; Kamas K; Karewicz A, Superparamagnetic Iron Oxide Nanoparticles-Current and Prospective Medical Applications. Materials 2019, 12 (4), E617. [PubMed: 30791358]

34. Grobner T, Gadolinium – a specific trigger for the development of nephrogenic fibrosing dermopathy and nephrogenic systemic fibrosis? Nephrol. Dial. Transplant 2006, 21 (4), 1104–1108. [PubMed: 16431890]

35. Committee, A., Gadolinium-Based Contrast Agents and Nephrogenic Systemic Fibrosis FDA Briefing Document 2009.

36. Bennett CL; Qureshi ZP; Sartor AO; Norris LB; Murday A; Xirasagar S; Thomsen HS, Gadolinium-induced nephrogenic systemic fibrosis: the rise and fall of an iatrogenic disease. Clin. Kidney J 2012, 5 (1), 82–88. [PubMed: 22833806]

37. Solomon RJ; Natarajan MK; Doucet S; Sharma SK; Staniloae CS; Katholi RE; Gelormini JL; Labinaz M; Moreyra AE, Cardiac angiography in renally impaired patients (CARE) study: a randomized double-blind trial of contrast-induced nephropathy in patients with chronic kidney disease. Circulation 2007, 115 (25), 3189–3196. [PubMed: 17562951]

38. Persson PB; Hansell P; Liss P, Pathophysiology of contrast medium-induced nephropathy. Kidney Int 2005, 68 (1), 14–22. [PubMed: 15954892]

39. United States Renal Data System, 2016 USRDS Annual Data Report Volume 1: Chronic Kidney Disease in the United States National Institutes of Health, National Institue of Diabetes Digestive and Kidney Diseases: Bethesda, MD, 2016.

40. United States Renal Data System, 2016 USRDS Annual Data Report Volume 2: End-Stage Renal Disease in the United States National Institues of Health, National Instutide of Diabetes Digestive and Kidney Diseases: Bethesda, MD, 2016.

41. Kanda T; Kawaguchi H, Hyperintense dentate nucleas and globus pallidus on unenhanced T1-weighted MR images are associated with gadolinium-based contrast media. Neuroradiology 2013, 55, 1268–1269.

42. Kanda T; ishii K; Kawaguchi H; Kitajima K; Takenaka D, High signal intensity in the dentate nucleus and globus pallidus on unenhanced T1-weighted MR images: relationship with increasing cumulative dose of a gadolinium-based contrast material. Radiology 2014, 270, 834–841. [PubMed: 24475844]

43. Kanda T; Osawa M; Oba H; Toyoda K; Kotoku J; Haruyama T, High signal intensity in dentate nucleus on unenhanced T1-weighted MR images: association with linear versus macrocyclic gadolinium chelate administration. Radiology 2015, 275, 803–809. [PubMed: 25633504]

44. US Food and Drugs Administration https://www.fda.gov/drugs/drug-safety-and-availability/fda-drug-safety-communication-fda-warns-gadolinium-based-contrast-agents-gbcas-are-retained-body. (accessed 26 June 2019).

45. Kanda T, The new restrictions on the use of linear gadolinium-based contrast agents in Japan. Magn. Reson. Med. Sci 2019, 18 (1), 1–3. [PubMed: 29553066]

46. Australian Therapeutic Good Administration https://www.tga.gov.au/alert/gadolinium-based-contrast-agents-mri-scans. (accessed 26 June 2019).

47. Semelka RC; Ramalho J; Vakharia A; AlObaidy M; Burke LM; Jay M; Ramalho M, Gadolinium deposition disease: Initial description of a disease that has been around for a while. Magn Reson Imaging 2016, 34 (10), 1383–1390. [PubMed: 27530966]

48. Semelka RC; Commander C; Jay M; Burke LMB; Ramalho M, Presumed Gadolinium Toxicity in Subjects With Normal Renal Function: A Report of 4 Cases. Invest Radiol 2016, 51 (10), 661–665. [PubMed: 27548344]

49. Semelka RC; Ramalho M; Jay M; Hickey L; Hickey J, Intravenous Calcium-/Zinc-Diethylene Triamine Penta-Acetic Acid in Patients With Presumed Gadolinium Deposition Disease: A Preliminary Report on 25 Patients. Invest. Radiol 2018, 53 (6), 373–379. [PubMed: 29419708]

50. Chandra T; Pukenas B; Mohan S; Melhem E, Contrast-Enhanced Magnetic Resonance Angiography. Magn. Reson. Imaging Clin. N. Am 2012, 20, 687–698. [PubMed: 23088945]

51. Jackson A; O'Connor JPB; Parker GJM; Jayson GC, Imaging Tumor Vascular Heterogeneity and Angiogenesis using Dynamic Contrast-Enhanced Magnetic Resonance Imaging. Clin. Cancer Res 2007, 13 (12), 3449–3459. [PubMed: 17575207]

52. Khouli RH; Macura KJ; Jacobs MA; Khalil TH; Kamel IR; Dwyer A; Bluemke DA, Dynamic Contrast-Enhanced MRI of the Breast: Quantitative Method for Kinetic Curve Type Assessment. Am. J. Roentgenol 2009, 193 (4), W295–W300. [PubMed: 19770298]

53. Vander Elst L; Sessoye A; Laurent S; Muller RN, Can the Theoretical Fitting of the Proton-Nuclear-Magnetic-Relaxation-Dispersion (Proton NMRD) Curves of Paramagnetic Complexes Be Improved by Independent Measurements of their Self-Diffusion Coefficients? Helv. Chim. Acta 2005, 88 (3), 574–587.

54. Kálmán FK; Woods M; Caravan P; Jurek P; Spiller M; Tircsó G; Király R; Brücher E; Sherry AD, Potentiometric and Relaxometric Properties of a Gadolinium-Based MRI Contrast Agent for Sensing Tissue pH. Inorg. Chem 2007, 46 (13), 5260–5270. [PubMed: 17539632]

55. Elhabiri M; Abada S; Sy M; Nonat A; Choquet P; Esteban-Gomez D; Cassino C; Platas-Iglesias C; Botta M; J., C. L., Importance of Outer-Sphere and Aggregation Phenomena in the Relaxation Properties of Phosphonated Gadolinium Complexes with Potential Applications as MRI Contrast Agents. Chem. Eur. J 2015, 21 (17), 6535–6546. [PubMed: 25754740]

56. Swift TJ; Connick RE, NMR-Relaxation Mechanisms of O17 in Aqueous Solutions of Paramagnetic Cations and the LIfetime of Water Molecules in the First Coordination Sphere. J. Chem. Phys 1962, 37 (2), 307–320.

57. Gale EM; Zhu J; Caravan P, Direct measurement of the Mn(II) hydration state in metal complexes and metalloproteins through 17O NMR line widths. J Am Chem Soc 2013, 135 (49), 18600–8. [PubMed: 24088013]

58. Peters JA; Geraldes CFGC, A Semi-Empirical Method for the Estimation of the Hydration Number of Mn(II)-Complexes. Inorganics 2018, 6, 116.

59. Esteban-Gomez D; Cassino C; Botta M; Platas-Iglesias C, 17O and 1H relaxometric and DFT study of hyperfine coupling constants in [Mn(H2O)6]2+. RSC Advances 2014, 4 (14), 7094–7103.

60. Caravan P; Farrar CT; Frullano L; Uppal R, Influence of molecular parameters and increasing magnetic field strength on relaxivity of gadolinium- and manganese-based T1-contrast agents. Contrast Media. Mol. Imag 2009, (4), 89–100.

61. Helm L, Optimization of gadolinium-based MRI contrast agents for high magnetic-field applications. Future Med. Chem 2010, 2 (3), 385. [PubMed: 21426173]

62. Rummeny EJ; Torres CG; Kurdziel JC; Nilsen G; OpdeBeeck B; Lundby B, MnDPDP for MR imaging of the liver - Results of an independent image evaluation of the European phase III studies. Acta Radiol 1997, 38 (4), 638–642. [PubMed: 9245957]

63. Toft KG; Hustvedt SO; Grant D; Martinsen I; Gordon PB; Friisk GA; Korsmo ÅJ; Skotland T, Metabolism and pharmacokinetics of MnDPDP in man. Acta Radiol 1997, 38 (5), 677–689. [PubMed: 9245963]

64. Gallez B; Bacic G; Swartz HM, Evidence for the dissociation of the hepatobiliary MRI contrast agent Mn-DPDP. Magn. Reson. Med 1996, 35 (1), 14–19. [PubMed: 8771018]

65. Vogl TJ; Hamm B; Schnell B; McMahon C; Branding G; LIssner J; Wolf K-J, Mn-DPDP enhancement patterns of hepatocellular lesions on MR images. J. Magn. Res. Imag 1993, 3 (1), 51–58.

66. Hu TC-C; Pautler RG; MacGowan GA; Koretsky AP, Manganese-enhanced MRI of mouse heart during changes in inotropy. Magn. Reson. Med 2001, 46 (5), 884–890. [PubMed: 11675639]

67. Leoni L; Dhyani AH; La Riviere P; Vogt S; Lai B; Roman BB, β-Cell subcellular localization of glucose-stimulated Mn uptake by X-ray fluorescence microscopy: implications for pancreatic MRI. Contrast Media & Molecular Imaging 2011, 6 (6), 474–481. [PubMed: 22144025]

68. Storey P; Danias PG; Post M; Li W; Seoane PR; Harnish PP; Edelman RR; Prasad PV, Preliminary Evaluation of EVP 1001–1: A New Cardiac-Specific Magnetic Resonance Contrast Agent with Kinetics Suitable for Steady-State Imaging of the Ischemic Heart. Invest. Radiol 2003, 38 (10), 642–652. [PubMed: 14501492]

69. Wolf GL; Baum L, ardiovascular toxicity and tissue proton T1 response to manganese injection in the dog and rabbit. AJR Am J Roentgenol 1983, 141 (1), 193–197. [PubMed: 6305179]

70. Yanaga T; Holland WC, Effect of manganese on transmembrane potential and contractility of atrial muscle. Am. J. Physiol 1969, 217 (5), 1280–1285. [PubMed: 5346291]

71. Eriksson P-O; Aaltonen E; Petoral RM Jr.; Lauritzson P; Miyazaki H; Pietras K; Mansson S; Hansson L; Leander P; Axelsson O, Novel Nano-Sized MR Contrast Agent Mediates Strong Tumor Contrast Enhancement in an Oncogene-Driven Breast Cancer Model. PLOS one 2014, 9 (10), e107762. [PubMed: 25296030]

72. Gianolio E; Bäckström S; Petoral RM Jr.; Olsson A; Aime S; Axelsson O, Characterization of a Manganese-Containing Nanoparticle as an MRI Contrast Agent. European Journal of Inorganic Chemistry 2019, 2019 (13), 1759–1766.

73. Pujales-Paradela R; Carniato F; Esteban-Gomez D; Botta M; Platas-Iglesias C, Controlling water exchange rates in potential Mn2+-based MRI agents derived from NO2A2−. Dalton Trans 2019, 48 (12), 3962–3972. [PubMed: 30834411]

74. Maigut J; Meier R; Zahl A; van Eldik R, Effect of chelate dynamics on water exchange reactions of paramagnetic aminopolycarboxylate complexes. Inorg. Chem 2008, 47 (13), 5702–5719. [PubMed: 18510310]

75. Maigut J; Meier R; Zahl A; van Eldik R, Triggering Water Exchange Mechanisms via Chelate Architecture. Shielding of Transition Metal Centers by Aminopolycarboxylate Spectator Ligands. J. Am. Chem. Soc 2008, 130, 14556–14569. [PubMed: 18839954]

76. Drahoš B; Lukeš I; Tóth E, Mn(II) complexes as potential contrast agents for MRI. Eur. J. Inorg. Chem 2012, 2012 (12), 1975–1986.

77. Forgacs A; Tei L; Baranyai Z; Esteban-Gomez D; Platas-Iglesias C; Botta M, Optimising the relaxivities of Mn2+ complexes by targeting human serum albumin (HSA). Dalton Trans 2017, 46 (26), 8494–8504. [PubMed: 28632276]

78. Botar R; Molnar E; Trencsenyi G; Kiss J; Kalman F; Tircsó G, Stable and inert Mn(II)-based and pH responsive contrast agents. J Am Chem Soc 2020, ASAP, 10.1021/jacs.9b09407.

79. Gale EM; Atanasova I; Blasi F; Ay I; Caravan P, A Manganese Alternative to Gadolinium for MRI Contrast. J. Am. Chem. Soc 2015, 137 (49), 15548–15557. [PubMed: 26588204]

80. Laurent S; Vander Elst L; Henoumon C; Muller RN, How to Measure the transmetallation of a gadolinium complex. Contrast Media. Mol. Imag 2010, 5, 305–308.

81. Laurent S; Elst LV; Copoix F; Muller RN, Stability of MRI paramagnetic contrast media: a proton relaxometric protocol for transmetallation assessment. Invest Radiol 2001, 36 (2), 115–22. [PubMed: 11224760]

82. Kálmán FK; Tircsó G, Kinetic inertness of the Mn complexes formed with AAZTA and some open-chain EDTA derivatives. Inorg. Chem 2012, 51 (19), 10065–10067. [PubMed: 22974437]

83. Drahoš B; Kotek J; Císaová I; Hermann P; Helm L; Lukeš I; Tóth E, Mn$^{2+}$ complexes with 12-member pyridine based macrocycles bearing carboxylate or phosphonate pendant arm: crystallographic, thermodynamic, kinetic, redox and $^1$H/ $^{17}$O relaxation studies. Inorg. Chem 2011, 50 (24), 12785–12801. [PubMed: 22092039]

84. Drahoš B; Kotek J; Hermann P; Lukeš I; Tóth E, Mn$^{2+}$ complexes with pyridine containing 15-membered macrocycles: thermodynamic, kinetic, crystallographic and $^1$H/ $^{17}$O relaxation studies. Inorg. Chem 2010, 49 (7), 3224–3238. [PubMed: 20180546]

85. Sarka L; Burai L; Brucher E, The Rates of the Exchange Reactions between [Gd(DTPA)]2ÿ and the Endogenous Ions Cu2‡ and Zn2‡: A Kinetic Model for the Prediction of the In Vivo Stability of [Gd(DTPA)]2ÿ, Used as a Contrast Agent in Magnetic Resonance Imaging. Chem. Eur. J 2000, 6 (4), 719–724. [PubMed: 10807182]

86. Wang J; Wang H; Ramsay IA; Erstad DJ; Fuchs BC; Tanabe KK; Caravan P; Gale EM, Manganese-Based Contrast Agents for Magnetic Resonance Imaging of Liver Tumors: Structure-Activity Relationships and Lead Candidate Evaluation. J. Med. Chem 2018, 61 (19), 8811–8824. [PubMed: 30204438]

87. Rohrer M; Bauer H; Mintorovitch J; Requardt M; Weinmann H-J, Comparison of magnetic properties of MRI contrast media solutions at different magnetic field strengths. Invest. Radiol 2005, 40 (11), 715–724. [PubMed: 16230904]

88. Gale EM; Wey HY; Ramsay I; Yen YF; Sosnovik D; Caravan P, A Manganese-Based Alternative to Gadolinium: Contrast Enhanced MR Angiography, Pharmacokinetics, and Metabolism. Radiology 2018, 286 (3), 865–872. [PubMed: 29117483]

89. Erstad DJ; Ramsay IA; Jordan VC; Sojoodi M; Fuchs BC; Tanabe KK; Caravan P; Gale EM, Tumor Contrast Enhancement and Whole-Body Elimination of the Manganese-Based Magnetic Resonance Imaging Contrast Agent Mn-PyC3A. Invest. Radiol 2019, 54 (11), 697–703. [PubMed: 31356382]

90. Islam MK; Kim S; Kim H-K; Kim Y-H; Lee Y-L; Choi G; Baek AR; Sung BK; Kim M; Cho AE; Kang H; Lee G-H; Choi SH; Lee T; Park J-A; Chang Y, Synthesis and Evaluation of Manganese(II)-Based Ethylenediaminetetraacetic Acid–Ethoxybenzyl Conjugate as a Highly Stable Hepatobiliary Magnetic Resonance Imaging Contrast Agent. Bioconjugate Chem 2018, 29 (11), 3614–3625.

91. Islam MK; Kim S; Kim HK; Park S; Lee GH; Kang HJ; Jung JC; Park JS; Kim TJ; Chan Y, Manganese Complex of Ethylenediaminetetraacetic Acid (EDTA)-Benzothiazole Aniline (BTA) Conjugate as a Potential Liver-Targeting MRI Contrast Agent. Journal of Medicinal Chemistry 2017, 60 (7), 2993–3001. [PubMed: 28301142]

92. Koenig SH; Brown RD III; Spiller M, The Anamolous Relaxivity of Mn3+(TPPS4). Magn. Reson. Med 1987, 4, 252–260. [PubMed: 3574059]

93. Ogan M; Revel D; Brasch R, Metalloporphyrin Contrast Enhancement of Tumors in Magnetic Resonance Imaging A Study of Human Carcinoma, Lymphoma, and Fibrosarcoma in Mice. Invest Radiol 1987, 22 (10), 822–828. [PubMed: 3429177]

94. Furmanski P; Longley C, Metalloporphyrin Enhancement of Magnetic Resonance Imaging of Human Tumor Xenografts in Nude Mice. Cancer Research 1988, 48 (16), 4604–4610. [PubMed: 3396012]

95. Fiel RJ; Musser DA; Mark EH; Mazurchuk R; Alletto JJ, A comparative study of manganese meso-sulfonatophenyl porphyrins: contrast-enhancing agents for tumors. Magn Reson Imaging 1990, 8 (3), 255–9. [PubMed: 2366638]

96. Schmiedl UP; Nelson JA; Robinson DH; Michalson A; Starr F; Frenzel T; Ebert W; Schumanngiampieri G, PHARMACEUTICAL PROPERTIES, BIODISTRIBUTION, AND IMAGING CHARACTERISTICS OF MANGANESE-MESOPORPHYRIN - A POTENTIAL HEPATOBILIARY CONTRAST AGENT FOR MAGNETIC-RESONANCE-IMAGING. Investigative Radiology 1993, 28 (10), 925–932. [PubMed: 8262747]

97. Schmiedl UP; Nelson JA; Starr FL; Schmidt R, HEPATIC CONTRAST-ENHANCING PROPERTIES OF MANGANESE-MESOPORPHYRIN AND MANGANESE-TPPS4 - A COMPARATIVE MAGNETIC-RESONANCE-IMAGING STUDY IN RATS. Investigative Radiology 1992, 27 (7), 536–542. [PubMed: 1644554]

98. Cheng W; Haedicke IE; Nofiele J; Martinez F; Beera K; Scholl TJ; Cheng H-LM; Zhang X. a., Complementary Strategies for Developing Gd-Free High-Field T1 MRI Contrast Agents Based on Mn(III) Porphyrins. J. Med. Chem 2014, 57, 516–520. [PubMed: 24328058]

99. Cheng W; Ganesh T; Martinez F; Lam J; Yoon H; Macgregor RB; Scholl TJ; Cheng H-LM; Zhang X. a., Binding of a dimeric manganese porphyrin to serum albumin: towards a gadolinium-free blood-pool T 1 MRI contrast agent. JBIC Journal of Biological Inorganic Chemistry 2014, 19 (2), 229–235. [PubMed: 24407461]

100. Cheng HLM; Haedicke IE; Cheng WR; Nofiele JT; Zhang XA, Gadolinium-Free T-1 Contrast Agents for MRI: Tunable Pharmacokinetics of a New Class of Manganese Porphyrins. Journal of Magnetic Resonance Imaging 2014, 40 (6), 1474–1480. [PubMed: 24214904]

101. Nofiele JT; Haedicke IE; Zhu YLK; Zhang X.-a.; Cheng H-LM, Gadolinium-Free Extracellular MR Contrast Agent for Tumor Imaging. J. Magn. Res. Imag 2015, 41 (2), 397–402.

102. Lyon RC; Faustino PJ; Cohen JS; Katz A; Mornex F; Colcher D; Baglin C; Koenig SH, Tissue Distribution and Stability of Metalloporhyrin MRI Contrast Agents. Magn. Reson. Med 1987, 4 (1), 24–33. [PubMed: 3821476]

103. Barandov A; Bartelle BB; Williamson CG; Loucks ES; Lippard SJ; Jasanoff A, Sensing intracellular calcium ions using a manganese-based MRI contrast agent. Nature. Commun 2019, 10 (1).

104. Barandov A; Bartelle BB; Gonzalez BA; White WL; Lippard SJ; Jasanoff A, Membrane-Permeable Mn(III) Complexes for Molecular Magnetic Resonance Imaging of Intracellular Targets. J. Am. Chem. Soc 2016, 138 (17), 5483–5486. [PubMed: 27088782]

105. Fraga CG, Relevance, essentiality and toxicity of trace elements in human health. Molecular Aspects of Medicine 2005, 26 (4), 235–244. [PubMed: 16125765]

106. Bloch J; Navon G, A nuclear magnetic resonance relaxation study of iron(III) EDTA in aqueous solution. J. Inorg. Nucl. Chem 1980, 42 (5), 693–699.

107. Jenkins BG; Armstrong E; Lauffer RB, SITE-SPECIFIC WATER PROTON RELAXATION ENHANCEMENT OF IRON(III) CHELATES NONCOVALENTLY BOUND TO HUMAN SERUM-ALBUMIN. Magn.Reson.Med 1991, 17 (1), 164–178. [PubMed: 1648652]

108. Mizuno M; Funahashi S; Nakasuka N; Tanaka M, Water Exchange of the (o-Phenylene-N,N,N'N'-tetraaceto)ferrate(III) Complex in Aqueous Solution As Studied by Variable-Temperature, -Pressure, and -Frequency Oxygen-17 NMR Techniques. Inorg. Chem 1991, 30 (7), 1550–1553.

109. Brausam A; Maigut J; Meier R; Szilagyi PA; Buschmann H-J; Massa W; Homannay Z; van Eldik R, Detailed Spectroscopic, Thermodynamic, and Kinetic Studies on the Protolytic Equilibria of

FeIIIcydta and the Activation of Hydrogen Peroxide. Inorg. Chem 2009, 48 (16), 7864–7884. [PubMed: 19618946]

110. Wang H; Clavijo Jordan V; Ramsay IA; Sojoodi M; Fuchs BC; Tanabe KK; Caravan P; Gale EM, Molecular Magnetic Resonance Imaging Using a Redox-Active Iron Complex. J. Am. Chem. Soc 2019, 141 (14), 5916–5925. [PubMed: 30874437]

111. Snyder EM; Asik D; Abozeid S; Burgio A; Bateman G; Turowski SG; Spernyak JA; Morrow JR, A Class of Fe III Macrocyclic Complexes With Alcohol Donor Groups as Effective T1 MRI Contrast Agents. Angew. Chem. Int. Ed 2020, 59 (6), 2414–2419.

112. Tsitovich PB; Gendron F; Nazarenko AY; Livesay BN; Lopez AP; Shores MP; Autschbach J; Morrow JR, Low-Spin Fe(III) Macrocyclic Complexes of Imidazole-Appended 1,4,7-Triazacyclononane as Paramagnetic Probes. Inorg. Chem 2018, 57 (14), 8364–8374. [PubMed: 29939736]

113. Fornasiero D; Bellen JC; Baker RJ; Chatterton BE, Paramagnetic complexes of manganese (II), iron (III), and gadolinium (III) as contrast agents for magnetic resonance imaging. The influence of stability constants on the biodistribution of radioactive aminopolycarboxylate complexes. Investigative radiology 1987, 22 (4), 322–327. [PubMed: 3583652]

114. Kálmán FK; Tircsó G, Kinetic inertness of the $Mn^{2+}$ complexes formed with AAZTA and some open-chain EDTA derivatives. Inorganic Chemistry 2012, 51 (19), 10065–10067. [PubMed: 22974437]

115. Lauffer RB, Paramagnetic metal complexes as water proton relaxation agents for NMR imaging: theory and design. Chem. Rev 1987, 87, 901–927.

116. Lauffer RB; Greif WL; Stark DD; Vincent AC; Saini S; Wedeen VJ; Brady TJ, Iron-EHPG as an hepatobilliary MR contrast agent: initial imaging and biodistribution studies. J. Comput. Assist. Tomogr 1985, 9 (3), 431–438. [PubMed: 3989032]

117. Boehm-Sturm P; Haeckel A; Hauptmann R; Mueller S; Kuhl CK; Schellenberger EA, Low-Molecular-Weight Iron Chelates May Be an Alternative to Gadolinium-based Contrast Agents for T1-weighted Contrast-enhanced MR Imaging. Radiology 2018, 286 (2), 537–546. [PubMed: 28880786]

118. Wu B; Warnock G; Zaiss M; Lin C; Chen M; Zhou Z; Mu L; Nanz D; Tuura R; Delso G, An overview of CEST MRI for non-MR physicists. EJNMMI Physics 2016, 3, 19. [PubMed: 27562024]

119. Vinogradov E; Sherry AD; Lenkinski RE, CEST: From basic principles to applications, challenges and opportunities. Journal of Magnetic Resonance 2013, 229, 155–172. [PubMed: 23273841]

120. Zijl P. v.; Yadav N, Chemical exchange saturation transfer (CEST): what is in a name and what isn't? Magn.Reson.Med 2011, 65, 927–948. [PubMed: 21337419]

121. Zhang SR; Merritt M; Woessner DE; Lenkinski RE; Sherry AD, PARACEST agents: Modulating MRI contrast via water proton exchange. Accounts Chem. Res 2003, 36 (10), 783–790.

122. Anemone A; Consolino L; Longo DL, MRI-CEST assessment of tumour perfusion using X-ray iodinated agents: comparison with a conventional Gd-based agent. European Radiology 2017, 27 (5), 2170–2179. [PubMed: 27572810]

123. Aime S; Calabi L; Biondi L; De Miranda M; Ghelli S; Paleari L; Rebaudengo C; Terreno E, Iopamidol: Exploring the potential use of a well-established X-ray contrast agent for MRI. Magn.Reson.Med 2005, 53 (4), 830–834. [PubMed: 15799043]

124. Henkelman RM; Stanisz GJ; Graham SJ, Magnetization transfer in MRI: a review. NMR Biomed 2001, 14 (2), 57–64. [PubMed: 11320533]

125. Woods M; Woessner DE; Sherry AD, Paramagnetic lanthanide complexes as PARACEST agents for medical imaging. Chemical Society reviews 2006, 35, 500–11. [PubMed: 16729144]

126. Le Fur M; Rotile NJ; Correcher C; Clavijo Jordan V; Ross AW; Catana C; Caravan P, Yttrium-86 Is a Positron Emitting Surrogate of Gadolinium for Noninvasive Quantification of Whole-Body Distribution of Gadolinium-Based Contrast Agents. Angew. Chem. Int. Ed 2020, 59 (4), 1474–1478.

127. Burns PJ; Cox JM; Morrow JR, Imidazole-appended macrocyclic complexes of Fe(II), Co(II), and Ni(II) as paraCEST agents. Inorganic Chemistry 2017, 56 (8), 4545–4554.

128. Dorazio SJ; Morrow JR, Iron(II) complexes containing octadentate tetraazamacrocycles as paraCEST magnetic resonance imaging contrast agents. Inorganic Chemistry 2012, 51 (14), 7448–7450. [PubMed: 22757664]

129. Dorazio SJ; Tsitovich PB; Siters KE; Spernyak JA; Morrow JR, Iron(II) PARACEST MRI Contrast Agents. Journal of the American Chemical Society 2011, 133 (36), 14154–14156. [PubMed: 21838276]

130. Tsitovich PB; Morrow JR, Macrocyclic ligands for Fe(II) paraCEST and chemical shift MRI contrast agents. Inorganica Chimica Acta 2012, 393, 3–11.

131. Tsitovich PB; Cox JM; Spernyak JA; Morrow JR, Gear Up for a pH Shift: A Responsive Iron(II) 2-Amino-6-picolyl-Appended Macrocyclic paraCEST Agent That Protonates at a Pendent Group. Inorganic Chemistry 2016, 55 (22), 12001–12010. [PubMed: 27934305]

132. Olatunde AO; Bond CJ; Dorazio SJ; Cox JM; Benedict JB; Daddario MD; Spernyak JA; Morrow JR, Six, Seven or Eight Coordinate Fe-II, Co-II or Ni-II Complexes of Amide-Appended Tetraazamacrocycles for ParaCEST Thermometry. Chemistry-a European Journal 2015, 21 (50), 18290–18300.

133. Olatunde AO; Cox JM; Daddario MD; Spernyak JA; Benedict JB; Morrow JR, Seven-coordinate Co$^{II}$, Fe$^{II}$ and six-coordinate Ni$^{II}$ amide-appended macrocyclic complexes as paracest agents in biological media. Inorganic Chemistry 2014, 53 (16), 8311–8321. [PubMed: 24820102]

134. Abozeid SM; Snyder EM; Lopez AP; Steuerwald CM; Sylvester E; Ibrahim KM; Zaky RR; Abou-El-Nadar HM; Morrow JR, Nickel(II) complexes as paramagnetic shift and paraCEST agents. European Journal of Inorganic Chemistry 2018, 2018 (18), 1902–1908.

135. Dorazio SJ; Olatunde AO; Spernyak JA; Morrow JR, CoCEST: cobalt(II) amide-appended paraCEST MRI contrast agents. Chem. Commun 2013, 49 (85), 10025–10027.

136. Abozeid SM; Snyder EM; Tittiris TY; Steuerwald CM; Nazarenko AY; Morrow JR, Inner-sphere and outer-sphere water interactions in Co(II) paraCEST agents. Inorganic Chemistry 2018, 57 (4), 2085–2095. [PubMed: 29412653]

137. Thorarinsdottir AE; Tatro SM; Harris TD, Electronic Effects of Ligand Substitution in a Family of CoII2 PARACEST pH Probes. Inorg. Chem 2018, 57 (17), 11252–11263. [PubMed: 30136567]

138. Du K; Harris TD, A Cu-2(II) Paramagnetic Chemical Exchange Saturation Transfer Contrast Agent Enabled by Magnetic Exchange Coupling. Journal of the American Chemical Society 2016, 138 (25), 7804–7807. [PubMed: 27276533]

139. Murthy NN; Karlin KK; Bertini I; Luchinat C, NMR and Electronic Relaxation in Paramagnetic Dicopper(II) Compounds. J. Am. Chem. Soc 1997, 119 (9), 2156–2162.

140. Paech D; Schuenke P; Koehler C; Windschuh J; Mundiyanapurath S; Bickelhaupt S; Bonekamp D; Baumer P; Bachert P; Ladd ME; Bendszus M; Wick W; Unterberg A; Schlemmer HP; Zaiss M; Radbruch A, T1 rho- weighted Dynamic Glucose-enhanced MR Imaging in the Human Brain. Radiology 2017, 285 (3), 914–922. [PubMed: 28628422]

141. Anemone A; Consolino L; Arena F; Capozza M; Longo DL, Imaging tumor acidosis: a survey of the available techniques for mapping in vivo tumor pH. Cancer and Metastasis Reviews 2019, 38 (1–2), 25–49. [PubMed: 30762162]

142. Muller-Lutz A; Khalil N; Schmitt B; Jellus V; Pentang G; Oeltzschner G; Antoch G; Lanzman RS; Wittsack H-J, Pilot study of Iopamidol-based quantitative pH imaging on a clinical 3T MR scanner. Magn. Reson. Mater. Phys 2014, 27 (6), 477–485.

143. Jones KM; Randtke EA; Yoshimaru ES; Howison CM; Chalasani P; Klein RR; Chambers SK; Kuo PH; Pagel MD, Clinical Translation of Tumor Acidosis Measurements with AcidoCEST MRI. Mol. Imaging Biol 2017, 19 (4), 617–625. [PubMed: 27896628]

144. Delli Castelli D; Ferrauto G; Cutrin JC; Terreno E; Aime S, In vivo maps of extracellular pH in murine melanoma by CEST–MRI. Magn.Reson.Med 2014, 71 (1), 326–332. [PubMed: 23529973]

145. Ferrauto G; Di Gregorio E; Auboiroux V; Petit M; Berger F; Aime S; Lahrech CEST-MRI for glioma pH quantification in mouse model: Validation by immunohistochemistry. NMR Biomed 2018, 31 (11), e4005. [PubMed: 30256478]

146. Coman D; Huang Y; Rao JU; De Feyter HM; Rothman DL; Juchem C; Hyder F, Imaging the intratumoral-peritumoral extracellular pH gradient of gliomas. NMR Biomed 2016, 29 (3), 309–319. [PubMed: 26752688]

147. Yoo B; Sheth VR; Howison CM; Douglas MJK; Pineda CT; Maine EA; Baker AF; Pagel MD, Detection of in vivo enzyme activity with CatalyCEST MRI. Magn.Reson.Med 2014, 71 (3), 1221–1230. [PubMed: 23640714]

148. Yoo B; Raam MS; Rosenblum RM; Pagel MD, Enzyme-responsive PARACEST MRI contrast agents: a new biomedical imaging approach for studies of the proteasome. Contrast Media & Molecular Imaging 2007, 2 (4), 189–198. [PubMed: 17712869]

149. Yoo B; Pagel MD, A PARACEST MRI Contrast Agent To Detect Enzyme Activity. Journal of the American Chemical Society 2006, 128 (43), 14032–14033. [PubMed: 17061878]

150. Suchy M; Ta R; Li AX; Wojciechowski F; Pasternak SH; Bartha R; Hudson RHE, A paramagnetic chemical exchange-based MRI probe metabolized by cathepsin D: design, synthesis and cellular uptake studies. Organic & Biomolecular Chemistry 2010, 8 (11), 2560–2566. [PubMed: 20485791]

151. Chauvin T; Durand P; Bernier M; Meudal H; Doan B-T; Noury F; Badet B; Beloeil J-C; Tóth É, Detection of Enzymatic Activity by PARACEST MRI: A General Approach to Target a Large Variety of Enzymes. Angewandte Chemie International Edition 2008, 47 (23), 4370–4372. [PubMed: 18454438]

152. Daryaei I; Jones KM; Pagel MD, Detection of DT-diaphorase Enzyme with a ParaCEST MRI Contrast Agent. Chemistry – A European Journal 2017, 23 (27), 6514–6517.

153. Li Y; Sheth VR; Liu G; Pagel MD, A self-calibrating PARACEST MRI contrast agent that detects esterase enzyme activity. Contrast Media & Molecular Imaging 2011, 6 (4), 219–228. [PubMed: 21861282]

154. Coman D; de Graaf RA; Rothman DL; Hyder F, In vivo three-dimensional molecular imaging with Biosensor Imaging of Redundant Deviation in Shifts (BIRDS) at high spatiotemporal resolution. NMR in Biomedicine 2013, 26 (11), 1589–1595. [PubMed: 23881869]

155. Schmidt R; Nippe N; Strobel K; Masthoff M; Reifschneider O; Castelli DD; Höltke C; Aime S; Karst U; Sunderkötter C; Bremer C; Faber C, Highly shifted proton MR imaging: Cell tracking by using direct detection of paramagnetic compounds. Radiology 2014, 272 (3), 785–795. [PubMed: 24852443]

156. Srivastava K; Weitz EA; Peterson KL; Marjanska M; Pierre VC, Fe- and Ln-DOTAm-F12 Are Effective Paramagnetic Fluorine Contrast\ Agents for MRI in Water and Blood. Inorg. Chem 2017, 56 (3), 1546–1557. [PubMed: 28094930]

157. Tsitovich PB; Tittiris TY; Cox JM; Benedict JB; Morrow JR, Fe(ii) and Co(ii) N-methylated CYCLEN complexes as paraSHIFT agents with large temperature dependent shifts. Dalton Transactions 2018, 47 (3), 916–924. [PubMed: 29260180]

158. Tsitovich PB; Cox JM; Benedict JB; Morrow JR, Six-coordinate Iron(II) and Cobalt(II) paraSHIFT Agents for Measuring Temperature by Magnetic Resonance Spectroscopy. Inorganic Chemistry 2016, 55 (2), 700–716. [PubMed: 26716610]

159. O'Neill ES; Kolanowski JL; Bonnitcha PD; New EJ, A cobalt(II) complex with unique paraSHIFT responses to anions. Chem. Commun 2017, 53 (25), 3571–3574.

160. Pujales-Paradela R; Saví T; Brandariz I; Pérez-Lourido P; Angelovski G; Esteban-Gómez D; Platas-Iglesias C, Reinforced Ni(II)-cyclam derivatives as dual 1H/19F MRI probes. Chem. Commun 2019, 55 (28), 4115–4118.

161. Srivastava K; Ferrauto G; Young VG Jr.; Aime S; Pierre VC, Eight-Coordinate, Stable Fe(II) Complex as a Dual 19F and CEST Contrast Agent for Ratiometric pH Imaging. Inorg. Chem 2017, 56 (20), 12206–12213. [PubMed: 28981278]

162. Bleany B, Nuclear Magnetic Resonance Shifts in Solution Due to Lanthanide Ions. J. Magn. Res 1972, 8 (1), 91–100.

163. Xie D; Yu M; Kadakia RT; Que EL, 19F Magnetic Resonance Activity-Based Sensing Using Paramagnetic Metals. Acc. Chem. Res 2020, 53 (1), 2–10. [PubMed: 31809009]

164. Khurana A; Chapelin F; Xu HY; Acevedo JR; Molinolo A; Nguyen Q; Ahrens ET, Visualization of macrophage recruitment in head and neck carcinoma model using fluorine-19 magnetic resonance imaging. Magn.Reson.Med 2018, 79 (4), 1972–1980. [PubMed: 28748562]

165. Zhong J; Narsinh K; Morel PA; Xu HY; Ahrens ET, In Vivo Quantification of Inflammation in Experimental Autoimmune Encephalomyelitis Rats Using Fluorine-19 Magnetic Resonance Imaging Reveals Immune Cell Recruitment outside the Nervous System. Plos One 2015, 10 (10), 13.

166. Ahrens ET; Helfer BM; O'Hanlon CF; Schirda C, Clinical Cell Therapy Imaging Using a Perfluorocarbon Tracer and Fluorine-19 MRI. Magn.Reson.Med 2014, 72 (6), 1696–+. [PubMed: 25241945]

167. Ruiz-Cabello J; Barnett BP; Bottomley PA; Bulte JWM, Fluorine (19F) MRS and MRI in biomedicine. NMR in Biomedicine 2011, 24 (2), 114–129. [PubMed: 20842758]

168. Barnett BP; Ruiz-Cabello J; Hota P; Ouwerkerk R; Shamblott MJ; Lauzon C; Walczak P; Gilson WD; Chacko VP; Kraitchman DL; Arepally A; Bulte JWM, Use of perfluorocarbon nanoparticles for non-invasive multimodal cell tracking of human pancreatic islets. Contrast Media & Molecular Imaging 2011, 6 (4), 251–259. [PubMed: 21861285]

169. de Vries IJM; Lesterhuis WJ; Barentsz JO; Verdijk P; van Krieken JH; Boerman OC; Oyen WJG; Bonenkamp JJ; Boezeman JB; Adema GJ; Bulte JWM; Scheenen TWJ; Punt CJA; Heerschap A; Figdor CG, Magnetic resonance tracking of dendritic cells in melanoma patients for monitoring of cellular therapy. Nat. Biotechnol 2005, 23 (11), 1407–1413. [PubMed: 16258544]

170. Jahromi AH; Wang C; Adams SR; Zhu W; Narsinh K; Xu H; Gray DL; Tsien RY; Ahrens ET, Fluorous-Soluble Metal Chelate for Sensitive Fluorine-19 Magnetic Resonance Imaging Nanoemulsion Probes. ACS Nano 2018, 13 (1), 143–151. [PubMed: 30525446]

171. Harvey P; Blamire AM; Wilson JI; Finney K-LNA; Funk AM; Senanayake PK; Parker D, Moving the goal posts: enhancing the sensitivity of PARASHIFT proton magnetic resonance imaging and spectroscopy. Chem. Sci 2013, 4 (11), 4251–4258.

172. Hekmatyar SK; Hopewell P; Pakin SK; Babsky A; Bansal N, Noninvasive MR thermometry using paramagnetic lanthanide complexes of 1,4,7,10-tetraazacyclodoecane-α,α′,α″,α‴-tetramethyl-1,4,7,10-tetraacetic acid (DOTMA4–). Magn.Reson.Med 2005, 53 (2), 294–303. [PubMed: 15678553]

173. Overoye-Chan K; Koerner S; Looby RJ; Kolodziej AF; Zech SG; Deng Q; Chasse JM; McMurry TJ; Caravan P, EP-2104R: a fibrin-specific gadolinium-Based MRI contrast agent for detection of thrombus. J Am Chem Soc 2008, 130 (18), 6025–39. [PubMed: 18393503]

174. Caravan P; Das B; Dumas S; Epstein FH; Helm PA; Jacques V; Koerner S; Kolodziej A; Shen L; Sun WC; Zhang Z, Collagen-targeted MRI contrast agent for molecular imaging of fibrosis. Angew Chem Int Ed Engl 2007, 46 (43), 8171–3. [PubMed: 17893943]

175. Uppal R; Medarova Z; Farrar CT; Dai G; Moore A; Caravan P, Molecular imaging of fibrin in a breast cancer xenograft mouse model. Invest Radiol 2012, 47 (10), 553–8. [PubMed: 22960948]

176. Uppal R; Catana C; Ay I; Benner T; Sorensen AG; Caravan P, Bimodal thrombus imaging: simultaneous PET/MR imaging with a fibrin-targeted dual PET/MR probe--feasibility study in rat model. Radiology 2011, 258 (3), 812–20. [PubMed: 21177389]

177. Uppal R; Ay I; Dai G; Kim YR; Sorensen AG; Caravan P, Molecular MRI of intracranial thrombus in a rat ischemic stroke model. Stroke 2010, 41 (6), 1271–7. [PubMed: 20395615]

178. Farrar CT; Gale EM; Kennan R; Ramsay I; Masia R; Arora G; Looby K; Wei L; Kalpathy-Cramer J; Bunzel MM; Zhang C; Zhu Y; Akiyama TE; Klimas M; Pinto S; Diyabalanage H; Tanabe KK; Humblet V; Fuchs BC; Caravan P, CM-101: Type I Collagen-targeted MR Imaging Probe for Detection of Liver Fibrosis. Radiology 2018, doi: 10.1148/radiol.2017170595.

179. Fuchs BC; Wang H; Yang Y; Wei L; Polasek M; Schuhle DT; Lauwers GY; Parkar A; Sinskey AJ; Tanabe KK; Caravan P, Molecular MRI of collagen to diagnose and stage liver fibrosis. Journal of Hepatology 2013, 59 (5), 992–8. [PubMed: 23838178]

180. Polasek M; Fuchs BC; Uppal R; Schuhle DT; Alford JK; Loving GS; Yamada S; Wei L; Lauwers GY; Guimaraes AR; Tanabe KK; Caravan P, Molecular MR imaging of liver fibrosis: a feasibility study using rat and mouse models. J Hepatol 2012, 57 (3), 549–55. [PubMed: 22634342]

181. Botnar RM; Wiethoff AJ; Ebersberger U; Lacerda S; Blume U; Warley A; Jansen CHP; Onthank DC; Cesati RR; Rezavi R; Marber MS; Hamm B; Schaeffter T; Robinson SP; Makowsi MR, In Vivo Assessment of Aortic Aneurysm Wall Integrity Using Elastin-Specific Molecular Magnetic Resonance Imaging. Circ. Cardiovasc. Imaging 2015, 7 (4), 679–689.

182. Protti A; Lavin B; Dong X; Lorrio S; Robinson S; Onthank DC; Shah AM; Botnar RM, Assessment of Myocardial Remodeling Using an Elastin/ Tropoelastin Specific Agent with High Field Magnetic Resonance Imaging (MRI). J. Am. Heart Assoc 2015, 4 (8), e001851. [PubMed: 26272655]

183. Phinikaridou A; Andia ME; Indermuehle A; Onthank DC; Cesati RR; Smith A; Robinson SP; Saha P; Botnar RM, Vascular Remodeling and Plaque Vulnerability in a Rabbit Model of Atherosclerosis: Comparison of Delayed Enhancement MR Imaging with an Elastin-specific Contrast Agent and Unenhanced Black-Blood MR Imaging. Radiology 2014, 271 (2), 390–399. [PubMed: 24475852]

184. Wildgruber M; Bielicki I; Aichler M; Kosanke K; Feuchtinger A; Settles M; Onthank DC; Cesati RR; Robinson SP; Huber AM; Rummeny EJ; Walch AK; Botnar RM, Assessment of Myocardial Infarction and Postinfarction Scar Remodeling With an Elastin-Specific Magnetic Resonance Agent. 7 2014, 2 (321–329), 321.

185. Spuentrup E; Botnar RM; Wiethoff AJ; Ibrahim T; Kelle S; Katoh M; Ozgun M; Nagel E; Vymazal J; Graham PB; Günther RW; Maintz D, MR imaging of thrombi using EP-2104R, a fibrin-specific contrast agent: initial results in patients. Eur. Radiol 2008, 18 (9), 1995–2005. [PubMed: 18425519]

186. Mastarone DJ; Harrison VSR; Eckermann AL; Parigi G; Luchinat C; Meade TJ, A Modular System for the Synthesis of Multiplexed Magnetic Resonance Probes. Journal of the American Chemical Society 2011, 133 (14), 5329–5337. [PubMed: 21413801]

187. Zhang S; Wu K; Sherry AD, A Novel pH-Sensitive MRI Contrast Agent. Angew. Chem., Int. Ed 1999, 38 (21), 3192–3194.

188. Lowe MP; Parker D; Reany O; Aime S; Botta M; Castellano G; Gianolio E; Pagliarin R, pH-Dependent Modulation of Relaxivity and Luminescence in Macrocyclic Gadolinium and Europium Complexes Based on Reversible Intramolecular Sulfonamide Ligation. J. Am. Chem. Soc 2001, 123 (31), 7601–7609. [PubMed: 11480981]

189. Esqueda AC; López JA; Andreu-de-Riqure G; Alvarado-Monzón JC; Ratnakar SJ; Lubag AJM; Sherry AD; De León-Rodríguez LM, A New Gadolinium-Based MRI Zinc Sensor. J. Am. Chem. Soc 2009, 131, 11387–11391. [PubMed: 19630391]

190. Oukhatar F; Meme S; Meme W; Szeremeta F; Logothetis NK; Angelovski G; Toth E, MRI Sensing of Neurotransmitters with a Crown Ether Appended Gd3+ Complex. ACS Chem. Neurosci 2015, 6 (2), 219–225. [PubMed: 25496344]

191. MacRenaris KW; Ma Z; Krueger RL; Carney CE; Meade TJ, Cell-Permeable Esterase-Activated Ca(II)-Sensitive MRI Contrast Agent. Bioconjugate Chemistry 2016, 27 (2), 465–473. [PubMed: 26689452]

192. Major JL; Bolteau RM; Meade TJ, Mechanisms of Zn$^{II}$-Activated Contrast Agents. Inorg. Chem 2008, 47 (22), 10788–10795. [PubMed: 18928280]

193. Kadjane P; Platas-Iglesias C; Boehm-Sturm P; Truffault V; Hagberg GE; Hoehn M; Logothetis NK; Angelovski G, Dual-Frequency Calcium-Responsive MRI Agents. Chem. Eur. J 2014, 20 (24), 7351–7362. [PubMed: 24796323]

194. Regueiro-Figueroa M; Gunduz S; Patinec V; Logothetis NK; Esteban-Gomez D; Tripier R; Angelovski G, Gd3+-based Magnetic Resonance imaging Contrast Agent Responsive to Zn2+. Inorg. Chem 2015, 54 (21).

195. Tu C; Nagao R; Louie AY, Multimodal Magnetic-Resonance/Optical-Imaging Contrast Agent Sensitive to NADH. Angew. Chem. Int. Ed 2009, 48, 6547–6551.

196. Carrera C; Digilio G; Baroni S; Burgio D; Consol S; Fedeli F; Longo D; Mortillaro A; Aime S, Synthesis and characterization of a Gd(iii) based contrast agent responsive to thiol containing compounds. Dalton Transactions 2007, (43), 4980–4987. [PubMed: 17992283]

197. Louie AY; Hüber MM; Ahrens ET; Rothbächer U; Moats R; Jacobs RE; Fraser SE; Meade TJ, In Vivo Visualization of Gene Expression Using Magentic Resonance Imaging. Nat. Biotechnol 2000, 18, 321–325. [PubMed: 10700150]

198. Moats RA; Fraser SE; Meade TJ, A "Smart" Magnetic Resonance Imaging Agent That Reports on Specific Enzymatic Activity. Angew. Chem. Int. Ed 1997, 36 (7), 726–727.

199. Lilley LM; Kamper S; Caldwell M; Chia ZK; Ballweg D; Vistain L; Krimmel J; Mills TA; MacRenaris K; Lee P; Water EA; Meade TJ, Self-Immolative Activation of β-Galactosidase-Responsive Probes for In Vivo MR Imaging in Mouse Models. Angew. Chem. Int. Ed 2020, 59 (1), 388–394.

200. Rodríguez E; Nilges M; Weissleder R; Chen JW, Activatable Magnetic Resonance Imaging Agents for Myeloperoxidase Sensing: Mechanism of Activation, Stability, and Toxicity. J. Am. Chem. Soc 2010, 132, 168–177. [PubMed: 19968300]

201. Nejadnik H; Ye D; Lenkov OD; Donig JS; Martin JE; Castillo R; Derugin N; Sennino B; Rao J; Daldrup-Link H, Magnetic Resonance Imaging of Stem Cell Apoptosis in Arthritic Joints with a Caspase Activatable Contrast Agent. ACS Nano 2015, 9 (2), 1150–1160. [PubMed: 25597243]

202. Mizukami S; Takikawa R; Sugihara F; Hori Y; Tochio H; Wälchi M; Shirakawa M; Kikuchi K, Paramagnetic Relaxation-Based 19F MRI Probe To Detect Protease Activity. J. Am. Chem. Soc 2008, 130, 794–795. [PubMed: 18154336]

203. Garcia-Martin ML; Martinez GV; Raghunand N; Sherry AD; Zhang S; Gillies RJ, High resolution pHe imaging of rat glioma using pH-dependent relaxivity. Magn.Reson.Med 2006, 55 (2), 309–315. [PubMed: 16402385]

204. Raghunand N; Howison C; Sherry AD; Zhang S; Gillies RJ, Renal and systemic pH imaging by contrast-enhanced MRI. Magn.Reson.Med 2003, 49 (2), 249–257. [PubMed: 12541244]

205. Clavijo Jordan MV; Lo S-T; Chen S; Preihs C; Chirayil S; Zhang S; Kapur P; Li W-H; De Leon-Rodriguez LM; Lubag AJM; Rofsky NM; Sherry AD, Zinc-sensitive MRI contrast agent detects differential release of Zn(II) ions from the healthy vs. malignant mouse prostate. Proceedings of the National Academy of Sciences 2016, 113 (37), E5464–E5471.

206. Lubag AJM; De Leon-Rodriguez LM; Burgess SC; Sherry AD, Noninvasive MRI of β-cell function using a Zn2+-responsive contrast agent. Proceedings of the National Academy of Sciences 2011, 108 (45), 18400–18405.

207. Su HS; Nahrendorf M; Panizzi P; Breckwoldt MO; Rodriguez E; Iwamoto Y; Aikawa E; Weissleder R; Chen JW, Vasculitis: Molecular Imaging by Targeting the Inflammatory Enzyme Myeloperoxidase. Radiology 2012, 262 (1), 181–190. [PubMed: 22084204]

208. Kleijn A; Chen JW; Buhrman JS; Wojtkiewicz GR; Iwamoto Y; Lamfers ML; Stemmer-Rachamimov AO; Rabkin SD; Weissleder R; Martuza RL; Fulci G, Distinguishing Inflammation from Tumor and Peritumoral Edema by Myeloperoxidase Magnetic Resonance Imaging. Clin. Cancer Res 2011, 17 (13), 4484–4493. [PubMed: 21558403]

209. Nahrendorf M; Sosnovik D; Chen JW; Panizzi P; Figueiredo J-L; Aikawa E; Libby P; Swirski FK; Weissleder R, Activatable Magnetic Resonance Imaging Agent Reports Myeloperoxidase Activity in Healing Infarcts and Noninvasively Detects the Antiinflammatory Effects of Atorvastatin on Ischemia-Reperfusion Injury. Circulation 2008, 117, 1153–1169. [PubMed: 18268141]

210. Breckwoldt MO; Chen JW; Stangenberg L; Aikawa E; Rodriguez E; Qiu S; Moskowitz MA; Weissleder R, Tracking the inflammatory response in stroke in vivo by sensing the enzyme myeloperoxidase. Proc. Natl. Acad. Sci., U.S.A 2008, 105 (47), 18584–18589. [PubMed: 19011099]

211. Aime S; Botta M; Gianolio E; Terreno E, A p(O2)-Responsive MRI Contrast Agent Based on the Redox Switch of Manganese(ii/iii) ±Porphyrin Complexes. Angew. Chem. Int. Ed 2000, 39 (4), 747–750.

212. Frost AE; Freedman HH; Westerback SJ; Martell AE, Chelating Tendencies of N,N'-Ethylenebis-[2-(0-hydroxyphenyl)]-glycine. J. Am. Chem. Soc 1958, 80 (3), 530–536.

213. Gale EM; Mukherjee S; Liu C; Loving GS; Caravan P, Structure-redox-relaxivity relationships for redox responsive manganese-based magnetic resonance imaging probes. Inorg Chem 2014, 53 (19), 10748–61. [PubMed: 25226090]

214. Loving GS; Mukherjee S; Caravan P, Redox-activated manganese-based MR contrast agent. J Am Chem Soc 2013, 135 (12), 4620–3. [PubMed: 23510406]

215. Bihari S; Smith PA; Parsons S; Sadler PJ, Stereoisomers of Mn(III) compelxes of ethylenbis[(o-hydroxyphenyl)glycine]. Inorg. Chim. Acta 2001, 331, 310–317.

216. Yu M; Beyers RJ; Gorden JD; Cross JN; Goldsmith CR, A Magnetic Resonance Imaging Contrast Agent Capable of Detecting Hydrogen Peroxide. Inorganic Chemistry 2012, 51 (17), 9153–9155. [PubMed: 22889331]

217. Gale EM; Jones CM; Ramsay I; Farrar CT; Caravan P, A Janus Chelator Enables Biochemically Responsive MRI Contrast with Exceptional Dynamic Range. J Am Chem Soc 2016, 138 (49), 15861–15864. [PubMed: 27960350]

218. Gore JC; Kang YS; Schulz RJ, Measurement of radiation dose distributions by nuclear magnetic resonance (NMR) imaging. Phys. Med. Biol 1984, 29 (10), 1189–1197. [PubMed: 6494247]

219. Ding S-P; J.-C., L.; Jin, C., A mouse model of severe acute pancreatitis induced with caerulein and lipopolysaccharide. World J. Gastroenterol 2003, 9 (3), 584–589. [PubMed: 12632523]

220. Tsitovich PB; Spernyak JA; Morrow JR, A redox-activated MRI Contrast Agent that Switches between Paramagnetic and Diamagnetic States. Angew. Chem. Int. Ed 2013, 52, 13997–14000.

221. Du K; Waters EA; Harris TD, Ratiometric quantitation of redox status with a molecular Fe-2 magnetic resonance probe. Chem. Sci 2017, 8 (6), 4424–4430. [PubMed: 28979760]

222. Jeon I-R; Park JG; Haney CR; Harris TD, Spin crossover iron(II) complexes as PARACEST MRI thermometers. Chem. Sci 2014, 5 (6), 2461–2465.

223. Yu M; Xie D; Phan KP; Enriquez JS; Luci JJ; Que EL, A CoII complex for 19F MRI-based detection of reactive oxygen species. Chem. Commun 2016, 52 (96), 13885–13888.

224. Yu M; Bouley BS; Xie D; Enriquez JS; Que EL, 19F PARASHIFT Probes for Magnetic Resonance Detection of H2O2 and Peroxidase Activity. J Am Chem Soc 2018, 130 (33), 10546–10552.

225. Jose CG; Jacob RH; Gardner GE, Alternative cutting methods and dry aging reduce the shear force of hot boned beef striploin in Bos indicus cattle. Meat Sci 2020, 163, 108036. [PubMed: 31951922]

226. Dearling JLJ; Packard AB, Some thoughts on the mechanism of cellular trapping of Cu(II)-ATSM. Nucl. Med. Biol 2010, 37 (3), 237–243. [PubMed: 20346863]

227. Lapi SE; Lewis JS; Dehdashti F, Evaluation of Hypoxia with Cu-ATSM. Semin. Nucl. Med 2015, 45 (2), 177–185.

228. Xue D; King TL; Banerjee A; Kohli V; Que EL, Exploiting Copper Redox for 19F Magnetic Resonance-Based Detection of Cellular Hypoxia. J. Am. Chem. Soc 2016, 138 (9), 2937–2940. [PubMed: 26906216]

229. Xie D; Kim S; Kohli V; Banerjee A; Yu M; Enriquez JS; Luci JJ; Que EL, Hypoxia-Bioresponsive 19F MRI Probes with Improved Redox Properties and Biocompatibility. Inorg. Chem 2017, 56 (11), 6429–6437. [PubMed: 28537705]

230. Enriquez JS; Yu M; Bouley BS; Xie D; Que EL, Copper(II) complexes for cysteine detection using 19F magnetic resonance. Dalton Trans 2018, 47 (42), 15024–15030. [PubMed: 30303220]

231. Aime S; Anelli PL; Botta M; Brocchetta M; Canton S; Fedeli F; Gianolio E; Terreno E, Relaxometric evaluation of novel manganese(II) complexes for application as contrast agents in magnetic resonance imaging. J. Biol. Inorg. Chem 2002, 7 (1–2), 58–67. [PubMed: 11862541]

232. Troughton JS; Greenfield MT; Greenwood JM; Dumas S; Wiethoff AJ; Wang J; Spiller M; McMurry TJ; Caravan P, Synthesis and evaluation of a high relaxivity manganese(II)-based MRI contrast agent. Inorg Chem 2004, 43 (20), 6313–23. [PubMed: 15446878]

233. Paradela-Pujales R; Carniato F; Uzal-Varela R; Brandariz I; Iglesias E; Platas-Iglesias C; Botta M; Esteban-Gomez D, A pentadentate member of the picolinate family for Mn(II) complexation and an amphiphilic derivative. Dalton Trans 2019, 48 (2), 696–710. [PubMed: 30547165]

234. Forgacs A; Paradela-Pujales R; Regueiro-Figueroa M; Valencia L; Esteban-Gomez D; Botta M; Platas-Iglesias C, Developing the family of picolinate ligands for Mn2+ complexation. Dalton Trans 2017, 46 (5), 1546–1558. [PubMed: 28091671]

235. Regueiro-Figueroa M; Rolla GA; Esteban-Gomez D; De Blas A; Rodriguez-Blas T; Botta M; Platas-Iglesias C, High Relaxivity Mn2+-Based MRI Contrast Agents. Chem. Eur. J 2014, 20 (52), 17300–17305. [PubMed: 25382711]

236. Zhu J; Gale EM; Atanasova I; Rietz TA; Caravan P, Hexameric Mn(II) dendrimer as MRI contrast agent. Chemistry 2014, 20 (44), 14507–13. [PubMed: 25224391]

237. Forgacs A; Regueiro-Figueroa M; Barriada JL; Esteban-Gomez D; de Blas A; Rodrigues-Blas T; Botta M; Platas-Iglesias C, Mono-, Bi-, and Trinuclear Bis-Hydrated Mn2+ Complexes as Potential MRI Contrast Agents. Inorg. Chem 2015, 54 (19), 9576–9587. [PubMed: 26397808]

238. Rolla GA; Platas-Iglesias C; Botta M; Tei L; Helm L, 1H and 17O NMR relaxometric and computational study on macrocyclic Mn(II) complexes. Inorg. Chem 2013, 52 (6), 3268–3279. [PubMed: 23437979]

239. Patinec V; Rolla GA; Botta M; Tripier R; Esteban-Gomez D; Platas-Iglesias C, Hyperfine Coupling Constants on Inner-Sphere Water Molecules of a Triazacyclononane based Mn(II) Complex and Related Systems Relevant as MRI Contrast Agents. Inorg. Chem 2013, 52 (19), 11173–11184. [PubMed: 24070368]

240. Phukan B; Mukherjee C; Goswami U; Sarmah A; Mukherjee S; Sahoo SK; Moi SC, A New Bis(aquated) High Relaxivity Mn(II) Complex as an Alternative to Gd(III)-Based MRI Contrast Agent. Inorg. Chem 2018, 57 (5).

241. Bianchi A; Calabi L; Giorgi C; Losi P; Mariani P; Palano D; Paoli P; Rossi P; Valtancoli B, Thermodynamic and structural aspects of manganese(II) complexes with polyaminopolycarboxylic ligands based upon 1,4,7,10- tetraazacyclododecane (cyclen). Crystal structure of dimeric [MnL]2–2CH3OH containing the new ligand 1,4,7,10-tetraaza-cyclododecane-1,4-diacetate. J. Chem. Soc. Dalton Trans 2001, (6), 917–922.

242. Laurent S; Vander Elst L; Copoix F; Muller RN, Stability of MRI Paramagnetic Contrast Media: A Proton Relaxometric Protocol for Transmetallation Assessment. Invest. Radiol 2001, 36, 115–122. [PubMed: 11224760]

243. Pota K; Garda Z; Kalman FK; Barriada JL; Esteban-Gomez D; Platas-Iglesias C; Toth I; Brucher E; Tircsó G, Taking the next step toward inert Mn2+ complexes of open-chain ligands: the case of the rigid PhDTA ligand. New J. Chem 2018, 42, 8001–8011.

244. Longo DL; Michelotti F; Consolino L; Bardini P; Digilio G; Xiao G; Sun PZ; Aime S, In Vitro and In Vivo Assessment of Nonionic Iodinated Radiographic Molecules as Chemical Exchange Saturation Transfer Magnetic Resonance Imaging Tumor Perfusion Agents. Invest. Radiol 2016, 51 (3), 155–162. [PubMed: 26460826]

245. Delli Castelli D; Terreno E; Aime S, YbIII-HPDO3A: A Dual pH- and Temperature-Responsive CEST Agent. Angewandte Chemie International Edition 2011, 50 (8), 1798–1800. [PubMed: 21328642]

246. Aime S; Barge A; Delli Castelli D; Fedeli F; Mortillaro A; Nielsen FU; Terreno E, Paramagnetic Lanthanide(III) complexes as pH-sensitive chemical exchange saturation transfer (CEST) contrast agents for MRI applications. Magn.Reson.Med 2002, 47 (4), 639–648. [PubMed: 11948724]

247. Mani T; Opina ACL; Zhao P; Evbuomwan OM; Milburn N; Tircsó G; Kumas C; Sherry AD, The stereochemistry of amide side chains containing carboxyl groups influences water exchange rates in EuDOTA-tetraamide complexes. J. Biol. Inorg. Chem 2014, 19 (2), 161–171. [PubMed: 23979260]

248. Dorazio SJ; Olatunde AO; Tsitovich PB; Morrow JR, Comparison of divalent transition metal ion paraCEST MRI contrast agents. J. Biol. Inorg. Chem 2014, 19, 191–205. [PubMed: 24253281]

249. Olatunde AO; Dorazio SJ; Spernyak JA; Morrow JR, The NiCEST Approach: Nickel(II) ParaCEST MRI Contrast Agents. Journal of the American Chemical Society 2012, 134 (45), 18503–18505. [PubMed: 23102112]

250. Caneda-Martínez L; Valencia L; Fernández-Pérez I; Regueiro-Figueroa M; Angelovski G; Brandariz I; Esteban-Gómez D; Platas-Iglesias C, Toward inert paramagnetic Ni(II)-based chemical exchange saturation transfer MRI agents. Dalton Transactions 2017, 46 (43), 15095–15106. [PubMed: 29067395]

251. Senanayake PK; Rogers NJ; Finney K-LNA; Harvey P; Funk AM; Wilson JI; O'Hogain D; Maxwell R; Parker D; Blamire AM, A new paramagnetically shifted imaging probe for MRI. Magn.Reson.Med 2017, 77 (3), 1307–1317. [PubMed: 26922918]

252. Martins AF; Clavijo Jordan V; Bochner F; Chirayil S; Paranawithana N; Zhang S; Lo S-T; Wen X; Zhao P; Neeman M; Sherry AD, Imaging Insulin Secretion from Mouse Pancreas by MRI Is Improved by Use of a Zinc Responsive MRI Sensor with Lower Affinity for Zn2+ Ions. J. Am. Chem. Soc 2018, 140 (50), 17456–17464. [PubMed: 30484648]

**A**

**B**

**C**

**D**
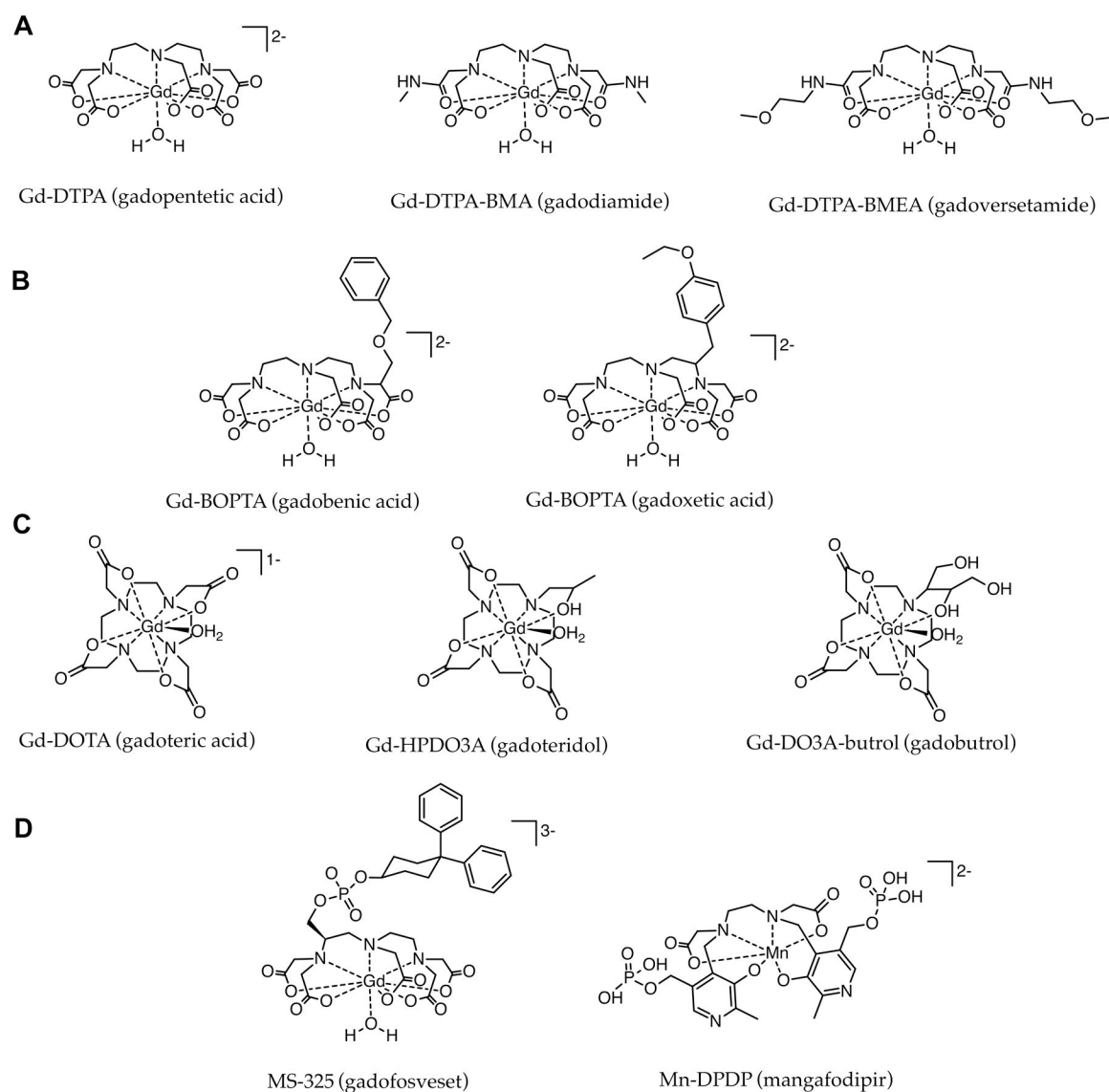
**Figure 1.**
MRI contrast agents that have been approved for use in humans. (A) Acyclic extracellular fluid GBCAs have an FDA contraindication by for use in patients with severe renal insufficiency or acute kidney injury and are no longer marketed in Europe due to toxicity concerns related to retained Gd. Gd-DTPA and Gd-DTPA-BMEA were recently withdrawn from the US market by their manufacturers. (B) Acyclic GBCAs used in liver imaging. Use in the European Union is restricted to liver scans. (C) Macrocyclic GBCAs are considered to be safer with respect to Gd release than acyclic GBCAs. (D) MS-325 and Mn-DPDP are approved for angiography and liver imaging, respectively, but are no longer marketed.
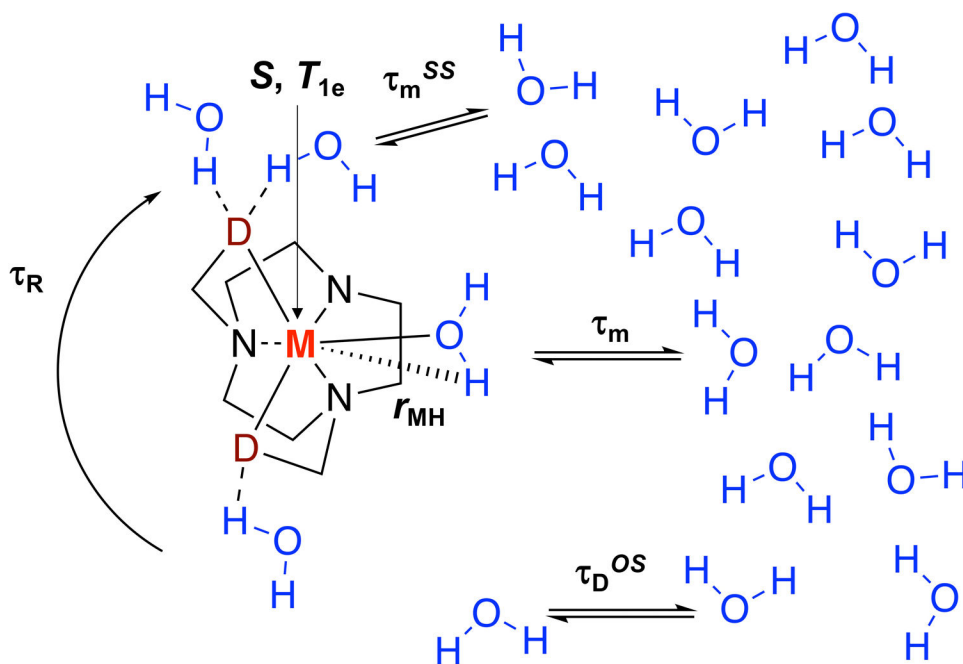
**Figure 2.**
Mechanisms contributing to $r_1$. Like the generic ternary complex depicted above, most transition metal-based relaxation agents are comprised of polydentate ligands build from polyamine backbones. Common pendant donor groups (D) include carboxylates, pyridines, phenolates, phosphonates.
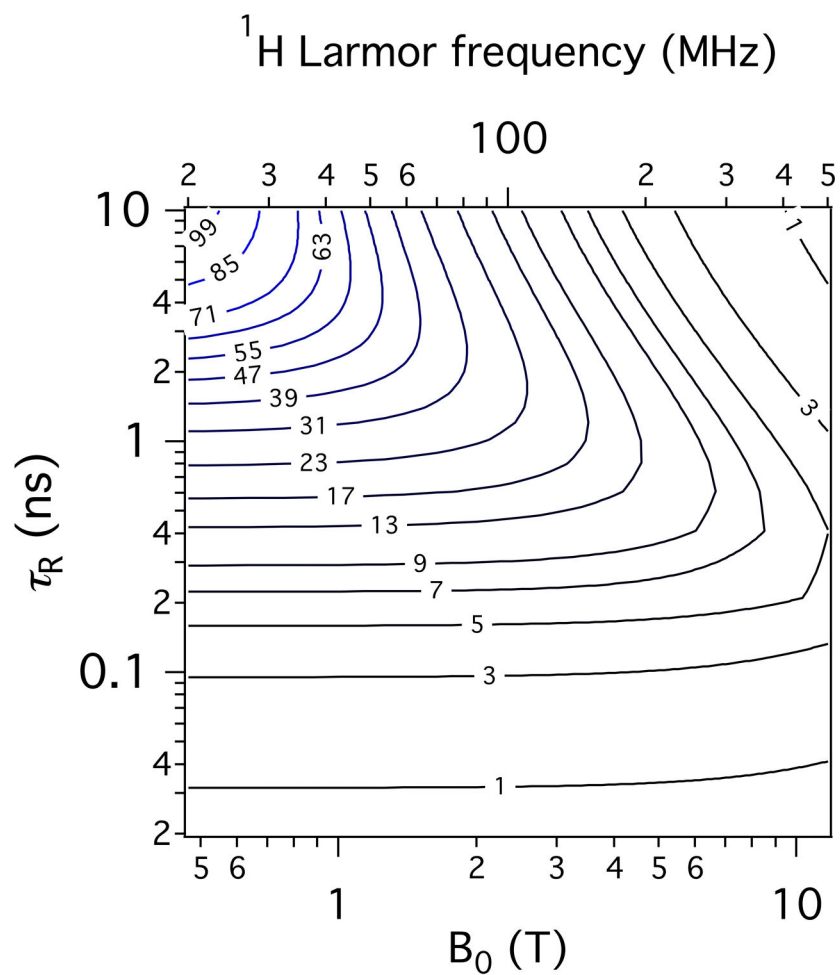
**Figure 3.**
Simulated $r_1^{IS}$ as for a q=1 $Mn^{2+}$ complex of $\tau_m = 10$ ns as a function of $\tau_R$ and $^1$H Larmor frequency according to Equations 2–4.
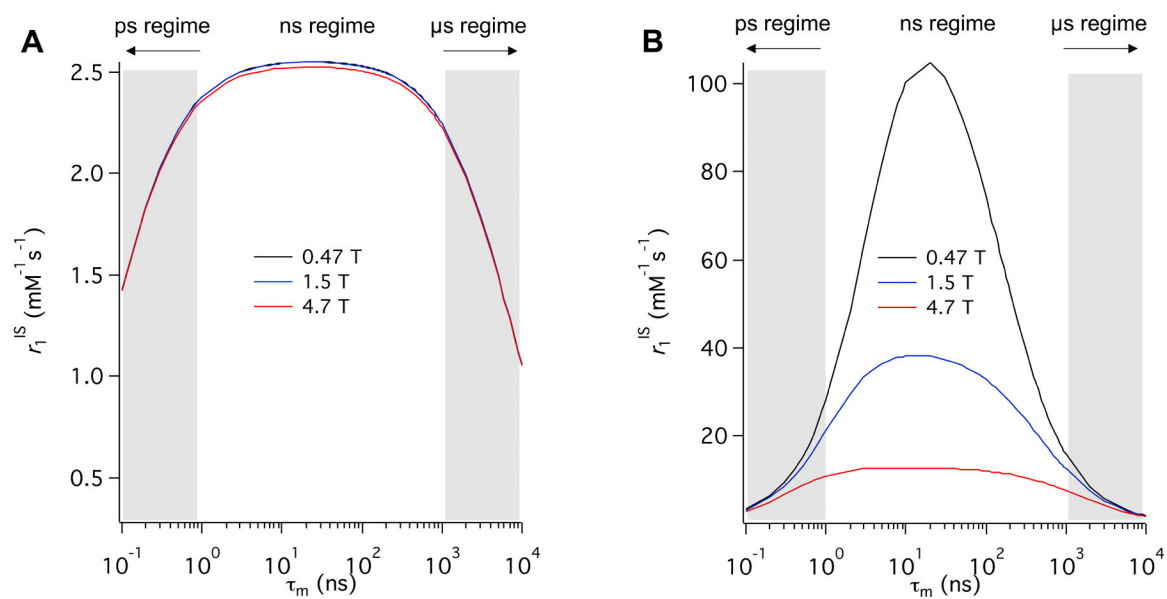
**Figure 4.**
Simulated $r_1^{IS}$ as a function of $\tau_m$ for $q = 1$ $Mn^{2+}$ complex of (A) $\tau_R = 80$ ns and (B) $\tau_R = 1/\omega_H$ at 0.47 T, 1.5T, and 4.7T.
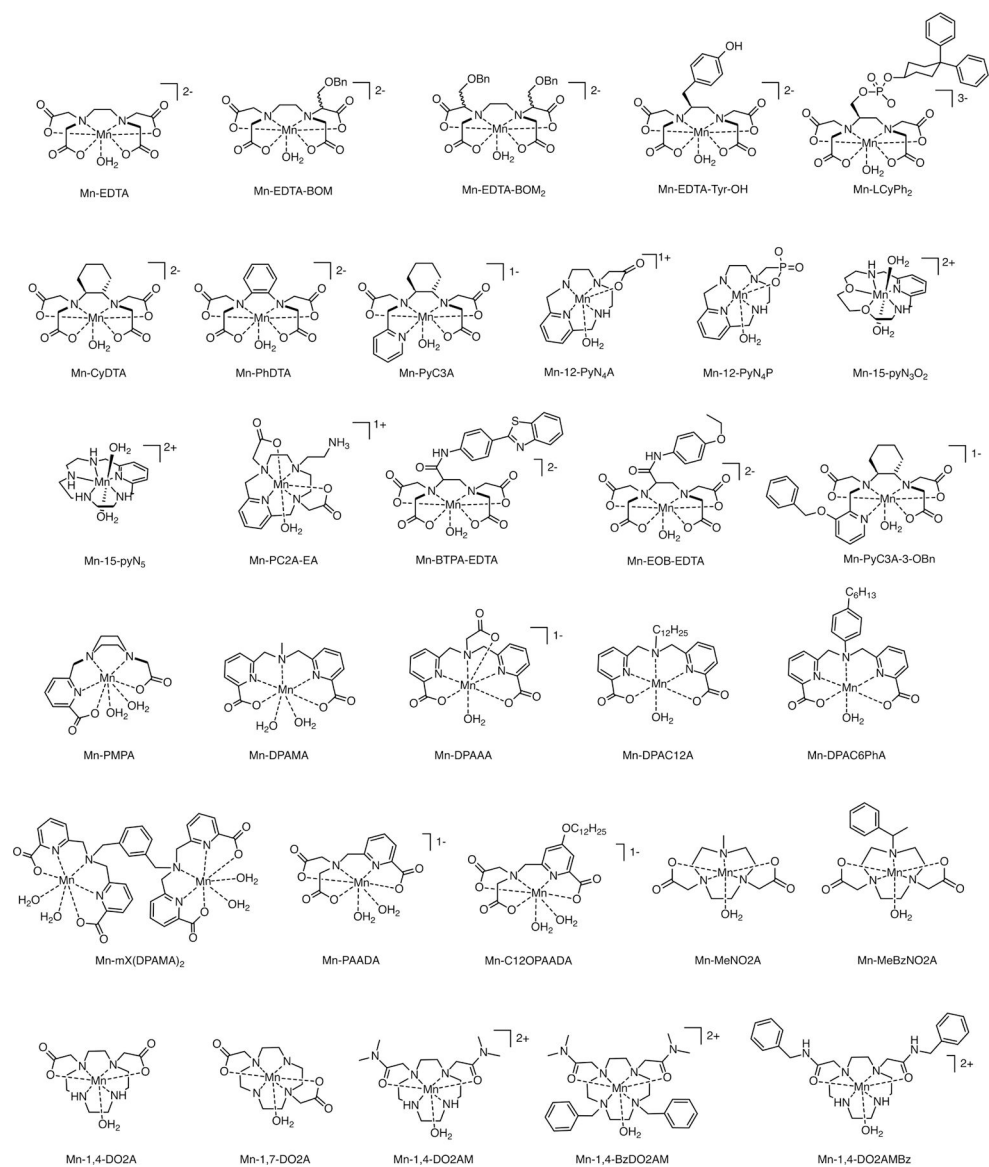
**Figure 5.**
Representative examples of $Mn^{2+}$ complexes considered as $T_1$ relaxation agents
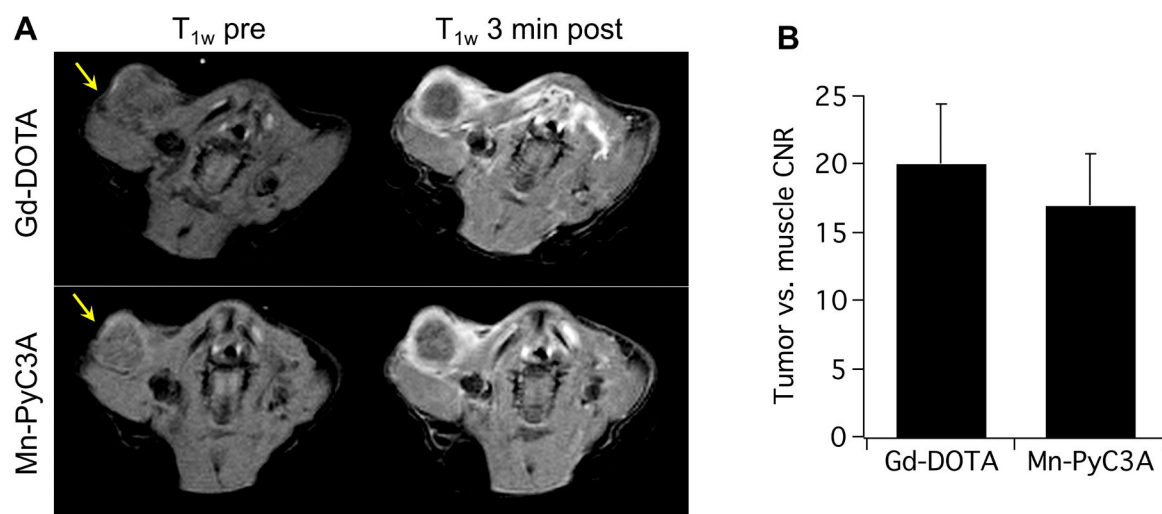
**Figure 6.**
Contrast-enhanced MRI of an orthotopic syngeneic murine model of breast cancer using 0.1 mmol/kg Gd-DOTA and 0.1 mmol/kg Mn-PyC3A. (A) $T_1$-weighted axial MR images through the upper thoracic mammary fat pad and tumor (arrow) before and 3 minutes after injection of Gd-DOTA orMn-PyC3A. Injections of Mn-PyC3A and Gd-DOTA were performed 3 hours apart. For this set of images, Gd-DOTA was injected first. The tumors are denoted by the yellow arrow. (B) Tumor vs. muscle contrast-to-noise ratios obtained using Mn-PyC3A and Gd-DTPA were not significantly different, P = 0.34. Reproduced dapted with permission from reference 114. Copyright (2019, Wolters Kluwer).
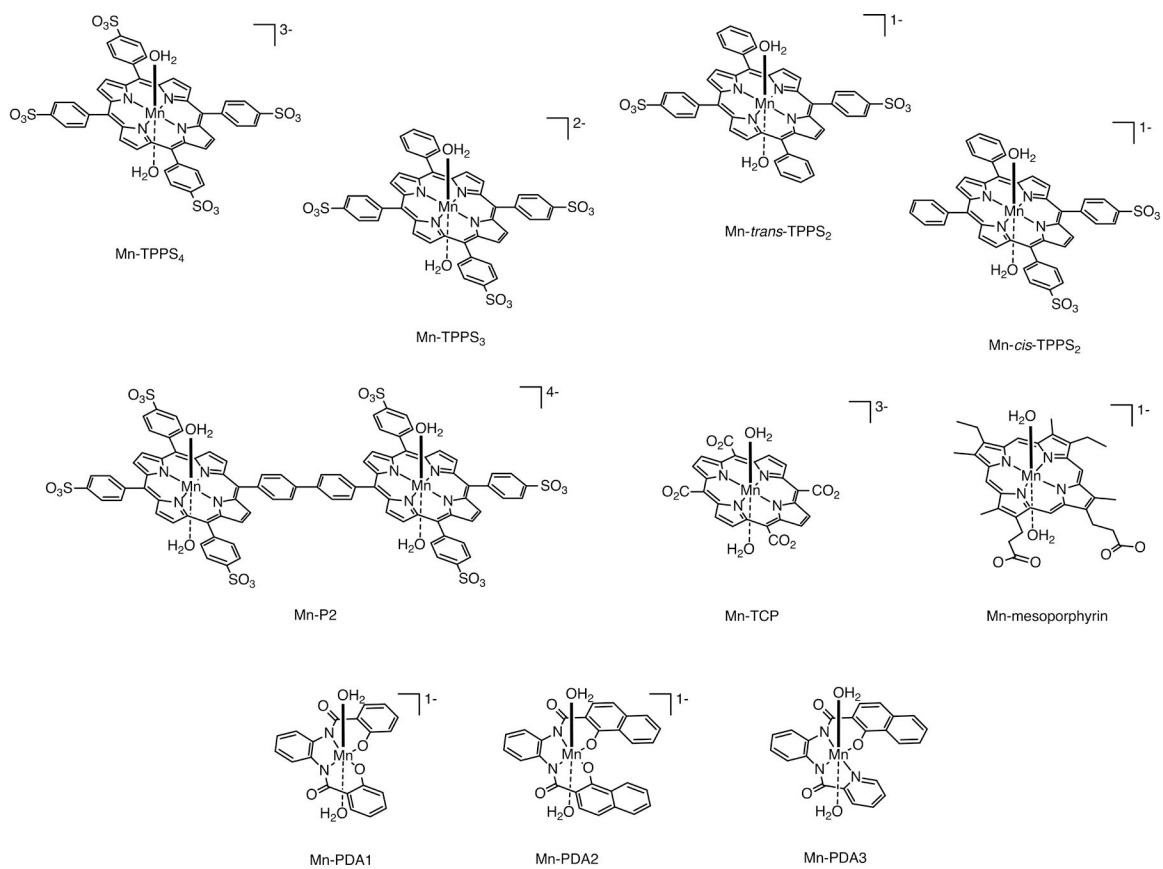
**Figure 7.**
Representative examples of $Mn^{3+}$ complexes considered as $T_1$ relaxation agents.
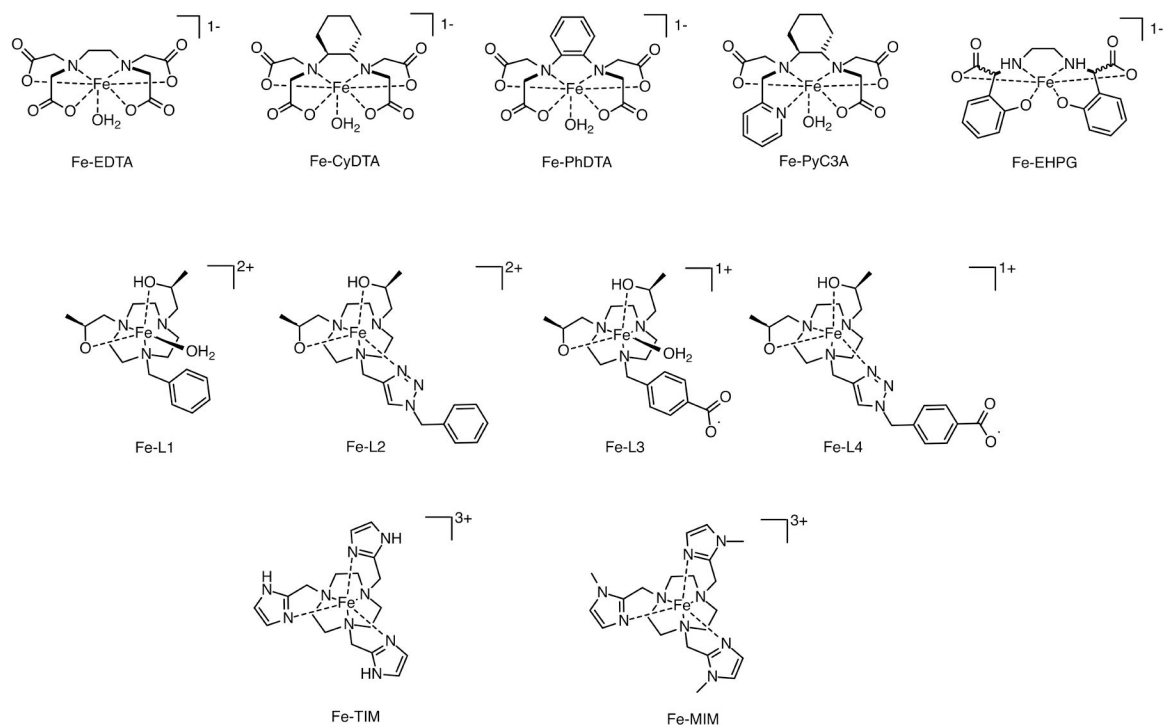
**Figure 8.**
Representative examples of $Fe^{3+}$ complexes considered as $T_1$ relaxation agents.
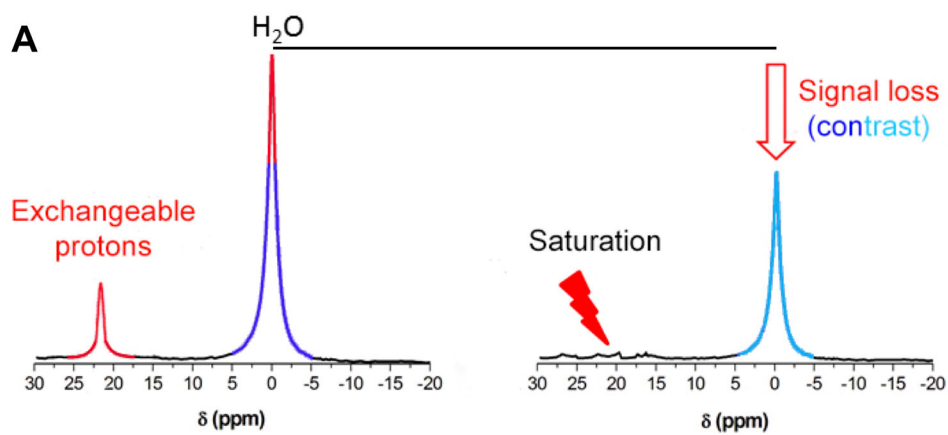
**Figure 9.**
CEST contrast is achieved though radiofrequency saturation of protons capable of exchange with bulk water, resulting in MR signal loss.
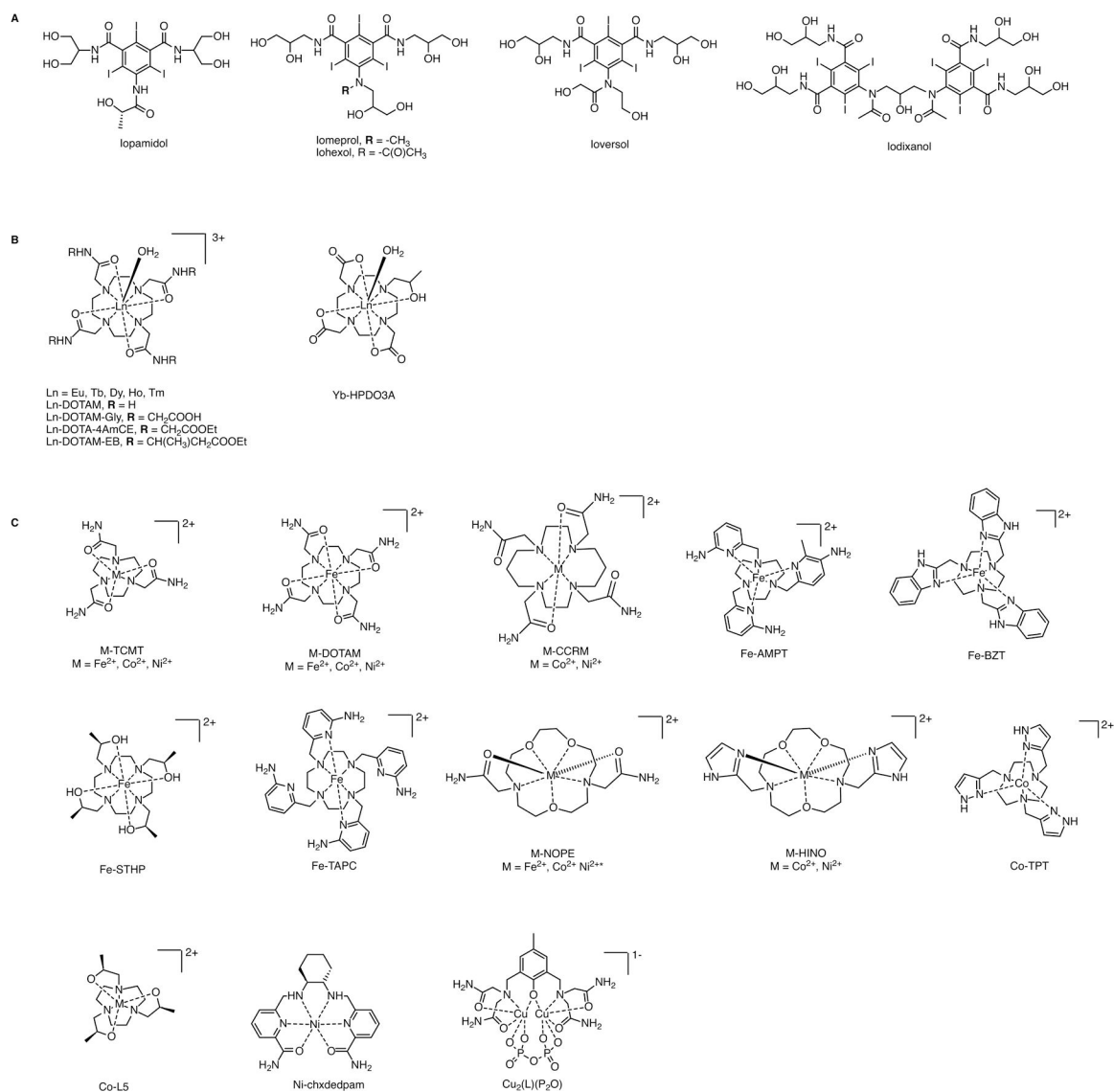
**Figure 10.**
Representative X-ray contrast agents used as diamagnetic CEST agents, (A), lanthanide-based paraCEST agents (B), and transition metal based paraCEST agents (C) discussed in this manuscript.
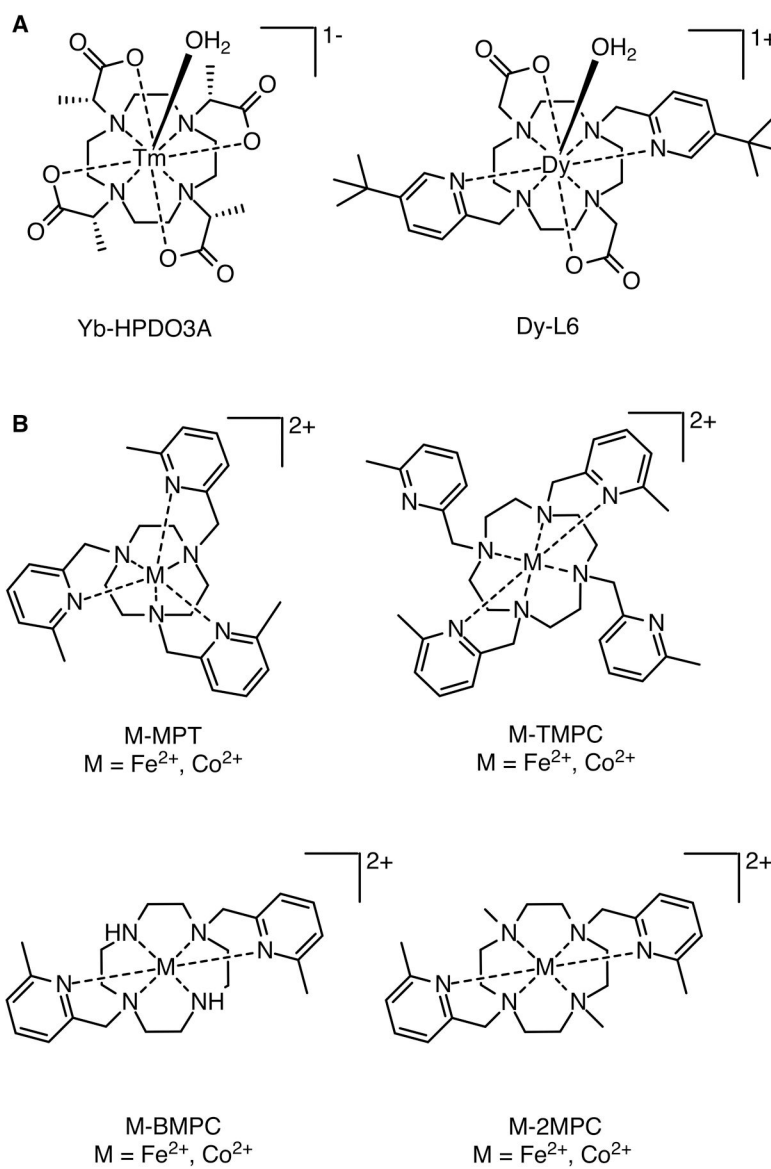
**Figure 11.**
Representative lanthanide-based ^{1}H paraSHIFT agents (A), and transition metal based ^{1}H paraSHIFT agents (B) discussed in this manuscript.
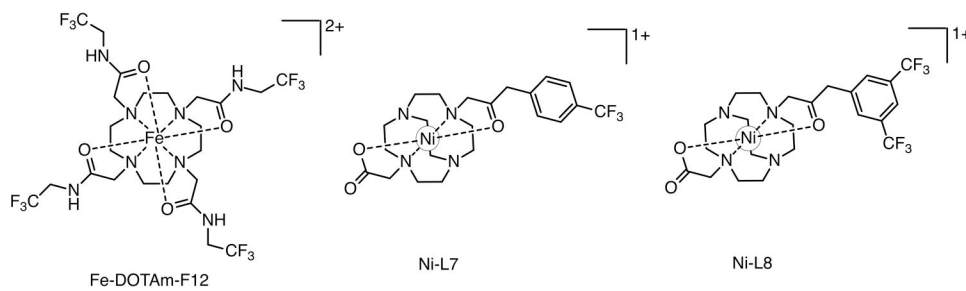
**Figure 12.**
Representative transition metal based $^{19}H$ paraSHIFT agents discussed in this manuscript.
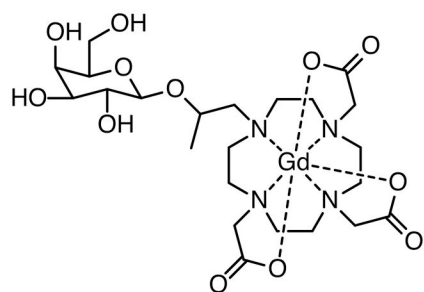
E-GadMe
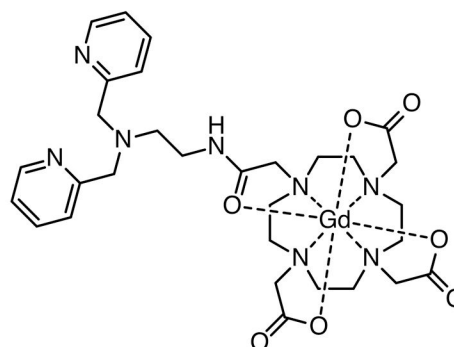
Gd-L1Zn
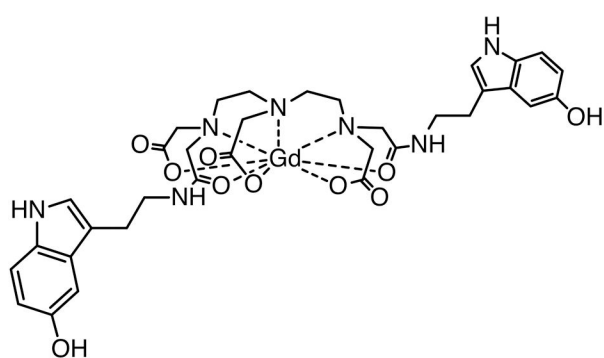
Gd-bis-5HT-DTPA or Gd-MPO
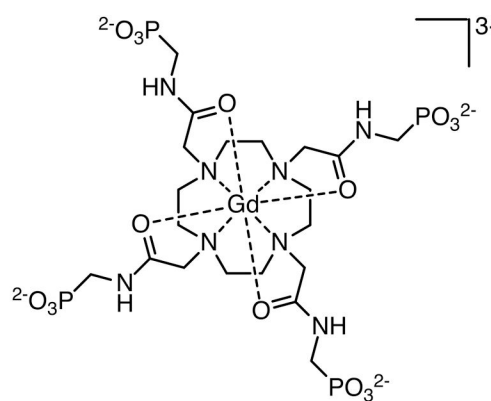
Gd-DOTA-4AmP

**Figure 13.**
Representative examples of biochemically responsive Gd-based relaxation agents.
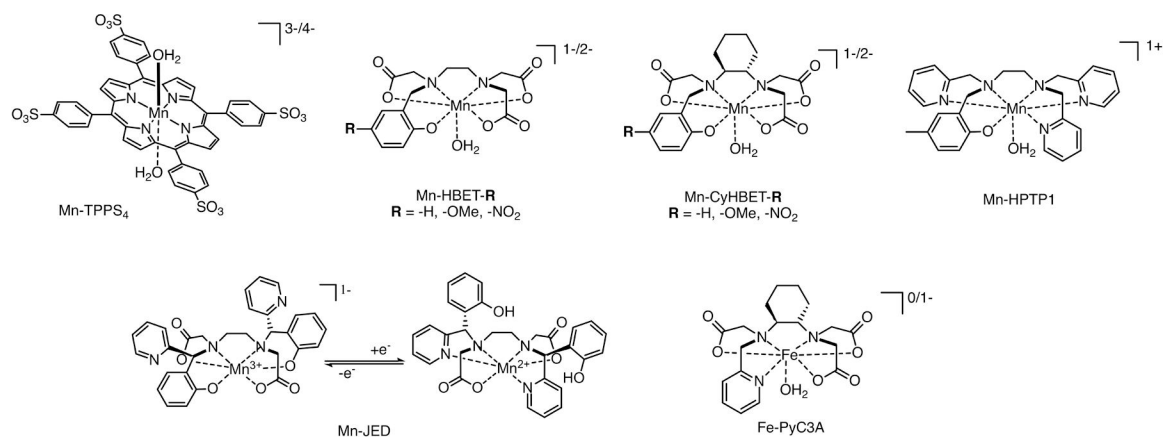
**Figure 14.**
Redox active transition metal complexes ($Mn^{3+/2+}$ and $Fe^{3+/2+}$) complexes studied as biochemically responsive relaxation agents.
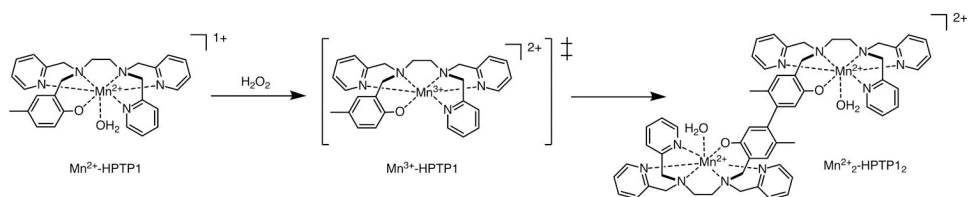
**Figure 15.**
Oxidation of Mn-HPTP1 by $H_2O_2$ results in a unstable $Mn^{3+}$ complex that undergoes ligand-metal auto-redox and dimerization, resulting in 20% $r_1$ change.
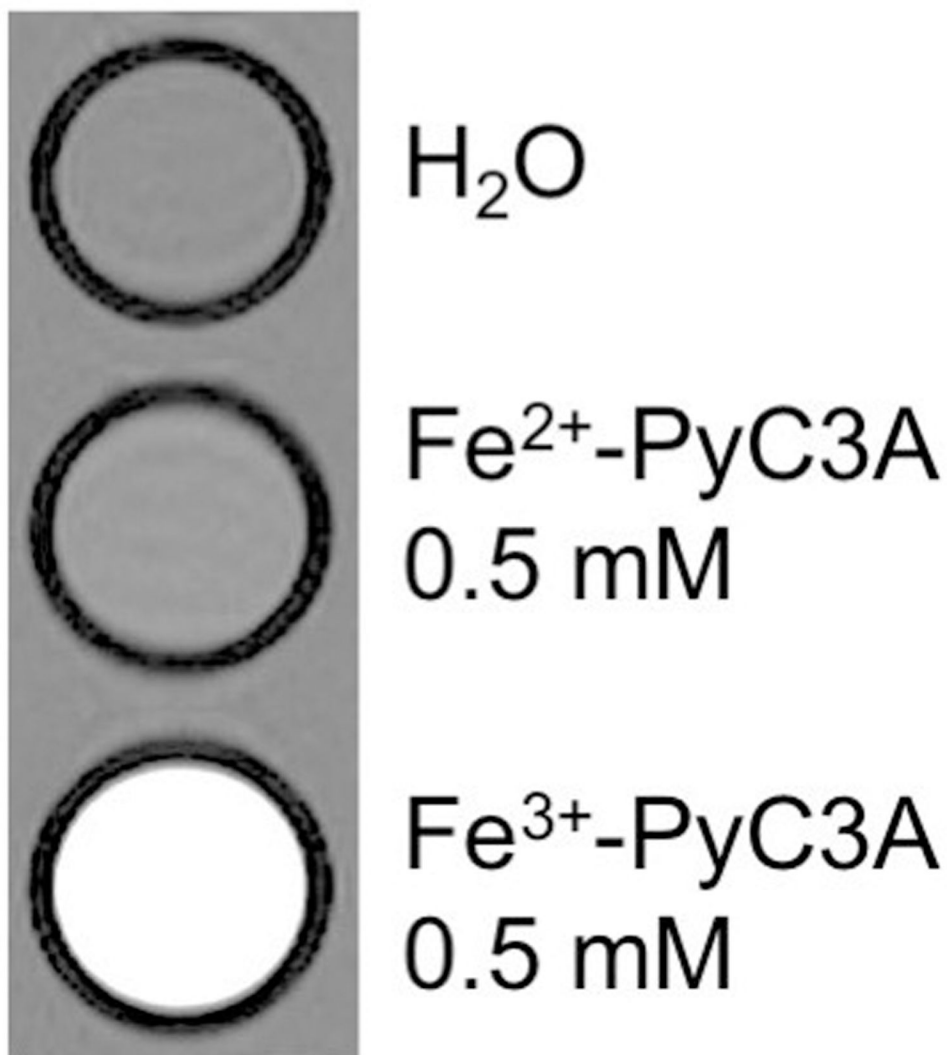
**Figure 16.**
T1-weighted 2D gradient echo images (TR = 125 ms, TE = 2.96 ms, FA = 60°) of phantoms containing neat water, 0.5 mM Fe2+-PyC3A, and 0.5 mM Fe3+-PyC3A at pH 7.4, room temperature and 4.7 T, demonstrate virtual "off/ on" effect. Reproduced/ adapted with permission from reference 101. Copyright (2019, American Chemical Society).
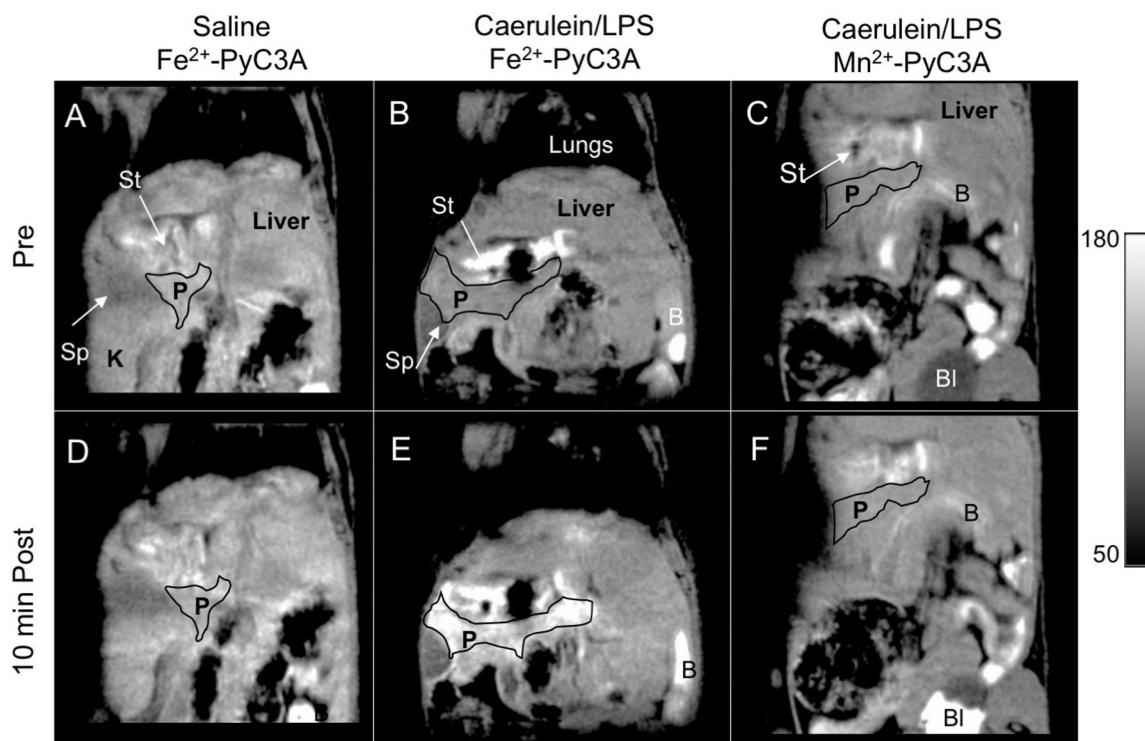
**Figure 17.**

$T_1$-weighted 2D coronal images of saline and caerulein/LPS treated mice recorded prior to and 10 min after injection of $Fe^{2+}$-PyC3A or $Mn^{2+}$-PyC3A. Organs are labelled as follows: P = pancreas, L = Liver, Sp =spleen, St = stomach, K = kidney, M = muscle, B = bowel. Bl = Bladder. Note that pancreas, and liver are isointense prior to contrast injection (A-C), after injection of $Fe^{2+}$-PyC3A to saline treated mice (D), or after injection of $Mn^{2+}$-PyC3A to caerulein/ LPS treated mice (F), but that the pancreas is strongly and selectively enhanced after injection of $Fe^{2+}$-PyC3A to caerulein/ LPS treated mice (E). The bowel and stomach are strongly enhanced at all times because of high levels of metals including Mn present in the mouse chow. Reproduced/ adapted with permission from reference 101. Copyright (2019, American Chemical Society).

Co-TPT    Fe₂(L)(etidronate)    Fe-3-BPP    Fe-Me₂NPY₅Me₂
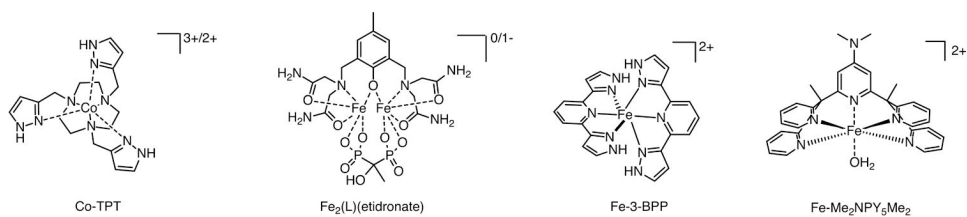
**Figure 18.**
Redox active and spin crossover transition metal complexes studied as biochemically or temperature responsive paraCEST agents.
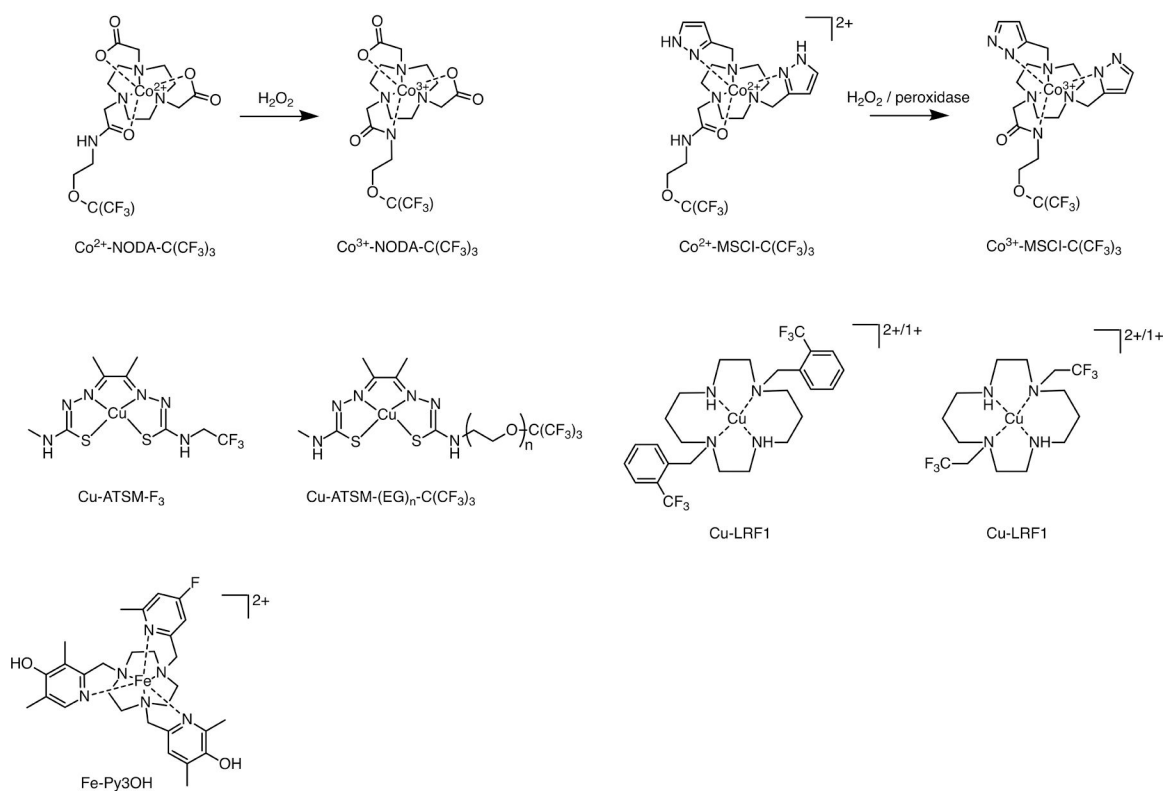
**Figure 19.**
Redox active transition metal complexes complexes studied as biochemically responsive $^{19}$F paraSHIFT agents, Fe-Py3OH undergoes low-spin to high-spin in response to hydroxypyridine deprotonation.

**Table 1.**

Binding affinity for human serum albumin (HSA) and $r_1$ in water, blood plasma, or 660 μM HSA solution for selected $Mn^{2+}$ complexes at different field strengths. Protein binding provides a large $r_1$ increase for $Mn^{2+}$ complexes at 0.47T and 1.5T, but the effect is much more modest at higher field strengths.

| | HSA binding affinity | | $r_1$ in water/ $r_1$ in blood plasma[b] or 660 μM HSA[c] $(mM^{-1}s^{-1})$, 37 °C, | | | |
| | $K_d$ (mM) | % binding[a] | 0.47T (20 MHz) | 1.4T (60 MHz) | 3.0T (128 MHz) | 4.7T (200 MHz) |
|---|---|---|---|---|---|---|
| Mn-EDTA-BOM | 0.67[231] | 48% | $3.6^{d,231}$ / $28^{c,d,e,231}$ | N/D | N/D | N/D |
| Mn-EDTA-BOM$_2$ | 0.053[231] | 92% | $4.3^{d,231}$ / $41^{c,d,e,231}$ | N/D | N/D | N/D |
| Mn-LCyPh$_2$ | 0.011[232] | 98% | $5.8^{232}$ / $46^{b,232}$ | $5.3$ / $27^{c,60}$ | N/D | $4.5$ / $5.6^{c,60}$ |
| Mn-PyC3A-3-OBn | 0.49 | 55% | N/D | 2.6 / 9.9 | N/D | N/D |
| Mn-C12OPAADA | 0.018[233] | 97% | $5.3^{d,233}$ / $30^{c,d,e,233}$ | N/D | N/D | N/D |
| Mn-DPAC12A | 0.0077[233] | 99% | $8.5^{d,233}$ / $15.5^{c,d,e,233}$ | N/D | N/D | N/D |
| Mn-DPAC6PhA | 0.14[234] | 80% | $4.1^{d,234}$ / $37^{c,d,e,234}$ | N/D | N/D | N/D |
| Mn-mX(DPAMA)$_2$ | 0.89[235] | 41% | $6.1^{b,235}$ / $20^{b,e,235}$ | N/D | N/D | N/D |
| Mn-1,4-DO2AM | 0.82[77] | 43% | $2.5^{d,77}$ / $3.8^{c,d,e,77}$ | N/D | N/D | N/D |
| Mn-1,4-DO2AMBz | 0.51[77] | 54% | $3.5^{d,77}$ / $16^{c,d,e,77}$ | N/D | N/D | N/D |
| Mn-1,4-BzDO2AM | 0.26[77] | 70% | $3.8^{d,77}$ / $14^{c,d,e,77}$ | N/D | N/D | N/D |

[a] Percentage protein binding under conditions of 0.1 mM contrast agent, 0.66 mM HSA

[b] recorded in bovine blood plasma

[c] recorded under conditions of 0.1 mM contrast agent, 0.66 mM HSA

[d] recorded at 25 °C

[e] $r_1$ estimated from weighted average of $r_1$ for independently reported free and bound complex under protein binding conditions.

**Table 2.**

Comparison of physicochemical properties of representative transition metal-based $T_1$-relaxation agents discussed as GBCA alternatives.

| | MW | q | $r_1$ in water or buffer, 37 °C (mM$^{-1}$s$^{-1}$) | $r_1$ in blood plasma, 37 °C (mM$^{-1}$s$^{-1}$) |
|---|---|---|---|---|
| **GBCAs** | | | | |
| Gd-DTPA | 546 | 1 | 3.3[a,87] 3.1[b,87] | 4.1[a,j,87] 3.7[b,j,87] |
| Gd-DTPA-BMA | 574 | 1 | 3.3[a,87] 3.2[b,87] | 4.3[a,j,87] 4.0[b,j,87] |
| GD-DTPA-BMEA | 662 | 1 | 3.8[a,87] 3.6[b,87] | 4.7[a,j,87] 4.5[b,j,87] |
| Gd-BOPTA | 666 | 1 | 4.0[a,87] 4.0[b,87] | 6.3[a,j,87] 5.5[b,j,87] |
| Gd-EOB-DTPA | 680 | 1 | 4.7[a,87] 4.3[b,87] | 6.9[a,j,87] 6.2[b,j,87] |
| MS-325 | 904 | 1 | 5.2[a,87] 5.3[b,87] | 19[a,j,87] 9.9[b,j,87] |
| Gd-DOTA | 558 | 1 | 2.9[a,87] 2.8[b,87] | 3.6[a,j,87] 3.5[b,j,87] |
| Gd-HP-DO3A | 559 | 1 | 2.9[a,87] 2.8[b,87] | 4.1[a,j,87] 3.7[b,j,87] |
| Gd-DO3A-butrol | 605 | 1 | 3.3[a,87] 3.2[b,87] | 5.2[a,j,87] 5.0[b,j,87] |
| **Mn$^{2+}$ complexes** | | | | |
| Mn-EDTA | 343 | 1 | 2.2[c,231] | |
| Mn-EDTA-BOM | 481 | 1 | 3.6[d,231] | 28[d,k,l,231] |
| Mn-EDTA-BOM$_2$ | 601 | 1 | 4.3[d,231] | 41[d,k,l,231] |
| Mn-EDTA-Tyr-OH | 449 | 1 | 3.2[c,236] | |
| Mn-BTA-EDTA | 596 | 1 | 3.5[e,91] | 15.1[e,m,91] |
| Mn-EOB-EDTA | 506 | 1 | 2.3[e,90] | 6.3[e,m,90] |
| Mn-LCyPh$_2$ | 686 | 1[57] | 5.8[f,232] | 46[f,n,232] |
| Mn-CyDTA | 397 | 1 | 2.1[c,79] | |
| Mn-PyC3A | 433 | 1 | 2.1[c,79] | 3.5[c,k,86] 3.4[b,k,88], 3.8[c,j,79] |
| Mn-PyC3A-3-OBn | 537 | 1 | 2.6[c,86] | 9.0[c,k,86] |
| Mn-DPAAA | 397 | 1 | 2.7[f,234] | |
| Mn-PAADA | 320 | 2 | 3.3[f,234] | |
| Mn-DPAMA | 354 | 2 | 4.2[f,237] | 9.6[d,k,l,237] |
| Mn-12-PyN$_4$A | 317 | 1 | 1.9[f,83] | |
| Mn-12-PyN$_4$P | 352 | 1 | 22.3[f,83] | |
| Mn-15-PyN$_5$ | 306 | 2 | 3.6[f,84] | |
| Mn-15-PyN$_3$O$_2$ | 304 | 2 | 3.1[f,84] | |

| | MW | $q$ | $r_1$ in water or buffer, 37 °C (mM$^{-1}$s$^{-1}$) | $r_1$ in blood plasma, 37 °C (mM$^{-1}$s$^{-1}$) |
|---|---|---|---|---|
| Mn-PC2A-EA | 361 | 0<q<1 | 2.5[d,78] | |
| Mn-1,4-DO2A | 341 | 1 | 1.7[f,238] | |
| Mn-1,7-DO2A | 341 | 0<q<1 | 1.3[f,238] | |
| Mn-1,4-DO2AM | 241 | 1 | 2.0[f,77] | 9.6[d,k,l,77] |
| Mn-MeNO2A | 328 | 1 | 2.2[f,239] | |
| **Mn$^{3+}$ complexes** | | | | |
| MnTPPS$_4$ | 984 | 2 | 12[e,211] | |
| Mn-TCP | 839 | 2 | 7.9[b,98] | |
| Mn-PDA-1 | 399 | 2 | 4.1[g,104] | |
| Mn-PDA-2 | 499 | 2 | 5.4[g,104] | |
| Mn-PDA-3 | 435 | 2 | 5.1[g,104] | |
| Mn-P2 | 1808 | 2 | 28.2[b,98],14.1/Mn | 32.4[b,o,99], 16.2/Mn |
| **Fe$^{3+}$ complexes** | | | | |
| Fe-CyDTA | 398 | 1 | 2.0[h,117] | 2.2[h,p,117] |
| Fe-L1 | 390 | ND | 2.2[i,111] | 2.5[i,m,111] 3.8[i,q,111] |
| Fe-L2 | 471 | ND | 0.81[i,111] | 1.1[i,m,111] |
| Fe-L3 | 433 | ND | 1.7[i,111] | 2.2,[l,m,111] 1.8[l,q,111] |
| Fe-L4 | 514 | ND | 0.42[i,111] | 0.96[l,m,111] |

[a]1.5T

[b]3.0T

[c]1.4T

[d]0.47T and 25 °C

[e]1.5T and 25 °C

[f]0.47T

[g]7.0T, 22 °C.

[h]0.94T, 37 °C. RT

[i]4.7T

[j]bovine blood plasma

[k]human serum albumin

[l]estimated $r_1$ for 0.1 mmol complex in 0.66 mM HSA based of $r_1$ values reported for free and HSA-bound complex

[m]0.67 mM human serum albumin

[n] human blood plasma

[o] 0.75 mM HSA

[p] fetal calf serum

[q] human blood serum

[r] rabbit blood plasma.

**Table 3.**

Thermodynamic stability constants for GBCAs and $Mn^{2+}$ and $Fe^{3+}$ complexes considered as $T_1$-relaxation agents.

| | $\log K^{a,b}$ | $\log K_{\text{cond pH 7.4}}$ |
|---|---|---|
| Gd-DTPA[1] | 22.5 | 18.4 |
| Gd-DTPA-BMA[1] | 16.9 | 14.8 |
| GD-DTPA-BMEA[1] | 16.6 | 15.0 |
| Gd-BOPTA[1] | 22.6 | 18.4 |
| Gd-EOB-DTPA[1] | 23.5 | 18.7 |
| MS-325[1] | 22.1 | 18.9 |
| Gd-DOTA[1] | 24.7 | 17.2 |
| Gd-HP-DO3A[1] | 23.8 | 17.1 |
| Gd-DO3A-butrol[1] | 21.8 | 14.7 |
| Mn-EDTA | 12.6,[213] 13.9[231] | 10.7,[213] 11.0[231] |
| Mn-EDTA-BOM[231] | 13.5 | 10.6 |
| Mn-EDTA-BOM$_2$[231] | 13.9 | 11.0 |
| Mn-CyDTA[213] | 14.3 | 12.3 |
| Mn-PyC3A[79] | 13.9 | 11.3 |
| Mn-DPAAA[234] | 13.19 | 13.0 |
| Mn-PAADA[233] | 9.59 | 8.8 |
| Mn-DPAMA[237] | 10.13 | 10.1 |
| Mn-PMPA[240] | 14.3 | 11.1 |
| Mn-12-PyN$_4$A[83] | 11.5 | 7.1 |
| Mn-12-PyN$_4$P[83] | 14.1 | 7.4 |
| Mn-15-PyN$_5$[84] | 10.9 | 7.7 |
| Mn-15-PyN$_3$O$_2$[84] | 7.2 | 5.2 |
| Mn-PC2A-EA[78] | 19.0 | 12.7 |
| Mn-1,4-DO2A[241] | 16.1 | 10.1 |
| Mn-1,7-DO2A[241] | 14.5 | 8.2 |
| Mn-1,4-DO2AM[77] | 12.64 | 8.9 |
| Fe-CyDTA | 30.1 | 28.0 |
| Fe-PyC3A[110] | N/D | 23.2 |
| Fe-EHPG[212] | >30 | N/D |

[a] $K$ = [metal-ligand complex]/[metal][ligand].

[b] $\log K$ may vary depending on measurement conditions (typically within $\log K$ +/− 1).

**Table 4.**

Kinetic inertness data for GBCAs and $Mn^{2+}$ complexes recorded under different experimental conditions. <u>Dissociation Challenge 1</u>: 2.5 mM contrast agent is incubated with 2.5 mM $Zn^{2+}$ in 50 mM pH 7.0 phosphate buffer at 37 °C, and kinetic inertness is compared by measuring the time required to achieve 20% release of the paramagnetic ion ($t_{20\%}$). <u>Dissociation Challenge 2</u>: 1 mM contrast agent, 25 mM $Zn^{2+}$, pH 6.0 MES buffer. <u>Dissociation Challenge 3</u>. [contrast agents] = [$Zn^{2+}$ or $Cu^{2+}$] = 0.01 mM, pH 7.4,. <u>Dissociation Challenge 4</u>. [contrast agents] = [$Zn^{2+}$ or $Cu^{2+}$] = 1.0 mM.

| | $t_{20\%}$ $Zn^{2+}$ challenge 1 (h) | $t_{1/2}$ $Zn^{2+}$ challenge 2 (h) | $t_{1/2}$ $Zn^{2+}$ challenge 3 (h) | $t_{1/2}$ $Zn^{2+}$ challenge 4 (h) |
|---|---|---|---|---|
| Gd-DTPA | 4.4,[242] 2.8[79] | 0.013[79] | 330 [a, 85] | 3.5 [a, 85] |
| Gd-DTPA-BMA | 1.0[242] | | | |
| Gd-BOPTA | 10[242] | | | |
| Gd-EOB-DTPA | 25[242] | | | |
| MS-325 | 60[242] | | | |
| Gd-DOTA | >83[242] | | $3.8 \times 10^5$ [a, 76] | $3.8 \times 10^5$ [a, 76] |
| Gd-HP-DO3A | >80[242] | | | |
| Gd-DO3A-butrol | >80[242] | | | |
| Mn-EDTA | | | .076[a, 114] | $4.3 \times 10^{-3}$[a, 114] |
| Mn-CyDTA | | 0.18[79] | 12[a, 114] | 12[a, 114] |
| Mn-PhCDTA | | | 19[a, 243] | 0.86[a, 243] |
| Mn-PyC3A | 1.8[79] | 0.29[79] | | |
| Mn-12-PyN4A | | | 2.6[a, 83] | 2.6[a, 83] |
| Mn-15-PyN5 | | | 11[a, 84] | 11[a, 84] |
| Mn-PC2A-EA | | 54[78] | 8100[a, 78] | 8100[a, 78] |
| Mn-1,4-DO2A | | | 49[a, 77] | 49[a, 77] |
| Mn-1,7-DO2A | | | 58[a, 77] | 58[a, 77] |
| Mn-1,4-DO2AM | | | 560[a, 77] | 560[a, 77] |

[a] Denotes $t_{1/2}$ estimated from empirical rate law data.

**Table 5.**

Comparison of pKa values for water co-ligand of representative $Fe^{3+}$ complexes shown in Fig 8 demonstrates that water co-ligand pKa is very sensitive to changes in ligand structure and electronics.

|  | pKa – water co-ligand |
|---|---|
| Fe-CyDTA[109] | 9.6 |
| Fe-PyC3A[110] | 8.5 |
| Fe-EDTA[109] | 7.6 |
| Fe-PhDTA[108] | <4.0 |

**Table 6.**

Chemical shift in ppm and $k_{ex}$ for CEST active protons of X-ray contrast agents, lanthanide-based and transition metal-based paraCEST agents shown in Figure 10.

| | Functional group | $\delta_H$ (ppm) | $k_{ex}$ (s$^{-1}$) |
|---|---|---|---|
| Iopamidol[123] | amide NH | 4.10 | 2,560[a] |
| Iomeprol[244] | amide NH | 4.30 | 1,830[a] |
| Iohexol[244] | Amide NH | 4.30 | 1,610[a] |
| Ioversol[244] | Amide NH | 4.30 | 1,630[a] |
| Iodixanol[244] | Amide NH | 4.30 | 1,210[a] |
| | | | |
| Tb-DOTA-4AmCE[121] | Water co-ligand | −600 | 32,300 |
| Dy-DOTA-4AmCE[121] | Water co-ligand | −720 | 58,800 |
| Yb-HPDO3A[245] | Alcohol OH | 71[b], 99[b] | N/D |
| Tm-DOTAM-Gly[246] | Amide NH | −51[c] | 3,450 |
| Ho- DOTAM-Gly[246] | Amide NH | 39[c] | 2,500 |
| Dy- DOTAM-Gly[246] | Amide NH | 77[c] | 2,500 |
| Eu-DOTAM-EB[247] | Amide NH | 53 | 12,300 |
| | | | |
| Fe-TCMT[248] | Amide NH | 69 | 240 |
| Fe-AMPT[248] | Aminopyridine NH$_2$ | 6.5 | N/D |
| Fe-BZT[248] | Benzothiazole -NH | 53 | N/D |
| Fe-STHP[248] | Alcohol OH | 54 | 3,000 |
| Fe-DOTAM[248] | Amide NH | 50 | 400 |
| Fe-TAPC[131] | Aminopyridine NH$_2$ | −79 | 1,700[d] |
| Fe-NOPE[133] | Amide NH | 92, 24[e] | 500 |
| Co-TCMT[248] | Amide NH | 32 | 890 |
| Co-DOTAM[248] | Amide NH | 45 | 300 |
| Co-CCRM[248] | Amide NH | 112 | 510 |
| Co-TPT[248] | Pyrazole NH | 135 | 9,200 |
| Co-HINO[127] | Imdazole NH | 32 | 1020[a] |
| Co-TAPC[131] | Aminopyridine NH$_2$ | −118 | N/D |
| Co-NOPE[133] | Amide NH | 59, −19[e] | 240 |
| Co-L5[136] | Alcohol OH | 140 | 5,000[f] |
| Ni-TCMT[248] | Amide NH | 76 | 364 |

| | Functional group | $\delta_H$ (ppm) | $k_{ex}$ (s$^{-1}$) |
|---|---|---|---|
| Ni-CCRM[248] | Amide NH | 72 | 328 |
| Ni-HINO[127] | Imdazole NH | 55 | 1020[a] |
| Ni-NOPE[133] | Amide NH | 72, 11[e] | 240 |
| Ni-DOTAM[249] | Amide NH | 73 | 330 |
| Ni- chxdedpam[250] | Amide NH | 91.5[e,g] | 6,100 |
| $Cu_2(L)(P_2O_7)$[138] | Amide NH | 29 ppm | 420 |

[a]pH 7.4

[b]The two -OH resonances observed have been tentatively assigned to R and S form of Yb-HP-DO3A.

[c]pH 8.1, 312K

[d]pH 7.7

[e]magnetically inequivalent NH from amide NH$_2$.

[f]pH 7.0

[g]pH 7.2

**Table 7.**

Chemical shift in ppm, $T_1$, and full-width at half max (FWHM) of observed $^1$H for representative lanthanide-based and transition metal-based paraSHIFT agents.

| | $^1$H resonance | Equiv. protons | $T_1$ (ms) | $\delta_H$ (ppm) | FWHM (Hz) | FWHM (ppm) |
|---|---|---|---|---|---|---|
| Dy-L2[171] | –tBu | 18 | 5.7[c] | –17.8[a] –29.9[a] | 78[b,c,f] | 0.20 [b,c,f] |
| Tm-DOTMA[171–172] | –CH$_3$ | 24 | 4.1[a], 5.3[a] | –107[a], –66.5[a] | 103[a,c,f], 84[a,c,f] | 0.26[a,c,f], 0.21[a,c,f] |
| DyL2[251] | –tBu | 18 | 8.0[d] | –60.1. –63.8 | N/D | |
| Fe-MPT[158] | –CH$_3$ | 9 | 2.4[e] | 21.2 | 207[e] | 0.41[e] |
| Fe-TMPC[158] | –CH$_3$ | 6 | 1.1[e] | –52.3 | 458[e] | 0.92[e] |
| Fe-BMPC[157] | –CH$_3$ | 6 | 0.62[e] | –22.5 | 480[e] | 0.96[e] |
| Fe-2MPC[157] | –CH$_3$ (pyridine) | 6 | 1.0[e] | –45.5 | 393[e] | 0.79[e] |
| | –CH$_3$ (amine) | 6 | 1.1[e] | 105 | 359[e] | 0.72[e] |
| Co-MPT [158] | –CH$_3$ | 9 | 5.7[e] | 8.03 | 66.5[e] | 0.13[e] |
| Co-TMPC[158] | –CH$_3$ | 6 | 0.37[e] | –120 | 909[e] | 1.8[e] |
| Co-BMPC[157] | –CH$_3$ | 6 | 0.30[e] | –80.4 | 1150[e] | 2.3[e] |
| Co-2MPC[157] | –CH$_3$ (pyridine) | 6 | 0.44[e] | –112.5 | 848[e] | 1.7[e] |
| | –CH$_3$ (amine) | 6 | 0.18[e] | 164.4 | 1982[e] | 4.0[e] |

[a] two isomers

[b] corresponds to major isomer with $\delta$ = 17.8ppm

[c] 9.4T

[d] 7.0T

[e] 11.7T

[f] calculated from $T_2$, assuming T$_2$ ~ 1/($\nu_{1/2}$*$\pi$).

**Table 8.**

$T_1$ and full-width at half max (FWHM) of observed $^{19}F$ resonance for representative ligands and corresponding transition metal-based complexes.

| | $^{19}F$ resonance | Equiv. protons | $T_1$ (ms) | FWHM (Hz) | FWHM (ppm) |
|---|---|---|---|---|---|
| DOTAm-F12[156] | $-CF_3$ | 12 | 880a | $0.59^{a,b}$ | $0.0017^{a,b}$ |
| Fe- DOTAm-F12[156] | $-CF_3$ | 12 | 5.7a | $103^{a,b}$ | $0.20^{a,b}$ |
| Ni-L7[160] | $-CF_3$ | 3 | 0.03a | $13^{a,b}$ | $0.047^{a,b}$ |
| Ni-L8[160] | $-CF_3$ | 6 | 0.01a | $40^{a,b}$ | $0.14^{a,b}$ |

[a]7.0T

[b]calculated from $T_2$, assuming $T_2 \sim 1/(\nu_{1/2}*\pi)$.

**Table 9.**

Comparison of biochemically mediated $r_1$ change achieved with representative Gd and transition metal complexes studied as biochemically responsive contrast agents.

| | $r_1$ change triggered by: | mechanism of $r_1$ change | "off" $r_1$/ "on" $r_1$ ($mM^{-1}s^{-1}$), magnitude $r_1$ change. | | |
|---|---|---|---|---|---|
| | | | **0.47T** | **1.4T** | **>3.0T** |
| EgadMe[197] | β-galactosidase | $q$ increase | N/D[a] | N/D[a] | 0.9/ 2.7[b], 3-fold |
| Gd-MPO | $H_2O_2$/myeloperoxidase | $\tau_R$ increase by oligomerization | 4.3/10.5, 2.4-fold[207] | N/D | 4.9/4.8[c], no change[110] |
| Gd-LZn[252] | $Zn^{2+}$ binding and subsequent HSA association | $\tau_R$ increase from $Zn^{2+}$ triggered albumin binding | 5.8/18, 3.1-fold | N/D | 6.0/6.8d, ~10% |
| Gd-4AmP[203–204] | pH change | Prototropic exchange, second sphere | N/D | N/D | 6.0 (pH 6)/ 4.0 (pH 4), ~50%, or ~5% per 0.1 pH unit[d] |
| Mn-TPPS$_4$[92] | $O_2$ | Oxidation from $Mn^{2+}$ to $Mn^{3+}$ | 10/12, ~20% | N/D | N/D |
| Mn-TPPS$_4$[92] | $O_2$, in presence of β-cyclodextrin | Oxidation from $Mn^{2+}$ to $Mn^{3+}$ | 23/58, ~2.5 fold | N/D | N/D |
| Mn-HBET[213] | Redox ($H_2O_2$, $L$-Cys) | $Mn^{2+}/Mn^{3+}$ interchange | N/D | 1.1/2.8, 2.5-fold | 1.1/3.9[d], 3.5-fold |
| Mn-HBET-NO$_2$[213] | Redox | $Mn^{2+}/Mn^{3+}$ interchange | N/D | 0.50/2.3, 5.8-fold | 0.7/3.1[d], 4.4-fold |
| Mn-CyHBET[213] | Redox | $Mn^{2+}/Mn^{3+}$ interchange | N/D | 0.40/3.3, 8.3-fold | |
| Mn-CyHBET-NO$_2$[213] | Redox | $Mn^{2+}/Mn^{3+}$ interchange | N/D | 0.50/2.3, 5.6-fold | |
| Mn-JED[217] | Redox ($H_2O_2$/ peroxidase, $L$-Cys) | $Mn^{2+}/Mn^{3+}$ interchange | N/D | 0.5/3.3, 6.6-fold 0.9/8.0, 8.9-fold | 0.9/4.3[d], 4.8-fold 1.1/ 3.6[b], 4.6-fold 0.5/2.5[d], 5.0-fold 0.5/ 1.9[b], 3.8-fold |
| Mn-HPTP1 | $H_2O_2$ | Dimerization, $\tau_R$ increase | N/D | N/D | 4.4–3.6e, ~ −20% |
| Fe-PyC3A[110] | $H_2O_2$, L-cys | $Fe^{2+}/Fe^{3+}$ interchange | N/D | 0.18/1.8, 10-fold | 0.18/2.4[d], 13-fold 0.15/2.2[b], 15-fold |

[a]$r_1$ change from $q$ modulation is field independent.

[b]11.7T

[c]4.7T

[d]9.4T

[e]3.0T